STUDY OF DIRECT PHOTON PRODUCTION WITH HEAVY FLAVOR JETS IN $p\overline{p}$ COLLISIONS AT$\sqrt{S} = 1.96\ \ \mathrm{TEV}$ WITH DZERO DETECTOR

A THESIS

Submitted to the

FACULTY OF SCIENCE
PANJAB UNIVERSITY, CHANDIGARH

for the degree of

DOCTOR OF PHILOSOPHY

2016

MANBIR KAUR

DEPARTMENT OF PHYSICS
CENTRE OF ADVANCED STUDY IN PHYSICS
PANJAB UNIVERSITY
CHANDIGARH, INDIA

This thesis is dedicated to

my family,

for

their love,

endless support

and encouragement.

Acknowledgements

I would like to thank my supervisor Prof. Suman B. Beri for her guidance, ideas, patience, support and motivation for the work done in this thesis. I consider myself very fortunate for being able to work with a very considerate and encouraging professor like her. It was a great learning experience to work under her supervision. I am thankful to the Chairman of Department of Physics at Panjab University for providing adequate facilities to work in the department. Many thanks and regards go in particular to Prof. J. B. Singh, Prof. M. Kaur and Prof. V. Bhatnagar for their continuous support and help in PUHEP lab. I would also like to thank the technical, computing and purchase section staff of Department of Physics and HEP office at Panjab University.

Special thanks go to the previous and current conveners of QCD working group at DØ: Leo Bellantoni, Dmitry Bandurin, Ashish Kumar and Peter Svoisky. Working with all of you is the most educational and enjoyable experience of my life. Also, I owe my thanks to DØ spokesperson Dr. Dmirti Denisov and all the members of DØ collaboration including physicists, engineers and technicians who worked hard, day and night, to make it successful.

I am deeply thankful to my colleagues at Panjab University; Nishu, Archana, Suneel, Sunil, Monika, Anil, Lovedeep, Bhawan, Kanishka, Charanjit, Ila, Genius, Raman Kumar, Amandeep, Anterpreet, Ridhi, Manisha, Ankita, Anwinder, Priyanka, Rajat, Sandeep, Sandeep Sharma and Renu who were always present for helping me out from all kind of problems with their suggestions, discussions and creating enjoyable environment in the lab. I would also like to thank all of my Indian friends whom I have met at Fermilab during my two and a half year of stay, Jyoti, Sonam, Richa, Ruchika, Sadia, Pratima, Suvadeep, Shilpee, Amit, Navaneeth, Nitin and Siva. Special thanks to Phillip, Daisy, Jyoti, Diego, Siddharatha, Deepthi, Sarah, Stefano, Mateus, Mark, Xuan, the staffs of the PAB and the Fermilab housing office, for making my five years of Ph.D life so colorful and enjoyable. Many thanks to my *friend Tom and his late bird "Taco".*

Thank you Mom and Dad, for all the unconditional love and encouragement. This thesis would have been simply impossible without your support. I thank my siblings Sofia and Taran for their constant support in all phases of my life. Special thanks to Cheryl for always believing in me and providing moral support throughout. Special thanks go to the love of my life Gary. Without you it would have been a lot less fun and a lot harder to get through this PhD. Many thanks to the Forster Family for enormous love and support. I love you all.

In retrospect, there are so many great people to give thanks to. Without them I would not have been able to come this far or complete this thesis. Though I cannot print out all the names, it is worthy noting that many great people helped me in different ways along this journey. I thank them all here.

Date: **(Manbir Kaur)**

Abstract

In hadronic collisions, photons (γ) with high energies emerge unaltered from the hard parton-parton interaction and therefore provide a clean probe of the underlying hard-scattering dynamics. Photons produced in these interactions (called direct or prompt) in association with one or more bottom (b)-quark jets provide an important test of perturbative Quantum Chromodynamics (QCD) predictions at large hard-scattering scales Q and over a wide range of parton momentum fractions. In addition, the study of these processes also provides information about the parton density functions of b quarks and gluons (g), which still have substantial uncertainties. In $p\bar{p}$ collisions, $\gamma + b$-jet events are produced primarily through the Compton process $gb \to \gamma b$, which dominates for low and moderate photon transverse momenta (p_T^γ), and through quark-antiquark annihilation followed by $g \to b\bar{b}$ gluon splitting $q\bar{q} \to \gamma g \to \gamma b\bar{b}$, which dominates at high p_T^γ. The final state with b-quark pair production, $p\bar{p} \to \gamma + b\bar{b}$, is mainly produced via $q\bar{q} \to \gamma b\bar{b}$ and $gg \to \gamma b\bar{b}$ scatterings. The $\gamma + 2$ b-jet process is a crucial component of background in measurements of, for example, $t\bar{t}\gamma$ coupling and in some searches for new phenomena.

This thesis presents the first measurements of the differential cross section $\mathrm{d}\sigma/\mathrm{d}p_T^\gamma$ for the production of an isolated photon in association with at least two b-quark jets. The ratio of differential production cross sections for $\gamma + 2$ b-jets to $\gamma + b$-jet as a function of p_T^γ is also presented. The measurement of the ratio of cross sections leads to cancellation of various experimental and theoretical uncertainties, allowing a more precise comparison with the theoretical predictions. The results are based on the proton-antiproton collision data corresponding to an integrated luminosity of 8.7 fb^{-1} at $\sqrt{s}$ =1.96 TeV collected with the DØ detector at the Fermilab Tevatron Collider. The large data sample and use of advanced photon and b-jet identification tools enable us to measure the $\gamma + 2$ b-jet production cross section differentially as a function of p_T^γ. This allows for probing the dynamics of the production process over a wide kinematic range not studied before in other measurements of a vector boson + b-jet final state. The measured cross sections and their ratios are compared to the NLO perturbative QCD calculations as well as predictions based on the k_{T}-factorization approach and those from the SHERPA and PYTHIA Monte Carlo event generators.

We also measure the ratio of cross sections, $\sigma(p\bar{p} \to Z + 2\ b \text{ jets})/\sigma(p\bar{p} \to Z + 2 \text{ jets})$, for associated production of a Z boson with at least two jets. This measurement uses data corresponding to an integrated luminosity of 9.7 fb^{-1} collected by the DØ experiment. The measured integrated ratio is in agreement with predictions from NLO perturbative QCD and the Monte Carlo event generators ALPGEN and PYTHIA. A good theoretical description of this process is essential since it forms a major background for a variety of physics processes, including standard model Higgs boson production in association with a Z boson, $ZH(H \to b\bar{b})$, and searches for supersymmetric partners of the b quark.

These results will improve our theoretical understanding as we search for phenomena beyond the standard model using the data from similar collider experiments in the case where the final states of the interaction involved the production of vector bosons in association with two b-quark jets.

This work has been done in collaboration with DØ experiment but the analyses and results presented in this thesis are my contribution.

Contents

List of Figures

List of Tables

Chapter 1

Introduction

“By convention sweet is sweet, bitter is bitter, hot is hot, cold is cold, color is color; but in truth there are only atoms and the void” -*Democritus*

1.1 Elementary particles

All matter which makes our universe is presently believed to consist of a few fundamental constituents called elementary particles. The idea of indivisible fundamental particle is very old. It goes back to the times of a Greek philosopher Democritus who gave the concept of atoms, but it was not until the 1900s that scientists began to study matter at the smallest scale. Many theories and experiments since then have given us remarkable insight into the fundamental structure of matter.

At present, the elementary particles can be categorized into two main *families*: fermions (named after Italian scientist Enrico Fermi) and bosons (named after Indian scientist Stayendra Nath Bose). The main difference between the two has to do with their spin, which is simply the intrinsic angular momentum of the particle. Bosons have spin $= n$, where n is an integer, while Fermions have spin $= (n + 1/2)$. Because of their ‘half-integer’ spin, Fermions must obey Pauli’s exclusion principle, while bosons on the other hand may occupy the same space. How these particles interact

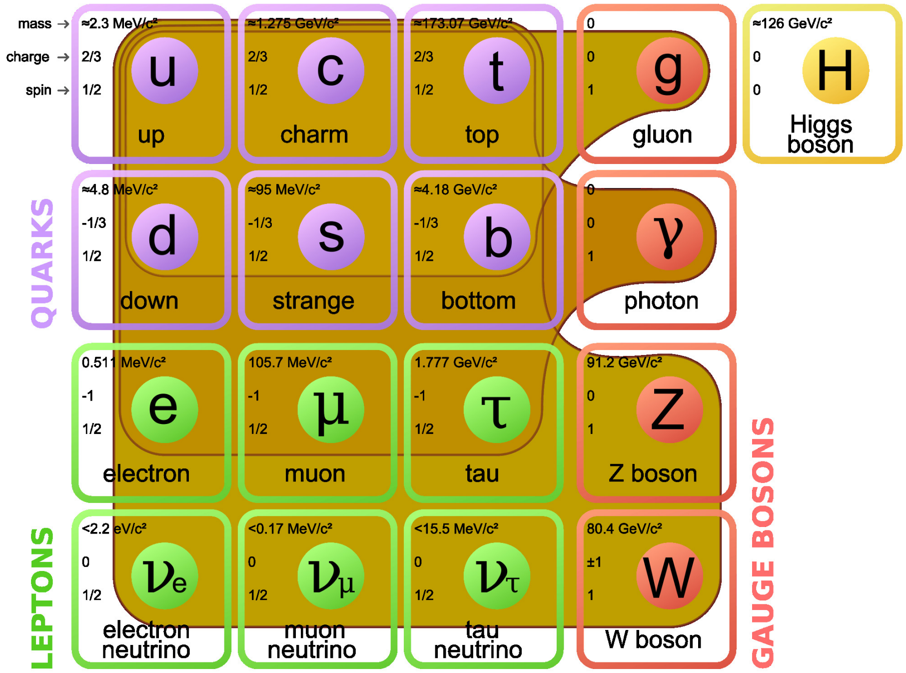

Figure 1.1: The Standard Model

and how they are related to each other is embodied in the single model called the Standard Model of particle physics, a trusted model whose accuracy has been verified by countless experiments over the years. The main features of this model are discussed in the following section.

1.2 The Standard Model

The Standard Model (SM) [1–5] incorporates our current understanding of all known fundamental particles and forces, with the exception of gravity. The SM (shown in Figure 1.1) combines twenty-four building blocks of matter (Fermions) - six leptons, six quarks, and their antiparticles with the four force carriers (Bosons). The SM is a gauge-invariant quantum field theory that provides an interesting picture of the various interactions, mediated by bosons, between fermions. There are three flavours of leptons in the Standard Model: electron (e), muon (μ) and tau (τ). For each flavour there is a charged and neutral lepton. The charged leptons are named according to their respective flavours and carry an electric charge of -1, while the neutral leptons are called neutrinos (shown in Figure 1.1). The three flavours can be written as three families as shown below:

$$\begin{pmatrix} e \\ \nu_e \end{pmatrix}, \begin{pmatrix} \mu \\ \nu_\mu \end{pmatrix}, \begin{pmatrix} \tau \\ \nu_\tau \end{pmatrix}. \tag{1.1}$$

While we observe more matter in the universe than anti-matter, the SM predicts that for each lepton there exists an anti-lepton, which has the same mass but opposite charge. In addition to the electric charge, the leptons (and anti-leptons) carry weak isospin.

There are six flavours of quarks in the SM. These are: up, down, charm, strange, top and bottom. The SM predicts that for each quark there exists an anti-quark which has the same mass but opposite electric charge. These quarks (and anti-quarks) carry the following types of charges:

- Colour charge (red, green or blue),
- Fractional electromagnetic charge,
- Weak isospin.

At low energies, quarks exist only as colourless (that is, they must either consist of a combination of all three colours or anti-colour charges, or of a colour-anti-colour pair) bound states known as hadrons. Hadrons consisting of three quarks, such as the proton and neutron, are known as baryons. Hadrons consisting of two quarks, are known as mesons, colour/anti-quark pair, for example, the π^0 and the B^0. The quarks can be grouped into three families:

$$\begin{pmatrix} u \\ d \end{pmatrix}, \begin{pmatrix} c \\ s \end{pmatrix}, \begin{pmatrix} b \\ t \end{pmatrix}. \tag{1.2}$$

The matter particles interact with each other through the exchange of force-carrying particles corresponding to the electromagnetic, weak, and strong forces. The four fundamental forces known to us in nature are :

- The strong force described by the $SU(3)$ symmetry group
- The weak force described by the $SU(2)$ symmetry group
- The electromagnetic force described by the $U(1)$ symmetry group
- The gravitational force. (This force is many orders of magnitude weaker than the other three fundamental forces and cannot yet be incorporated into the SM).

The structure over the SM comes from the symmetry group $SU(3) \times SU(2) \times U(1)$ [6, 7]. The forces are briefly discussed below:

The Strong Force The strong force is mediated by gluons. A gluon is a massless particle that carries a colour charge. There are eight gluons in total, all are identical except for their colour charge. The gluons carry colour charge and interact with particles that carry colour charge, therefore they are able to interact with each other. This is a non-abelian behaviour in terms of their symmetry group. The strong force coupling parameter, α_S, decreases with energy and it's behaviour is described by the equation:

$$\frac{\partial \alpha_S^2(Q^2)}{\partial \ln(Q^2)} = -(11 - \frac{2n_f}{3})\frac{\alpha s}{4\pi} \tag{1.3}$$

where Q^2 is the energy scale of the interaction and n_f is the number of families of fermions. In the SM, $n_f = 6$.

The Electromagnetic Force The mediator of the electromagnetic (EM) force is the photon (γ), which is massless and couples to charged particles, although itself is uncharged. As photon is a massless particle, the range of the EM force is infinite.

Force	Gauge Boson	Charge	Spin	Mass (GeV/c^2)	Range	Rel. Strength
Strong	Gluon (g)	0	1	0	10^{-15}	1
EM	Photon (γ)	0	1	0	∞	1/137
Weak	$W^{\pm}$	± 1	1	80.385 ± 0.015	10^{-18}	10^{-5}
	Z^0	0	1	91.188 ± 0.002		
Gravity	Graviton (G)	0	2	0	∞	10^{-38}

Table 1.1: The four fundamental forces and their basic properties.

The Weak Force The weak forces are the mediated by $W^{\pm}$ and Z^0 bosons. These are massive particles. Their masses have been determined experimentally, 80.385 ± 0.015 GeV for the W$^{\pm}$ bosons and 91.1876 ± 0.0021 GeV for the Z^0 [8]. The high masses of these bosons imply that they can only act over short distances. The Table 1.1 lists the four fundamental forces and their basic properties.

1.2.1 Electroweak Unification and the Higgs Field

The coupling strength of both the EM and the weak forces increases with energy. The Glashow-Salam-Weinberg model [9–11] showed that the EM and weak forces combine to yield the electroweak (EW) force at high enough energies, which is thus described by a $SU(2) \times U(1)$ group. From the gauge invariance requirement, this results in four gauge bosons. The $SU(2)$ component gives three of these: W^1,W^2 and W^3, and since $SU(2)$ is non-abelian, this implies that these three bosons interact with each other. The remaining gauge boson B arises from the $U(1)$ group. The photon and weak bosons may then be written as a mixture of the $SU(2) \times U(1)$ gauge bosons as follows:

$$W\pm = \frac{1}{\sqrt(2)}(W^1 \mp W^2) \tag{1.4}$$

and

$$\begin{pmatrix} Z \\ \gamma \end{pmatrix} = \begin{pmatrix} \cos\theta_W & \sin\theta_W \\ -\sin\theta_W & \cos\theta_W \end{pmatrix} \begin{pmatrix} W^2 \\ B \end{pmatrix} \tag{1.5}$$

where θ_W is known as the weak mixing angle and is determined from the coupling constants of the $SU(2)$ (g_W) and $U(1)$ $(g\prime_W)$ groups such that:

$$\sin\theta_W = \frac{g\prime_W}{\sqrt{g_W^2 + g\prime_W^2}} \tag{1.6}$$

With their respective forces combined, the discrepancy between the masses of the weak bosons and that of the photon was unexplained. In 1964, three groups of researchers: Brout and Englert [12], Guralink, Hagen and Kibble [13] and Higgs [14] proposed a mechanism to explain this. Higgs proposed a massive scalar boson, which we call Higgs boson with the Higgs field. The Higgs mechanism allowed for the symmetry of the massless bosons to be spontaneously broken through interacting with a complex scalar field ϕ:

$$\phi = \begin{pmatrix} \phi^2 \\ \phi^0 \end{pmatrix} \tag{1.7}$$

The field ϕ has potential energy V:

$$V = \mu^2 \phi^\dagger \phi + \lambda(\phi^\dagger \phi)^2 \tag{1.8}$$

with $\mu^2 \to 0$ and $\lambda \to 0$. Setting $\phi^+ = 0$ at the minimum of the potential V^0 (with ϕ^0 the field at the minimum potential) and allowing ϕ^0 a non-vanishing component:

$$\phi^0 = \frac{1}{\sqrt{2}}\begin{pmatrix} 0 \\ v \end{pmatrix} \tag{1.9}$$

then the potential has minima at $\phi^0 = \pm v$. At some point in the early universe then, the Higgs field acquired a vacuum expectation value (or VEV) at v, meaning that it now has an inherent value at every point in space:

$$v = \frac{|\mu|}{\sqrt{\lambda}} \tag{1.10}$$

v has a value of approximately 246 GeV [8] Taking perturbations h about v,

$$\phi = \phi^0 + h = \frac{1}{\sqrt{2}}\begin{pmatrix} 0 \\ v + h \end{pmatrix} \tag{1.11}$$

Using this expression for ϕ in the potential then gives

$$V = V_0 + \lambda^2 v^2 h^2 \tag{1.12}$$

The Higgs boson corresponds to these perturbations in ϕ, with a mass term $M_H = \sqrt{2v}$. Masses of the EW bosons are then given by the following expressions:

$$M_{W^\pm} = \frac{vg}{2} \tag{1.13}$$

$$M_Z = v\frac{\sqrt{g + g\prime}}{2} \tag{1.14}$$

$$M_\gamma = 0 \tag{1.15}$$

where g and $g\prime$ are the coupling constants of the $U(1)$ and $SU(2)$ groups. The

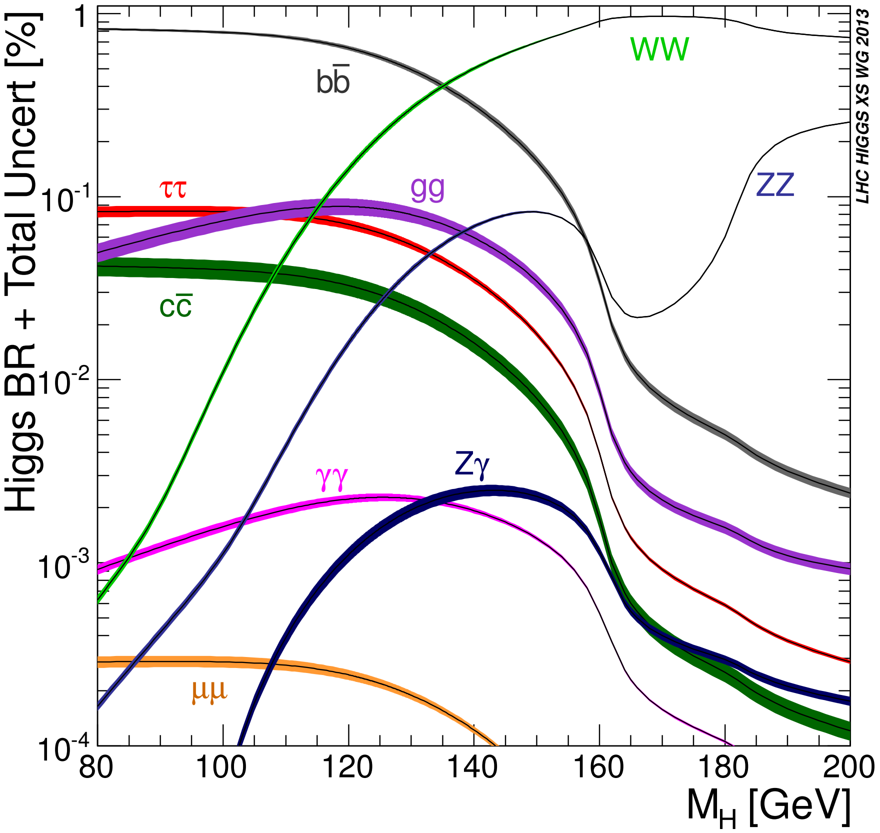

Figure 1.2: Branching ratios of the Higgs for a range of Higgs masses.

Higgs boson decays into pairs of massive particles, provided that this is kinematically allowed. Figure 1.2 shows the branching ratio of a Higgs over a range of mass values. Note that a Higgs decay to two photons is included, even though there is no direct coupling between a Higgs and a massless particle - this decay occurs indirectly through either a boson or fermion loop.

In 2012, the experiments at the Large Hadron Collider (LHC) discovered a Higgs like boson. Later in 2013, the discovery of the Higgs boson was confirmed with mass of $\approx$ 125 GeV [15, 16]. This was a huge success for the Standard Model and Higgs and Englert earned the 2013 Nobel Prize in Physics. In 2012, the experiments at Tevatron Fermilab, DØ and CDF, saw the first evidence of the fermionic decay specifically to $b\bar{b}$ of such particle [17].

1.3 Motivation and Theoretical aspects

The theory that explains how quarks and gluons interact is called Quantum Chromo Dynamics (QCD) [18]. It is analogous to Quantum Electro Dynamics (QED) [19] which deals with interactions involving electrons and photons. As discussed above, quarks and gluons carry colour charge and interact with particles that carry colour charge, which makes it very interesting to study these particles and their interactions. The way we study these particles is by colliding them together and observing what comes out and in what direction. It is important to note that quarks have electric charge as well as colour charge, but gluons only carry colour charge. So photons can interact with quarks but they can not interact with gluons. Thus we can study QCD by smashing quarks and watching how many quarks and gluons come out and in what direction. Then we can compare that to how many and in what directions photons come out in same kind of collisions. This gives us complementary information about the nature of quarks and gluons and their relative arrangements.

Because of this electromagnetic nature of photon-quark interactions, the photons produced in the final state of fundamental 2 → 2 QCD interactions provide a valuable source of information about the quark-gluon dynamics. The collisions of quarks at high energy, for example proton and anti proton ($p\bar{p}$) collisions, produce photons with a high transverse momentum. These are called "direct" because they are produced directly from parton-parton interactions (and not from hadron decays such as $\pi^0, \eta, K_s^0, \omega$). This means they emerge unaltered from the hard interactions of quarks. These direct photons being produced in association with heavy (c or b) quarks give us a possibility to better understand relevant parton scattering dynamics and the proton/antiproton properties, and consequently allow us, in particular, to measure the momentum distributions of its constituent heavy quarks. Hence, the study of direct photon production in association with a heavy quark pair ($Q\bar{Q}\gamma$ for Q = t,b) is a very significant part of the physics of both the Tevatron and the LHC. The study of the Z boson production in association with heavy flavour jets is also essential. This is because Z plus heavy flavour jets production forms an irreducible background for the $ZH \rightarrow llb\bar{b}$ searches, as their final states have an identical signature of a Z boson and at least one b or c quark jet.

A collision between proton and antiproton is considered to be an interaction between just one constituent but given that hundereds of particles can be formed by these collisions, a cross-section is measured which represents how likely a particular interaction will occur, like " a quark and an antiquark producing a photon in association with one or more heavy flavour jets". The measurement of production cross section of direct photon or Z boson in association with heavy flavour quarks is motivated by the need of testing the theoretical predictions and to extract the certain parameters to tune the theory. Hence, it is important to understand how these theoretical predictions are calculated with which experimental data can be compared. For this we need to review the basics of QCD and perturbative Quantum Chromodynamics (pQCD) expanded with the parton model. As we know, QCD is the quantum field theory related to the interactions due to strong force, to describe this theory let us introduce the classical lagrangian :

$$L = -\frac{1}{4}F_a^{\mu\nu}F_{a\mu\nu} + \bar{\psi}_j(i\gamma_\mu D_{jk}^\mu - M_j\delta_{jk})\psi_k \tag{1.16}$$

where

$$D_{jk}^\mu = \delta_{jk}\partial^\mu + ig(T-a)_{jk}G_a^\mu \tag{1.17}$$

$$F_a^{\mu\nu} = \partial^\mu G_a^\nu - \partial^\nu G_a^\mu - gf_{abc}G_b^\mu G_c^\nu \tag{1.18}$$

where $a = 1,2,3,....8$ and $j,k = 1,2,3$ are the color indices of gluons and quarks, respectively. $F_a^{\mu\nu}$ is the gluon tensor and D_{jk}^μ is the covariant derivative acting on the quark field. The f_{abc} are the structure constants of $SU(3)$, M is the mass matrix, and g is the coupling constant. In principle, QCD can help us know the arrangement of gluons and quarks inside a proton or an anti proton. But practically, it is non perturbative in this area, so it is not possible to obtain the distributions of quarks and gluons from basic principles. In this case, parton model comes into play which offers phenomenological picture.

The Parton Model The parton model explains certain features of deep inelastic scattering. Experiments in the 1960's and 1970's showed that there was a structure to many mesons and baryons that were known at that time. The study of deep inelastic scattering can provide information about the structure of the nucleons and the properties of the constituent particles.

We only need a simple version of QCD to build the useful parton model. In the parton model, the high energy inelastic collision between, for example, a proton and an anti proton can be considered as an elastic collision between a single parton in the proton and a single parton in the anti proton. Then we can assume that the quarks and gluons inside the proton are independent. This assumption is justified by the approximation that if the time scale of the hard scattering is much shorter than the time scale on which the partons inside the proton interact, then the scattered parton is free. Following this approximation, the proton can be described by a function $G_{a/A}(x)$ which represents the probability of finding parton a in the proton A with a momentum fraction between x and $x + dx$. These functions are called parton distribution functions (PDFs) because they provide the probability distribution of partons within the hadron. The hard scattering of partons a and b can be described by two body Born scattering. The main point to note here is that since the particles from which partons a and b arise do not know anything about the interaction in which a and b may be involved. Thus the parton distribution functions do not depend on the details of the hard scattering in the parton model and we can say that they are universal. In other words, $G_{a/A}(x)$ can be measured in one process and applied to calculate a prediction for a different process. Also as strongly interacting quarks and gluons are not observed as free particles in nature, they must recombine to form particles that we observe. This process is known as fragmentation. Thus to observe some particular particle, for example, an energetic photon, we must form a function that gives the probability that a quark or a gluon fragments into a photon. The probability that a particular parton d fragments into a photon with momentum fraction z and $z + dz$ of the parton d is denoted by the function $D_{\gamma/d}(z_\gamma)$. Like the parton distribution functions, this function is universal, and can be derived from various hard scattering processes. In the parton model the cross section for inclusive $\gamma + X$ production in proton-antiproton collisions can be written as the incoherent sum of all the sub-processes possible [20]:

$$
\begin{aligned}
&E_\gamma \frac{d\sigma}{d^3p_\gamma}(p\bar{p} \to \gamma + X) = \\
&\qquad \sum_{a,b,c,d} \int \mathrm{d}x_a \, \mathrm{d}x_b \, \mathrm{d}z_c G_{a/p}(x_a) G_{b/\bar{p}}(x_b) D_{\gamma/d}(z_\gamma) \frac{\hat{s}}{z^2\pi} \frac{d\hat{\sigma}}{d\hat{t}}(ab \to cd)\delta(\hat{s} + \hat{t} + \hat{u}). \quad (1.19)
\end{aligned}
$$

This equation can be represented schematically as shown in Figure 1.3

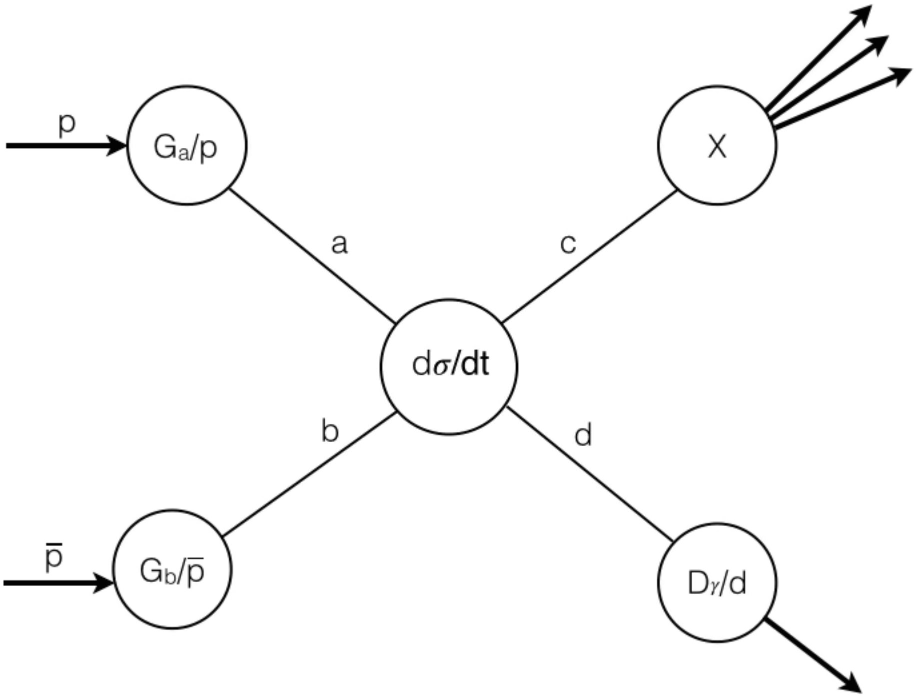

Figure 1.3: A schematic view of the parton model in which X represents the particles that are integrated over in the final state to obtain semi-inclusive cross-section.

Here, the variables $\hat{s}, \hat{t}, \hat{u}$ are the Mandelstam variables in the center of mass frame of the partons and the delta function imposes the conservation of momentum and energy. We can define these and several other useful variables as follows. Let p_A and p_B be the four momentum of proton and anti-proton.

$$s = (p_A + p_B)^2$$

and the momenta of the partons can be written as

$$p_a = \frac{x_a\sqrt{s}}{2} \text{ and } p_b = \frac{x_b\sqrt{s}}{2}$$

Finally, we can define the Mandelstam variables in the center of mass frame as:

$$\hat{s} = x_a x_b s \qquad \hat{u} = -x_b p_T \sqrt{s} e^y \qquad \hat{t} = -x_a p_T \sqrt{s}$$

$$\hat{s} = (p_a + p_b)^2 \qquad \hat{u} = (p_c - p_b)^2 \qquad \hat{t} = (p_c - p_a)^2$$

$$\hat{u} = -\frac{\hat{s}}{2}(1 + cos\theta^*) \qquad \hat{t} = -\frac{\hat{s}}{2}(1 - cos\theta^*)$$

In the parton model the scattering is divided into a "soft" part which is represented by the PDFs and the fragmentation functions and the "hard" scattering. The fact that the parton distribution functions are same for any process and depend only on x (this property is called scaling) contributes to the success of the parton model. However, in QCD there is no such division and no requirement of scaling. So lets consider the description of the hard scattering process denoted by $\mathrm{d}\hat{\sigma}/\,\mathrm{d}\hat{t}$. Such a description must have QCD and QED also because photon interacts electromagnetically. Because of the dominance of the strong force over the electromagnetic force, we can write the cross section as a series in terms of α_s as:

$$\hat{\sigma} = \sigma^{LO}\alpha_{EM}\alpha_s + \sigma^{NLO}\alpha_{EM}\alpha_s^2 + ... \tag{1.20}$$

where α_{EM} is the electromagnetic coupling constant. The coupling constant evolves due to the procedure by which the theory is renormalized. Renormalization is the procedure by which the predictions of a theory are made finite by reabsorbing the infinities into the formal parameters of the theory mainly the masses of the quark and the coupling constants. It then depends upon the renormalized masses and coupling constant. After renormalization, one of the basic parameters of the theory, the coupling constant, is then a direct function of dimensional scale parameter μ: $\alpha_s = \alpha_s(\mu)$. However, the observable physical quantities can not depend on the scale parameter, which implies that the formal parameters of the theory must depend on μ in some particular way. As a result, it is possible to derive the function that describes the change of $\alpha_s(\mu)$ with momentum scale of the scattering. In QCD, its slope in μ is negative which means that the coupling constant decreases as the momentum scale of the process increases. And $\alpha_s(\mu) \rightarrow 0$ as $\hat{t} \rightarrow \infty$. In QED, this situation is the opposite where the coupling constant increases with increasing energy. We can understand this in terms of self interaction of the gluons. A virtual gluon can radiate another gluon and hence QCD becomes dominated by processes that involve many soft gluons if they are allowed enough time for such radiation to occur. On the other hand, in QED, a virtual photon can not radiate other photons, but it can decay into virtual fermion pairs. This produces a screening effect which becomes less important at small scales. Therefore, higher order corrections are more important at higher energies.

In short, higher order corrections in QED are more important at high energies whereas in QCD, higher order corrections are more dominating at low energies. This asymptotic decrease in the renormalized strong coupling to zero as Q^2 increases is called asymptotic freedom.

Also, the increase in $\alpha_s(\mu)$ at low momentum scales is responsible for binding quarks and gluons into hadrons. As a result, the quarks and gluons are never observed in isolation. Thus in high energy collisions, a gluon or a quark with large momentum must hadronize into a "jet" in final state. Because gluons carry color, the force between two colored objects, for instance a pair of quarks, does not decrease with the distance between them but instead remains approximately constant. As a result that the energy of the gluons between the two quarks increases, and when energy is large enough, a new quark antiquark pair is created [21].

In terms of perturbation theory, if one were mathematically capable enough to calculate the theory to all orders, one would always get the correct result which would be independent of the choice of scale μ. Therefore, the better one is at calculating, the less one relies on absorbing higher order corrections into the renormalized coupling constant and the answer is dependent less on the choice of μ. Thus, the sensitivity of a particular calculation on the choice of μ can be taken as the uncertainty in the theoretical prediction. Thus, the calculation is divided into calculable part and a part which must be extracted from the experiment; we can now understand parton model as leading order QCD. The separation between the hard scattering and the soft PDFs is now arbitrary. We can introduce a new scale λ, which separates the hard scattering from PDFs. So now, $G_{a/A} = G_{a/A}(x, \lambda)$ as well as $\alpha_s = \alpha_s(\mu)$. Now there is a natural scale for λ and μ, the momentum exchange for the process Q^2. It is common to set $\lambda^2 = \mu^2 = Q^2$ in a given process. In order to make predictions, we must have a way to evolve the PDF's to any desired scale. The experimental input required is the fractional momenta of quarks with respect to their parent hadrons (x) and the energy scale at which these measurements were made (Q^0). This information is then used to set the boundary conditions for the DGLAP equations [22–24], which are differential equations whose solutions describe the evolution of these quark and gluon parameterizations as a function of Q^2.

The calculations that provide a complete treatment of all sub-processes through next to leading order have been performed [25] and the numerical techniques [26] equations were used. Parameterizations of the PDFs were taken from the CTEQ collaborations [27]. The production of a photon in association with one or more heavy flavour quarks are reviewed next in more details.

1.3.1 Production Mechanism

Two main sources of the associated photon (γ) and heavy flavor quark (b) production are the “Compton”-like scattering

$$b + g \to b + \gamma \tag{1.21}$$

and the annihilation subprocess

$$q + \overline{q} \rightarrow g + \gamma \tag{1.22}$$

during which the final state gluon splits into a heavy quark pair $g \rightarrow b\bar{b}$. So main source of $\gamma + 2b$-jet is ISR/FSR where we have gluon radiated in initial state or final state which splits in $b\bar{b}$. Figure 1.4 shows the fractional contributions of the $bg \rightarrow b\gamma$ subprocesses to the total cross section of associated production of a direct photon with a heavy flavor quark. Here, the photons are in the central ($|\eta| < 1.0$) and forward ($1.5 < |\eta^\gamma| < 2.5$) rapidity regions. The curves are obtained using signal processes (1) and (2) simulated with PYTHIA 6.4 event generator [28]. The Compton scattering process is dominant up to $p_T^\gamma \simeq 80$ GeV with the central photons and $50 - 60$ GeV with the forward photons.

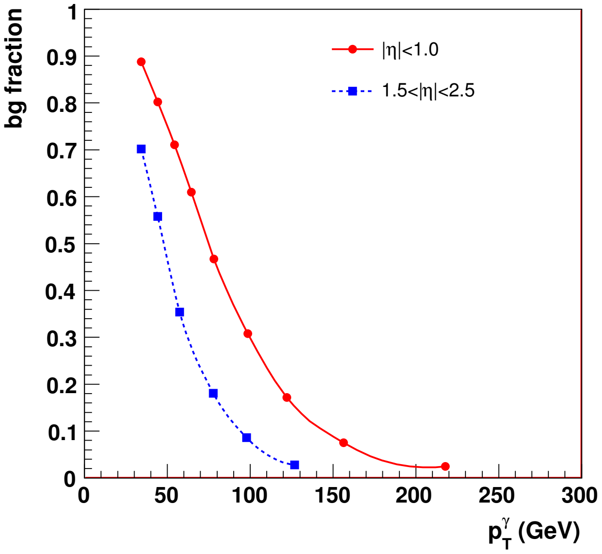

Figure 1.4: Fractional contribution of the $bg \rightarrow b\gamma$ subprocess to the associated production of direct photon and b-jet in the events with photons in the central and forward rapidity regions.

At tree level, the direct photon production in association with a $b\bar{b}$ pair consists of two partonic subprocesses, namely $q\bar{q} \rightarrow \gamma b\bar{b}$, $g\bar{g} \rightarrow \gamma b\bar{b}$ as shown in Fig 1.5.

Figure 1.6 shows the tree level Feynman diagrams contributing to the production of $Z + b\bar{b}$ events via gluon splitting (top two diagrams) and gluon fusion (bottom three diagrams).

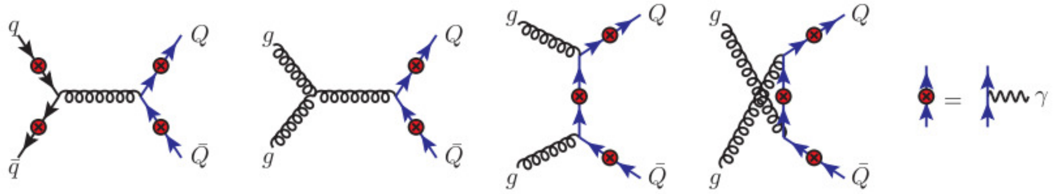

Figure 1.5: Tree-level Feynman diagrams for $p\bar{p} \to Q\bar{Q}\gamma$ production, corresponding $q\bar{q} \to \gamma b\bar{b}$, $g\bar{g} \to \gamma b\bar{b}q\bar{q} \to \gamma b\bar{b}$, $g\bar{g} \to \gamma b\bar{b}$ subprocesses. For each diagram, the red circled crosses correspond to all possible photon insertions [29].

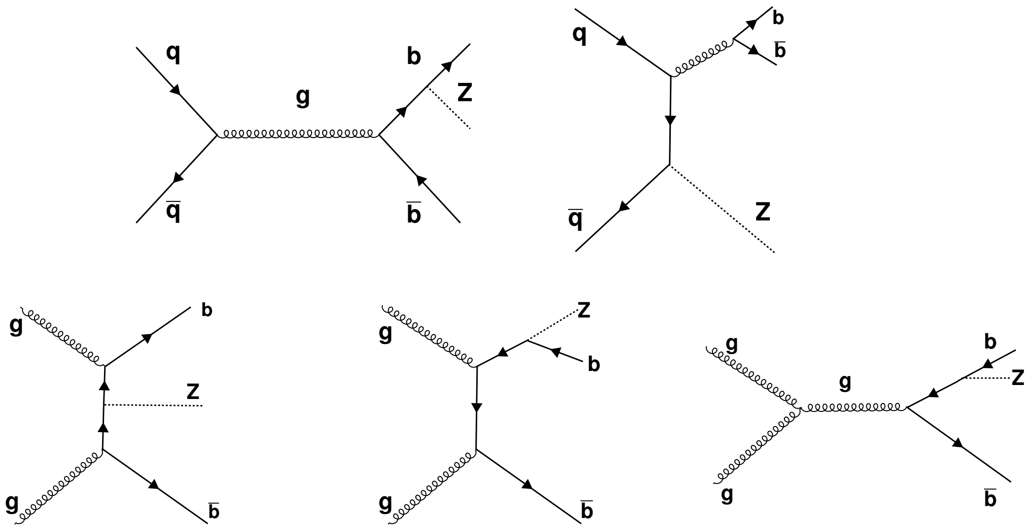

Figure 1.6: Tree level Feynman diagrams for $Z + b\bar{b}$ events via gluon splitting (top two diagrams) and gluon fusion (bottom three diagrams).

The production cross section for the Compton scattering should be sensitive to the b quark (as well as to the gluon) densities inside the colliding hadrons and may give us an opportunity for tuning the parameters of those PDFs which still have noticeable uncertainties. Those uncertainties, on the theory side, come from a scheme dependence in the treatment of the heavy flavour quarks and the choice of specific parameters (like heavy quark thresholds) in some schemes [30–33]. On the experimental side, they are caused by a lack of relevant experimental data:

inclusive b-jet production in D0 and CDF at $\sqrt{s} = 0.63$ and 1.8 TeV, performed in Run I [34, 35] (most of which showed a systematic discrepancy with theory up to a factor 2.5), $Z + b$ production in D0 and CDF [36–38], CDF results on $\gamma + b$ [39], and, finally, D0 result with $\gamma + b$ cross section measured with central photon and jet [40]. A series of measurements involving γ and $b(c)$-quark final states at have been performed by the DØ and CDF collaborations [41–43].

This thesis presents first measurement of the inclusive $\gamma + 2b$-jet differential cross sections as a function of the photon p_T in $p\bar{p}$ collisions at $\sqrt{s}$ =1.96 TeV which is an extension of the previous $\gamma + b$-jet measurement. The results are based on data corresponding to an integrated luminosity of 8.7 ± 0.5 fb^{-1} [44] collected with the DØ detector from June 2006 to September 2011 at the Fermilab Tevatron Collider. In addition to that, the ratio of cross sections for the inclusive production of $Z + 2$ b-jet events to $Z + 2$-jet events was also measured using full Run II Tevatron data collected by the DØ experiment corresponding to the integrated luminosity of 9.7 fb^{-1}. Studies of Z boson production in association with a bottom and abti-bottom quark provide important tests of the predictions of perturbative quantum chromodynamics (pQCD) [45–47]. The ratio of cross sections for the $Z + b$-jet to $Z + 1$-jet production have been measured by the D0 experiment [48] which agrees well with QCD calculations.

The main aim in carrying out these measurements is to provide results which can be compared to theoretical predictions. These comparisons will provide information about the b-quark parton density in nucleons which will help us understand the b-quark parton density functions [29]. It will help in directly constraining the b-quark parton distribution and explore the presence of an intrinsic b-quark density in nucleons as opposed to a purely perturbative b-quark density obtained from the evolution of the gluon parton density. Constraining and understanding the b-quark parton density will play a crucial role in improving the accuracy with which other important processes like the associated production with weak gauge bosons (W/Z

+ b), a background to Higgs production, and the associated production with a scalar/pseudoscalar (H/A + b), can be predicted. This has been the main aim of present work. The work has been done in collaboration with DØ experiment but the analyses have been performed by me. During my Ph.D, I visited Fermilab twice to perform the data analysis and work with experts.

1.4 Overview

In this chapter, the basic ideas of particle physics are introduced along with the theoretical aspects of the present work. Also the motivation and the aim behind the study has been established. Next chapter discusses the Fermilab Accelerator complex and DØ detector. Chapter 3 lists the data samples used for the measurement and details of Monte Carlo Simulations samples used for the study. Chapter 4 introduces the algorithms used in identifying the particles needed in this study. Chapter 5 presents $\gamma + 2b$-jet differential cross section measurements. It enumerates the requirements placed on these objects including cross section calculations for direct photon plus heavy flavour jets and results for the ratio of cross sections of $\gamma + 2b$-jet to $\gamma + b$-jet. Chapter 6 presents measurement of ratio $\sigma(p\bar{p} \to Z + 2\ b\text{ jets})/\sigma(p\bar{p} \to Z + 2\text{ jets})$. It discusses the requirements placed on events with Z plus heavy flavour jet and results for the ratio of inclusive cross section calculations. Finally chapter 7 presents a summary and conclusions of the present work.

Chapter 2

The Experimental Setup

The study of collisions of particles at high energy is one of the most crucial ways of understanding the fundamental structure of matter. According to the famous Einstein equation $E = mc^2$ the kinetic energy of the colliding particles is converted into the rest energy of new particles. In this way we can produce and study particles which are not present under normal conditions in nature, like heavier quarks and intermediate bosons. Study of these particles is important for developing a full picture of the structure of matter and the fundamental forces. To look deeper into the structure of matter, or to produce new heavier particles, the higher energy of the colliding particles is needed. Equally important is high intensity of the collisions, as the interesting processes are usually very rare. Thus, we build colliders to be bigger, more functional, and more expensive than their predecessors. The Tevatron has been one of such accelerators. Located at Fermi National Accelerator Laboratory, in Batavia, IL, U.S.A, the Tevatron was used to collide bunches of protons and antiprotons at a center of mass energy $\sqrt{s} = 1.96$ TeV.

The Tevatron was shutdown on Sept 30^{th} 2011 after 26 years of operation. The Figure 2.1 shows the aerial view of the Tevatron ring. This chapter discusses the various components and steps for accelerating particles through the Tevatron and also of the detection processes. The first section describes the Tevatron accelerator complex. In the next section we discuss the main components of the DØ detector followed by the details of the trigger system used to select the events of our interest.

Figure 2.1: The aerial veiw of accelerator complex

2.1 The accelerator

The accelerator system consists mainly of four parts : the proton source, Main Injector, antiproton source, and the Tevatron. The whole system is shown in Figure 2.2 The proton source system is composed of the Pre-accelerator (Preacc), the Linear Accelerator (Linac) and the Booster. The Linac is a Cockcroft-Walton accelerator; it provides a source of negatively charged hydrogen ions (H). During the Tevatron operations, the H gas acquired an energy of 750 keV through a column from the charged dome (-750 kV) to the grounded wall. The H ions were then accelerated by linac from the Preacc to an energy of 400 MeV through two sections: the low energy Drift Tube Linac (DTL) and the high energy Side Coupled Cavity Linac (SCL). After the Linac, the 400 MeV negative hydrogen ions were directed to a thin carbon film which would strip both electrons from the H- ions, and only allow protons into the circular accelerator called the “Booster”. The Booster then accelerated these protons to 8 GeV which were then ready to pass into the Main Injector (MI).

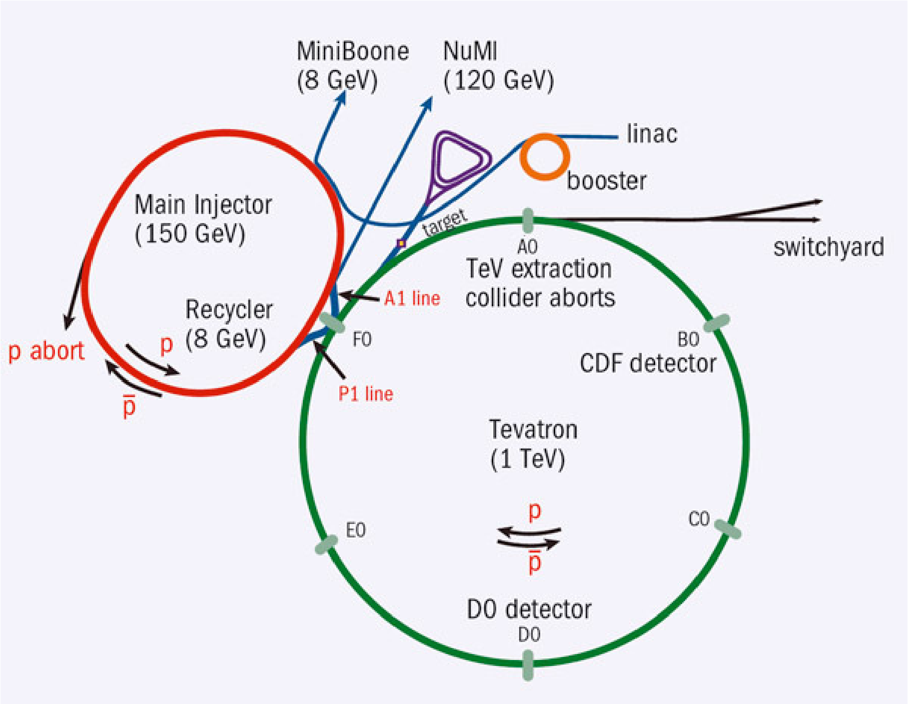

Figure 2.2: The Tevatron overview

The MI is a synchrotron accelerator and has the circumference that is seven times that of the Booster. It can accelerate the proton beam from 8 GeV to either 150 GeV when it was used to generate protons, or to 120 GeV when preparing the anti proton beam for the Tevatron. The antiproton source is composed of the Debuncher and the Accumulator. The proton beam of energy 120 GeV entered the antiproton source and struck a nickel target which produced secondary particles from which 8 GeV anti-protons were collected and sent to the Debuncher. High momentum spread anti-protons were captured in the Debuncher and then stored in the Accumulator. The final step of proton and anti-proton beam preparation occurred in the Tevatron. The Tevatron is the largest synchrotron accelerator at Fermilab and has a circumference of 6.28 km. The electric fields generated in a series of radio frequency cavities provided the energy to accelerate the proton and anti-proton to the final energy of 980 GeV. To steer and focus the beams, superconducting magnets were used which are made from a superconducting niobium/titanium alloy and are kept in $\sim$ 4 K liquid helium. The proton and anti-proton beams were split into 36 individual bunches and spread out in the ring accordingly. The interval between every two bunch crossings is 396 ns. The proton and anti-proton bunches were made to collide at two sets of coordinates around the Tevatron ring where the two detectors were placed: DØ and CDF.

2.2 The DØ detector

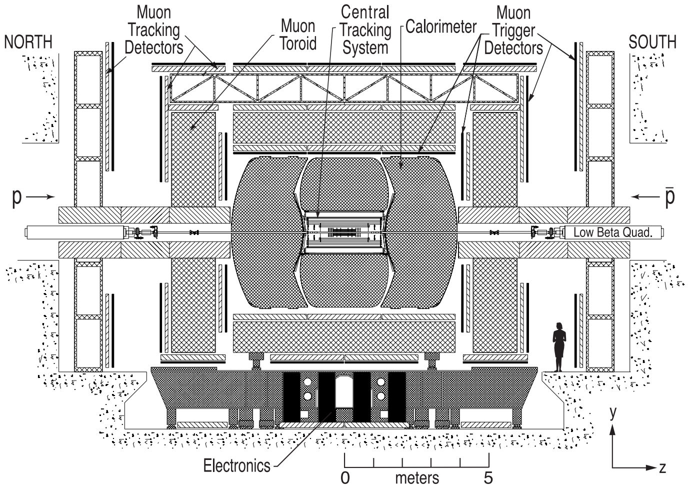

Figure 2.3: The upgraded DØ Detector

The DØ experiment was proposed in 1983 and its operation can be divided into two major periods. Between 1992 and 1996, the DØ detector was used to study high transverse momentum phenomena at $\sqrt{s}$ =1.96 TeV. This period is called Run I. During the 1996-2001 period, along with the Tevatron upgrades [49], the DØ detector was upgraded. After being upgraded [50–52], it consisted a central tracking system, a preshower system, a calorimeter system and a muon system. The DØ experiment began Run II in March of 2001. It operated for a decade until the final shut down in September of 2011. For the present work of thesis, data is analysed from the Run II period and so it is upgraded Run II DØ detector that is described in detail in the next section. Figure 2.3 shows the overview of the DØ detector since the upgrades in 2001.

2.2.1 Coordinates, Kinematic Quantities and Units

It is now important to discuss the coordinate system used for both the DØ detector and the analysis discussed in this thesis. DØ uses a standard right-handed coordinate system with the origin (0,0,0) at the center of the detector. The positive x-axis direction is pointing radially outward from the center of the Tevatron ring, the positive y-axis direction is straight up and the positive z-axis is along the direction of the protons. While DØ is roughly cylindrical in shape, a collision has a spherical rest frame symmetry. This combination is the motivation behind the cylindrical/spherical hybrid system used at DØ (z, θ, ϕ). The angular variables are defined so that $\phi = \pi/2$ is parallel to the positive y-axis, and $\theta = 0$ is coincident with the positive z-axis depicted in the Figure 2.4.

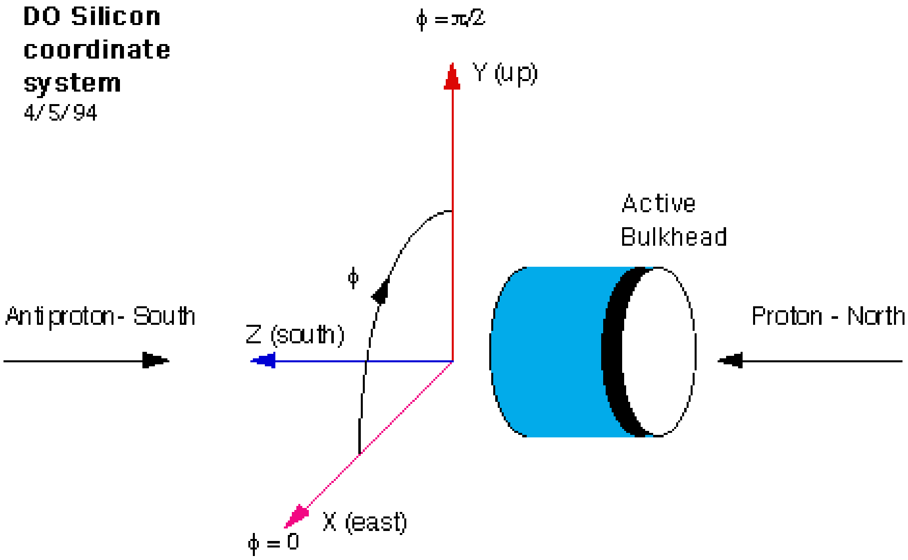

Figure 2.4: DØ Coordinate System

Theta is typically replaced by another quantity called pseudorapidity, denoted as η and defined as:

$$\eta = \ \ln \tan \theta/2 \tag{2.1}$$

In the relativistic limit (E>>m), η is a good approximation of the Lorentz invariant rapidity (y).

$$y = \frac{1}{2} \ln \frac{(E + p_z)}{(E - p_z)} \tag{2.2}$$

It is also convenient to use the 'transverse' momentum instead of momentum, which is the momentum vector projected onto a plane perpendicular to the beam axis:

$$p_T = p \sin \theta \tag{2.3}$$

This is useful due to the fact that in a collision, the momenta along the beam of the colliding partons are not known. However, their transverse momenta are very small compared to their momenta along the beam, so one can apply momentum conservation in the transverse plane. Collisions do not always coincide with the center of the detector. The variance from the center point in the x and y coordinates is very small (40μm) however, it can be large (28 cm) in the z-direction. For this reason, it is often useful to define a detector η and ϕ and a physics η and ϕ. The detector η and ϕ are constructed by using the center of the detector as the center of coordinate system, while physics η and ϕ are constructed by using the primary vertex (PV) as the center of the coordinate system. In general, detector η and ϕ are used when referring to a location in the detector and physics η and ϕ are used when referring to the properties of a particle. A particles 4-momentum vector (E, $\vec{p}$) can be represented as (E, p_T , η, ϕ). The natural unit system with $\hbar = c = 1$ is used, where the mass, momentum and energy are in electron-volts (eV), 1 eV= 1.6×10^{-19}

J in SI units.

2.2.2 Central Tracking System

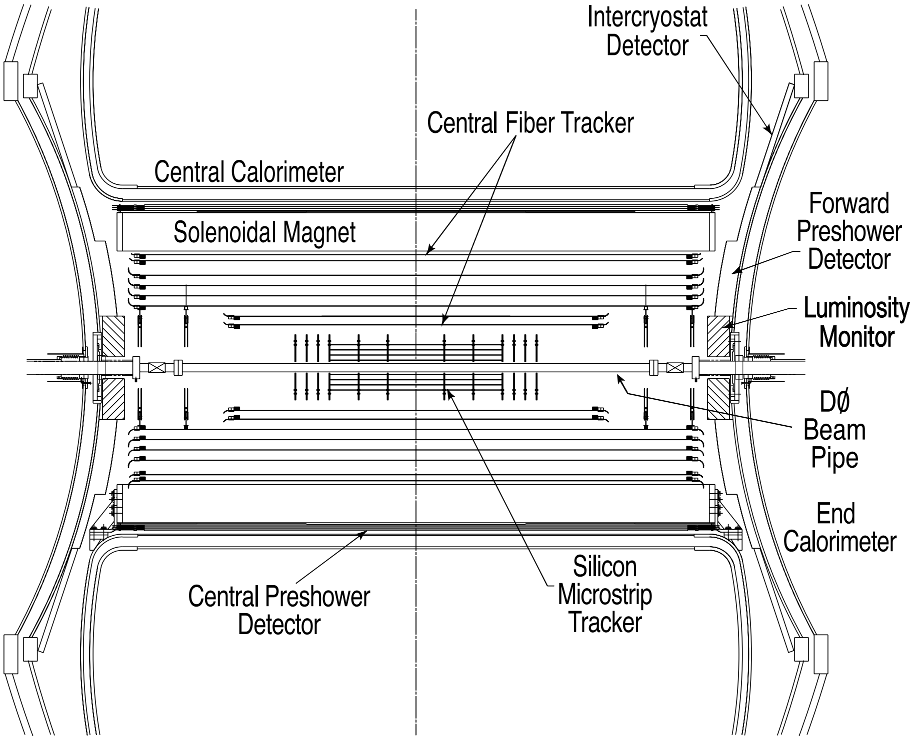

Figure 2.5: DØ Tracking System

The central tracking system consists of the silicon microstrip tracker (SMT) and the central fiber tracker (CFT) surrounded by a 2T solenoidal magnet as shown in Figure 2.5, covering up to $\eta \lesssim 1.7$. The main functions of the tracker include locating the primary interaction vertex with a resolution of $\sim 35\mu$m and providing high precision momentum measurement of charged particles in the central region. It is important for studies of the top quark, electroweak physics, B physics and searches for new phenomena and the Higgs boson.

Silicon Microstrip Tracker (SMT) The SMT [53] is used for tracking and vertexing the events in almost all of the volume of the calorimeter and muon system.

This is achieved by constructing the geometry as in Figure 2.6. There are six barrels in the central region having four concentric silicon readout layers for each barrel. There is an array of sensors on each layer called ladders. When charged particles would pass through the silicon material, it would produce an electron-hole. The sensors collected the signals. There is a total of 432 ladders. The first two layers have twelve ladders each and the outer two layers have twenty four ladders each. After the particle travels through the six barrels, it must pass through the F-disks. F-disk has twelve double-sided wedge detectors at high $|z|$. In the most forward regions, two large-diameter disks called H-disks were placed. These helped to track of charged particles with large $|\eta|$.

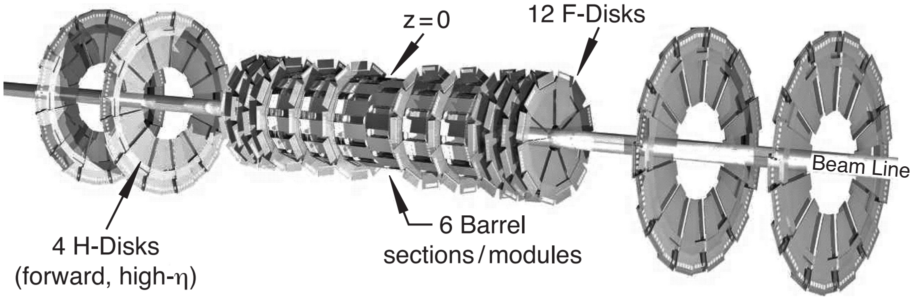

Figure 2.6: DØ Silicon Detector

Central Fiber Tracker (CFT) The Central Fiber Tracker (CFT) is the tracker surrounding SMT [54]. In this part we first explain the geometry of the CFT and then describe the working principle of how charged particles were detected with the CFT. The CFT consists of scintillating fibers installed on eight concentric support cylinders with radii of $(20-52)$cm. The length of the innermost two is 1.66 m and outer six cylinders is 2.52 m. The length difference allowed to place the SMT H-disks. The outer cylinders cover up to $\eta \lesssim 1.7$. Each cylinder has a doublet layer of fibers with one (axial) layer oriented along the beam direction (z) and a second layer (stereo) at a stereo angle in ϕ of $+3^{o}(u)$ or $-3^{o}(v)$. The doublet layers are placed in the order of *zu-zv-zu-zv-zu-zv-zu-zv* from the center moving outward.

The scintillation light in the scintillating fibers was propagated to visible light photon counters (VLPCs) through clear fiber waveguides. The charged particle would start interacting with the scintillating fibers. The scintillating fibers are 835μm in diameter and 1.66 or 2.52 m in length. The scintillating fibers are made of polystyrene (PS) doped with a mixture of organic fluorescent dye called paraterphenyl, a wave-shifter dye 3- hydroxyflavone (3HF), and two claddings. These are assembled into curved ribbons that consist of two layers of 128 fibers each, as shown in Figure 2.7.

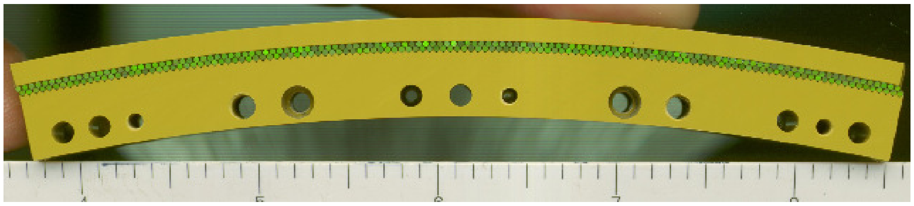

Figure 2.7: A curved ribbon consisting of two layers of scintillating fibers

The curved ribbons were mounted on the support cylinder. Photons at a wavelength of 340 nm were produced by the interaction of charged particles with the PS and paraterphenyl, and then absorbed by 3HF but re-emitted at 530 nm. The re-emitted photons propagated to the clear fiber waveguides from the scintillating fibers. The clear fiber is similar to the scintillating fiber chemically and structurally, but the clear fiber is without any fluorescent dyes. The attenuation length for the scintillating fibers is $\approx$ 5 m and for clear fibers is $\approx$ 8 m. The length of the waveguides range from 7.8 m to 11.9 m. Figure 2.8 shows the routing of the waveguides. The other ends of waveguides are connected to VLPCs where the photons are turned into electronic signals. VLPCs are impurity-band silicon avalanche photodetectors that operate at 9 K. They provided rapid response, good quantum efficiency ($\geq$ 75%), high gain (22000 to 65000), low gain dispersion and the capability of functioning in a high background environment. There are 8 VLPCs installed on a VLPC chip and 128 chips mounted on a VLPC cassette. So each cassette has 1024 VLPC light sensitive pixels, or channels. There are 76800 channels in the CFT in total. The electronic signals from the VLPCs were amplified by the analog front-end boards (AFEs) that are also installed on the cassette body. The AFEs also provided trigger discriminator signals, temperature control, and bias-voltage control. After the passage of scintillating light through all the fibers to VLPCs, the generated signals were usually small, ≈ 6 photoelectrons (pe). The individual channel thresholds were set at around 1.0 pe in order to keep acceptable efficiency for triggers while controlling noise rates. To test the connectivity, monitor the stability of the VLPC readout and calibrate the response of VLPCs channel-by-channel, fast Nichia blue-emitting LED pulsers were used to generate LED spectra as in Figure 2.9.

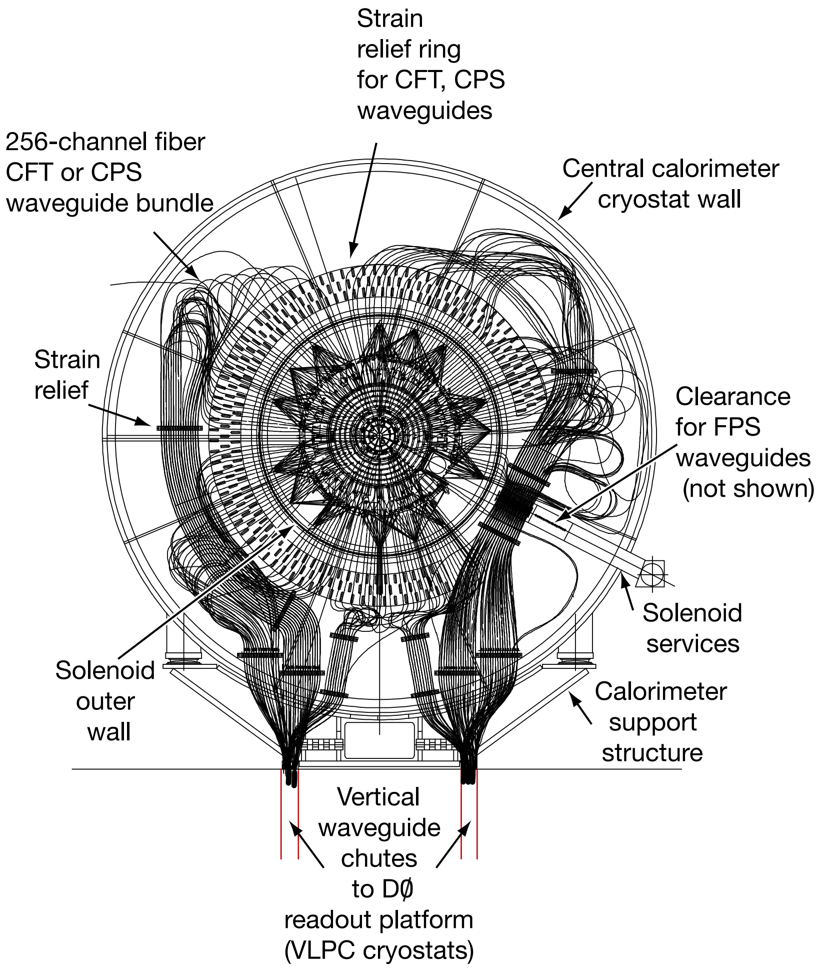

Figure 2.8: A cross section view of the routing of the clear fiber waveguides on the south face of the central cryostat

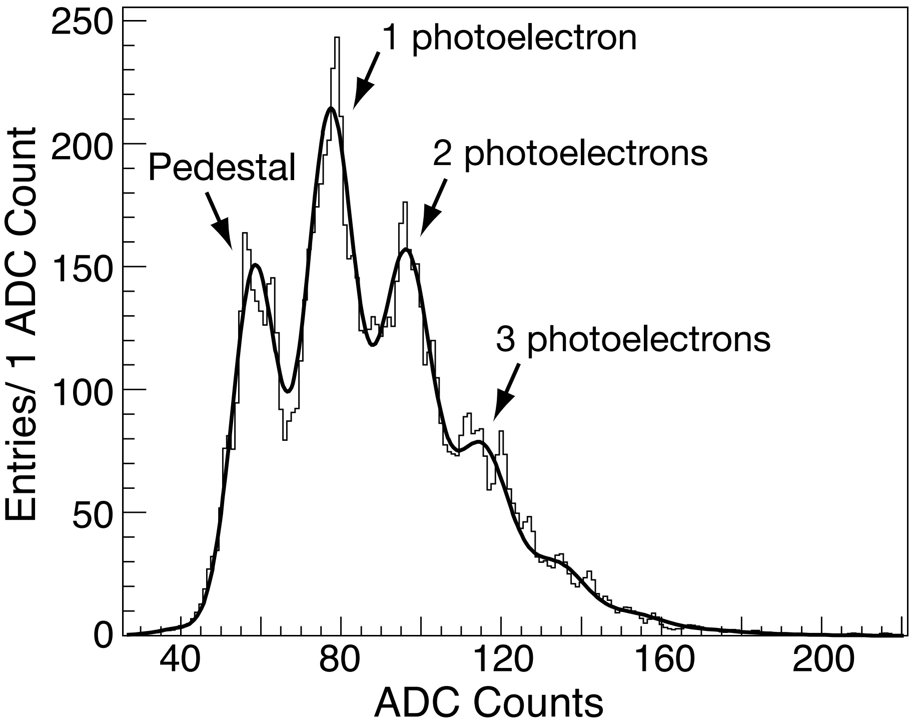

Figure 2.9: An example fit to the LED spectrum from an axial CFT fiber. The solid histogram is the data; the smooth curve is the fit.

2.2.3 Solenoid

The solenoid was added after Run I to optimize the transverse momentum resolution and the track pattern recognition. It provided the magnetic field of 1.9 T with two possible polarity configurations. It is 2.72m in length with inner radii of 1.07 m and outer radii of 1.42m. It is 1.1 radiation length thick. The Figure. 2.10 shows magnetic field lines in the DØ detector with both the solenoid and torodial magnets at full current.

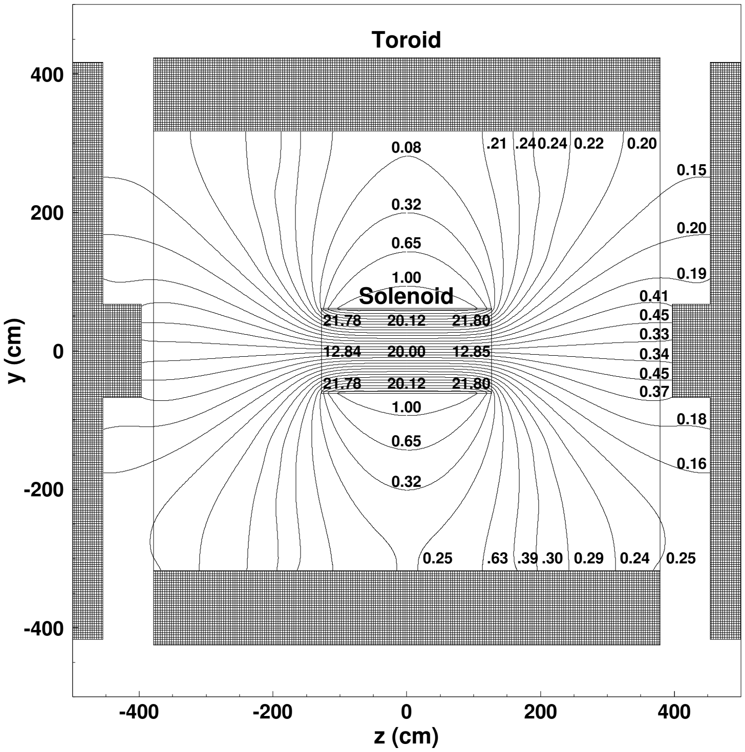

Figure 2.10: Magnetic field lines in the DØ detector with both the solenoid and torodial magnets at full current

2.2.4 Preshower system

The preshower system is a combination of a tracking system and a calorimeter. It was primarily used to match particle tracks to the corresponding calorimeter shower. Some energy from the passing particles would be deposited in the iron solenoid magnet. The preshower system would also help us to measure the energy which was deposited by the particles in the volumes prior, and was therefore useful for identifying the types of particles we were measuring. The preshower system consists of two sub-components. The central preshower detector (CPS) [55] covered the region $|\eta| < 1.3$ and the two forward preshower detectors (FPS) [56] cover $1.5 < |\eta| < 2.5$. Both the CPS and FPS are made from triangular strips of scintillators, as shown in Figure 2.11. Each strip is embedded with a wavelength shifting (WLS) fiber at the center that collected and transfered the emitted light to the read-out.

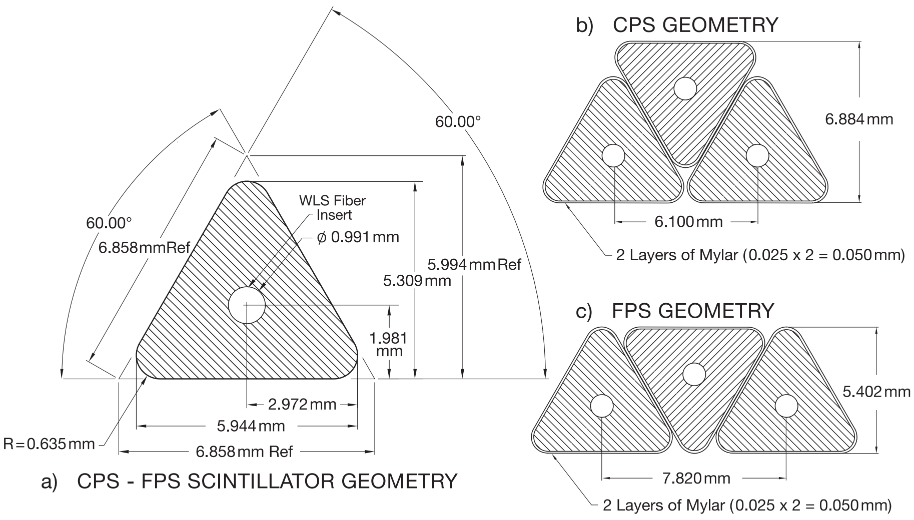

Figure 2.11: Cross section and geometrical layout of the CPS and FPS scintillator strips

Since the triangles are interspersed, there is no dead space between strips. Most tracks passed through more than one strip, allowing for strip to strip interpolations which improved the position measurement, and thus helped us identify the vertices of photons.

Central Preshower (CPS) The CPS consists of three concentric cylindrical layers of triangular scintillator strips. The three layers of scintillator are placed in an axial-*u*-*v* geometry, with a *u* stereo angle of 23.774° and a *v* stereo angle of 24.016°. Each layer is made from eight octant modules and has 1280 strips. The modules consist of two 1/32" stainless steel skins with the scintillator strips in between.

Forward Preshower (FPS) The two FPS detectors are installed on the spherical heads of the end calorimeter cryostats. Each detector is made from two planar layers of scintillator strips. The two layers are separated by a thick lead-stainless-steel absorber with radiation length (X_0) of 2, as shown in Figure 2.12. The upstream layers are known as the minimum ionizing particle (MIP) layers. The downstream layers behind the absorber are called the shower layers. Charged particles going through the detector produced minimum ionizing signals in the MIP layer, allowing measurement of the location (in η, ϕ and z) of the track. However, photons generally did not interact with the MIP layer, but did produce a shower signal in the shower layer.

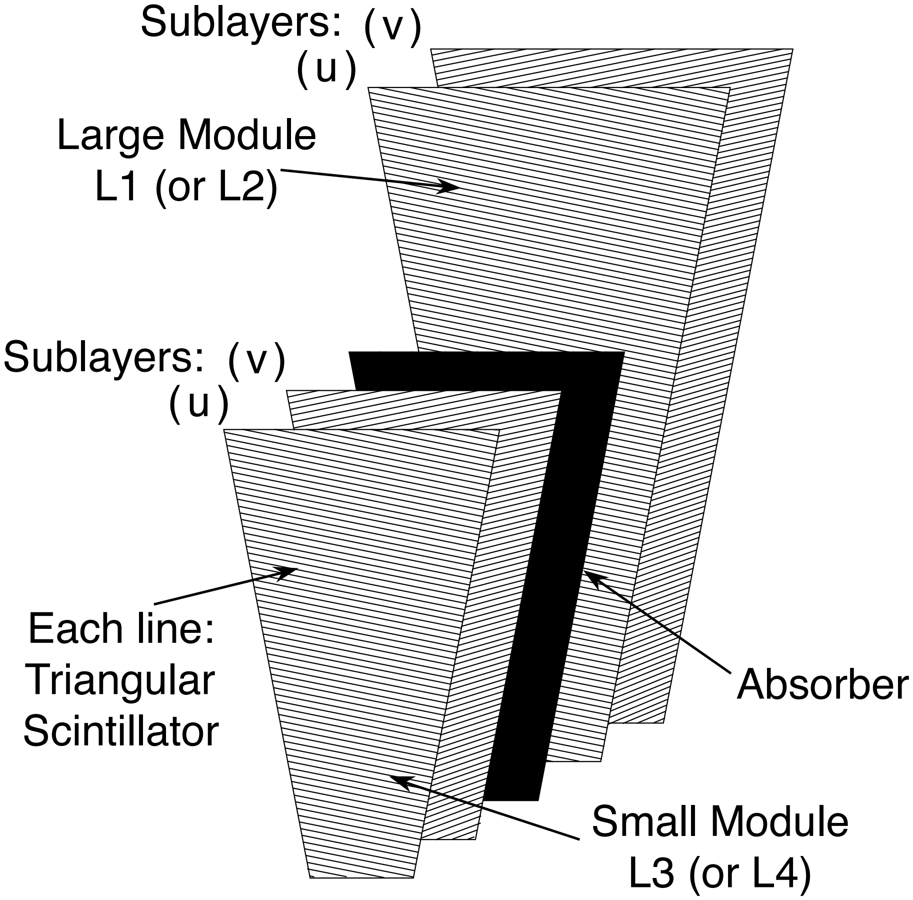

Figure 2.12: Complete $\phi-$segment of a FPS module

2.2.5 Calorimeter

The energy of either charged or neutral particles, was measured with the calorimeter system, which is mainly a uranium/liquid-argon sampling calorimeter system [57]. Since the momentum of a photon cannot be determined with the central tracker, the calorimeter system is the most significant individual sub-detector for this study. The calorimeter system comprises of a central calorimeter (CC) covering $\eta < 1.1$ and two (north and south) end calorimeters (EC) covering the forward region, $1.5 < |\eta| < 4.2$.

The calorimeters have an electromagnetic (EM) section followed outward by fine hadronic (FH) and coarse hadronic (CH) sections. An isometric view of the system geometry is shown in Figure 2.13 [58].

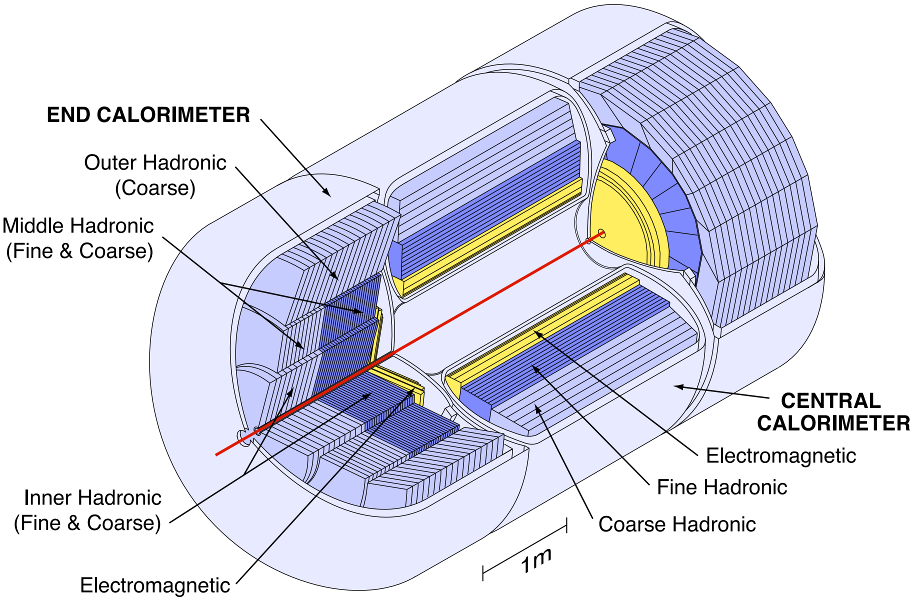

Figure 2.13: DØ Uranium/Liquid-argon Calorimeter

Each calorimeter is built from a number of cells. A typical cell structure is shown in Figure 2.14. It has a thin absorption plate made of almost pure depleted uranium for the EM sections, or uranium niobium (2%) alloy for the FH sections. The CH sections use relatively thick copper in CC or stainless steel in EC plates. The gaps between the absorption plates are filled with the active medium liquid argon. Liquid argon does not confine charges and allowed the ionization produced in electromagnetic and hadronic showers to be collected by the signal boards without amplification. The argon also made the calibration relatively simple, and allowed us to segment the calorimeter into the transverse and longitudinal cells. It also provided good radiation hardness, and relatively low cost per channel for readout electronics.

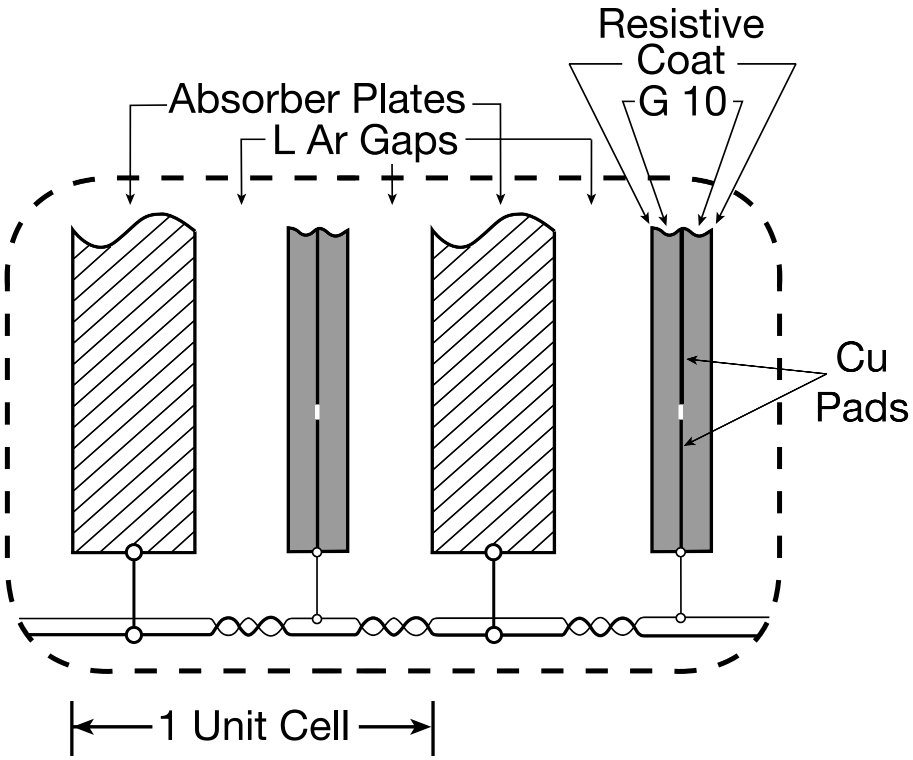

Figure 2.14: Liquid argon gap and signal board unit cell for the calorimeter

Particles traversed and ionized the liquid argon and generated a number of liberated electrons which drifted to the signal boards for readout under a 2.0 kV potential. The electron drift time across the 2.3 mm liquid argon gap is approximately 450 ns. The gap thickness is large enough to observe minimum ionizing particle signals. As shown in Figure 2.15, the readout cells form pseudo-projective towers with a size of $\Delta\eta \times \Delta\phi \approx 0.1 \times 0.1$. The EM section is divided into 4 layers of 1.4, 2.0, 6.8, and 9.8 X_0 thickness. The third layer is further divided twice into cells covering 0.05×0.05 in the $\eta \times \phi$ plane. The CC-EM section has 32 modules in the ϕ direction. The detector responses are different for the particles that were incident on the modules as opposed to the intermodule crack (ϕ-crack). If an EM cluster position in ϕ at the third layer is > 0.02 from the crack, it is called ϕ-fiducial in CC region.

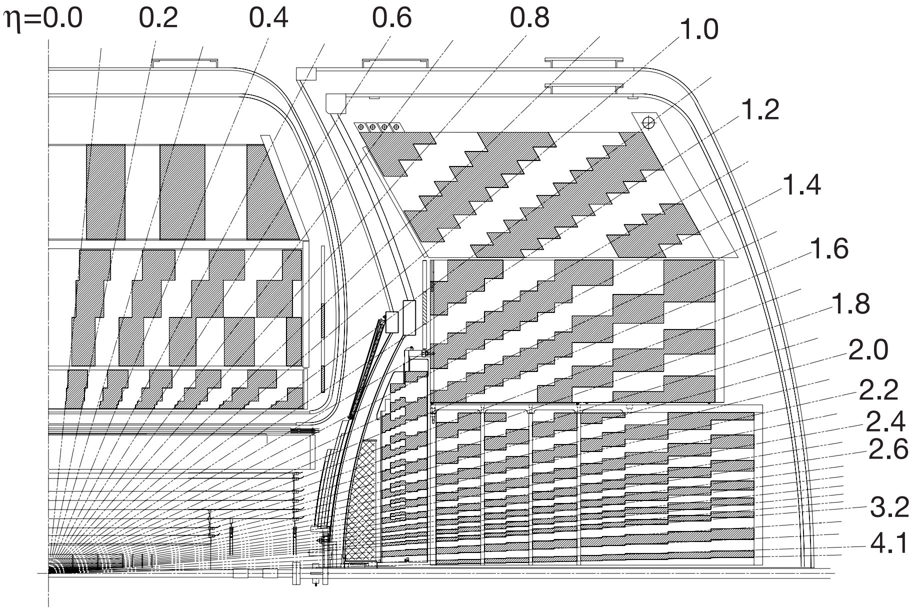

Figure 2.15: DØ Uranium/Liquid-argon Calorimeter showing segmentation in η and depth

2.2.6 Muon system

Muons would pass more easily through the detector than electrons, photons, or jets, and so the muons were detected at the outer-most layer of the DØ detector called the muon system. The upgraded DØ detector added a new forward muon system in addition to the original central muon system and toroidal magnet, extending muon detection from $|\eta| \leq 1.0$ to $|\eta| \approx 2.0$. The central muon system is comprised of proportional drift tubes (PDTs) in three layers (A, B and C). Layers A and B contain trigger scintillation counters providing coverage for $|\eta| < 1.0$. The new forward muon system used mini drift tubes (MDTs) instead of PDTs, and also trigger scintillation counters and beam pipe shielding. It extended the coverage for muon detection to $|\eta| \approx 2.0$. The toroidal iron magnet generated a 1.8 T magnetic field outside the calorimeter which provided a second measurement of the muon momentum besides the central tracker.

Figure 2.16 and 2.17 show a schematic view of the muon wire chambers and scintillation detectors. In the central muon system, a toroidal magnet generated 1.9 T magnetic field in the iron absorber. The PDTs of the A layer are located under the central toroidal magnet and so is the case for B layer, whereas the C layer is outside of the toroidal magnet. The PDTs measured the electron drift time and the charge deposition and thus helped in determining the hit position along the wire. They provided a drift distance resolution of about 1 mm. In the forward muon system, the end toroidal magnets produced approximately 2.0 T. The MDTs of the A layer are arranged inside toroidal magnets, and those for the B, and the C layer are located outside of the toroidal magnets . This was done in order to reconstruct muon tracks. The three layers of scintillation counters are also installed inside (layer A) and outside (layers B and C) of the toroidal magnet to trigger events which include a muon. The MDT coordinate has a resolution of $\sim$ 0.7 mm per hit. The stand-along momentum resolution is $\sim$ 20 % for muon momentum below 40 GeV/c. The MDT resolution on the bend angle, and the fact that we use multiple scatterings in the iron, helped us to refine our momentum resolution.

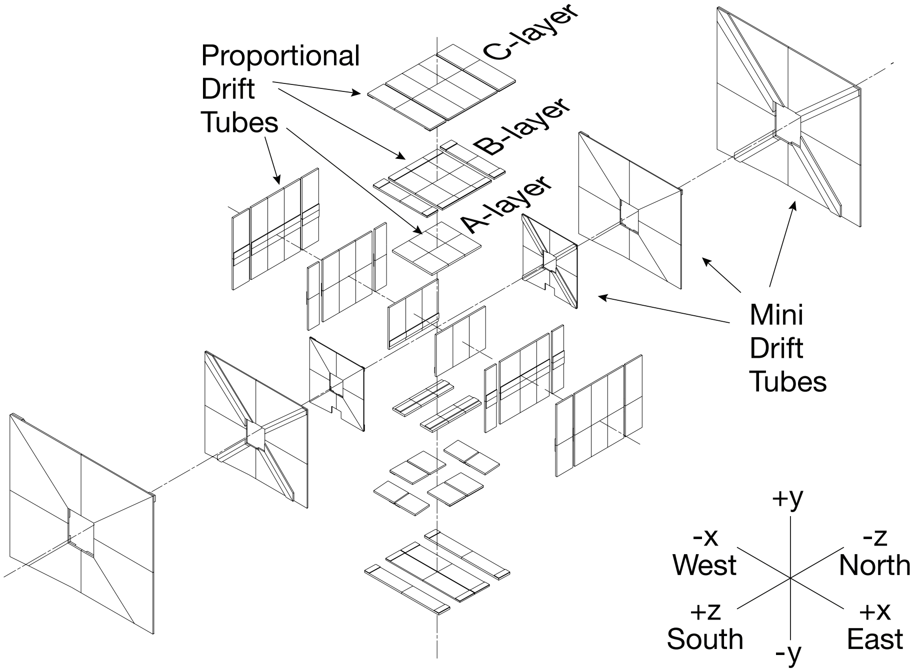

Figure 2.16: A schematic view of muon drift tube system of DØ

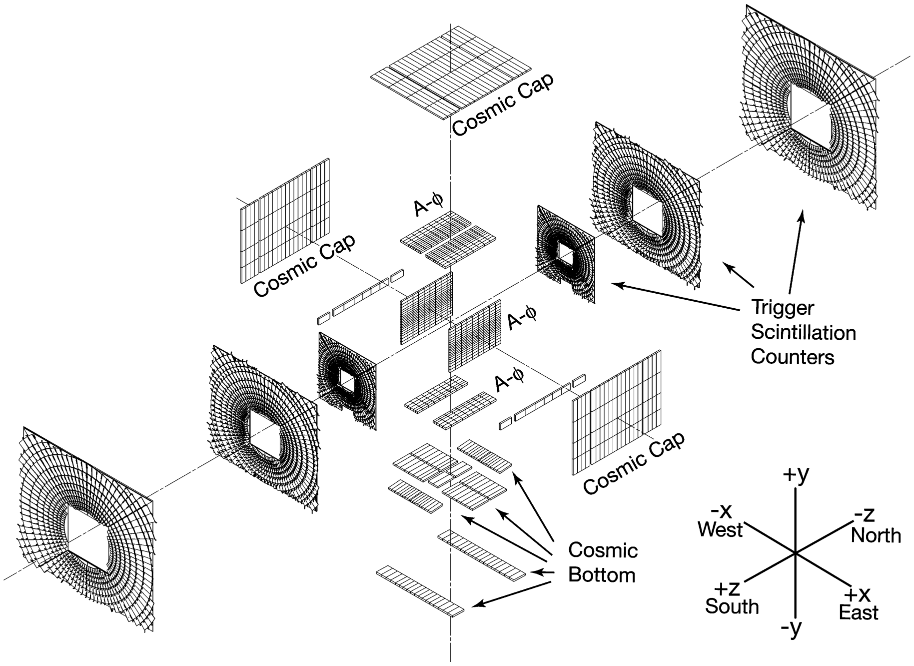

Figure 2.17: A schematic view of the muon scintillator system of DØ

2.2.7 Luminosity Monitor

The luminosity monitor (LM) determined the luminosity at the DØ interaction region by detecting inelastic $p\bar{p}$ collisions. It is installed in front of the end calorimeters at $z = \pm 140$ cm, covering $2.7 < |\eta| < 4.4$, as shown in Figure 2.18. The Figure. 2.19 shows the geometry of the LM counters and location of the PMTs.

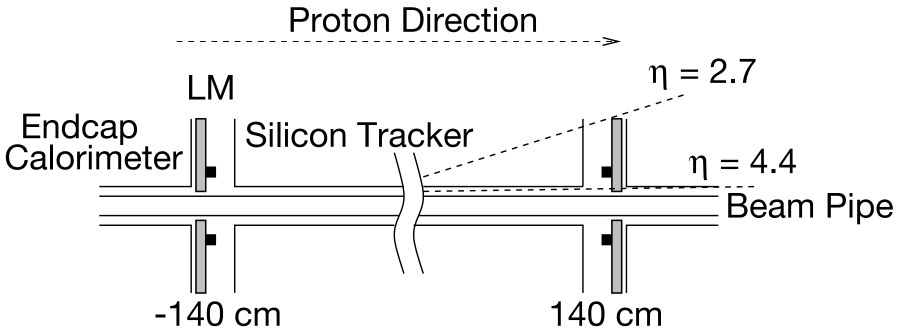

Figure 2.18: A schematic view of the location of the LM detectors

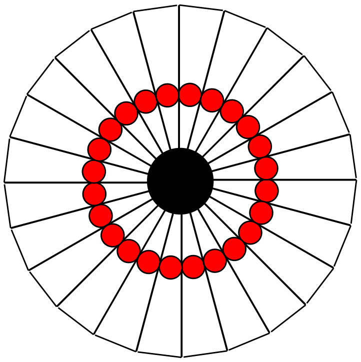

Figure 2.19: The geometry of the LM counters and location of the PMTs (solid red dots)

The luminosity L is calculated from the average number of inelastic collisions per beam crossing ($\bar{N}_{LM}$) measured by the LM:

$$L = \frac{f\bar{N}_{LM}}{\sigma_{LM}} \tag{2.4}$$

where f is the beam frequency and σ_{LM} is the effective cross section that includes the acceptance and efficiency of the LM detector [59]. It is important to remove beam halo backgrounds when counting $p\bar{p}$ interactions. It is done by constraining the z coordinate of the interaction vertex $|z_v|$ to be less than 100 cm. zv is calculated by Equation 2.5

$$zv = \frac{c}{2} \times (t_- - t_+) \tag{2.5}$$

where $t_\pm$ are the times of flight for particles hitting the LM placed at ±140 cm. Beam halo particles usually have $|zv| \approx 140$ cm, and therefore are usually eliminated by the requirement of $|zv| < 100$ cm.

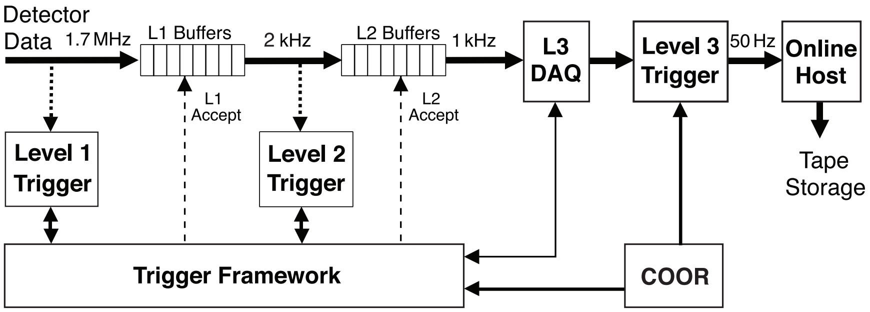

Figure 2.20: A schematic view of the trigger system of the DØ detector

2.2.8 Trigger System

The Tevatron accelerator system gave bunch crossings every 396 ns, which is 1/3962.5 MHz. It becomes unrealistic to record every single event because of dead time of the trigger system, our data recording rate and available disk space. The DØ detector has a trigger system with three distinct successive levels, called level 1 (L1) level 2 (L2) and level 3 (L3), to only select those interesting physics events to be recorded. Fewer events are examined with each succeeding level but in greater detail and more complexity. This is shown in Figure 2.20.

Level 1 The L1 trigger consists of the calorimeter trigger (L1Cal), the central track trigger (L1CTT) and the muon trigger (L1Muon). The L1Cal decision was made with the trigger inputs which searched for energy deposition patterns exceeding programmed limits on transverse energy deposits. The trigger tower energies were made up by sums of the energies deposited in $\delta\eta \times \delta\phi = 0.2 \times 0.2$. The L1CTT reconstructed the trajectories of charged particles using data taken by the CFT, and the CPS and FPS, to make trigger decision. The L1Muon trigger would find patterns made by muons using the signals from the muon wire chamber, the muon scintillation counters, and the tracks from the L1CTT. The Level 1 trigger decision was made within $3.5\mu s$. After L1 selection, the trigger rate is reduced to 2 kHz for L2.

Level 2 The second level, L2, would take data from the L1 trigger system in order to identify the types of particles found in the different subsections of the detector, and record properties such as the energy, direction, charge, and momentum of these objects. L2 would also compare data from across all subsections to determine if and how the particles were related to one another. The L2 trigger includes the L2CAL, L2CTT, L2MUO, L2PS (PreShower), L2STT and L2Global systems. The preprocessors of the L2 trigger system would reconstruct physics objects by collecting and analyzing data from the front-ends and from the L1 trigger system to make trigger decisions. The fired L1 triggers were sent to the L2Global system and the L2Global matched the fired L1 triggers to L2 triggers. This means that if a L1 trigger was matched to a related L2 trigger, the L2 trigger was passed. The L2 trigger system would further select events for L3 to process and decide. For L3 the trigger rate was reduced from 2 kHz to 1 kHz. Candidate events passing the L1 and L2 selection, would come to L3 for the decision whether or not to be recorded on tape.

Level 3 L3 is a fully programmable software trigger system and it decided on complete physics objects and their correlations. L3 also performed a limited reconstruction of events. The output rate of L3 was around 300 Hz limited by data recording speed, media costs and reconstruction capacities. The L3 trigger would receive candidates passing through the L1 and L2 triggers and it would reduce the 1 kHz input rate to 50 Hz so that events could be recorded for offline analysis. It performed a limited reconstruction of physics objects in events and reduced the input rate. Input, event building and output took 15 ms per event. Unpacking, reconstruction and filtering took about 235 ms. The L3DAQ system would transport detector component data from the VME readout crates to the L3 trigger filtering farm. The bandwidth of the L3DAQ was 250 MB/s and it corresponded to an average event size of about 200 kB at an L2 trigger accept rate of 1 kHz.

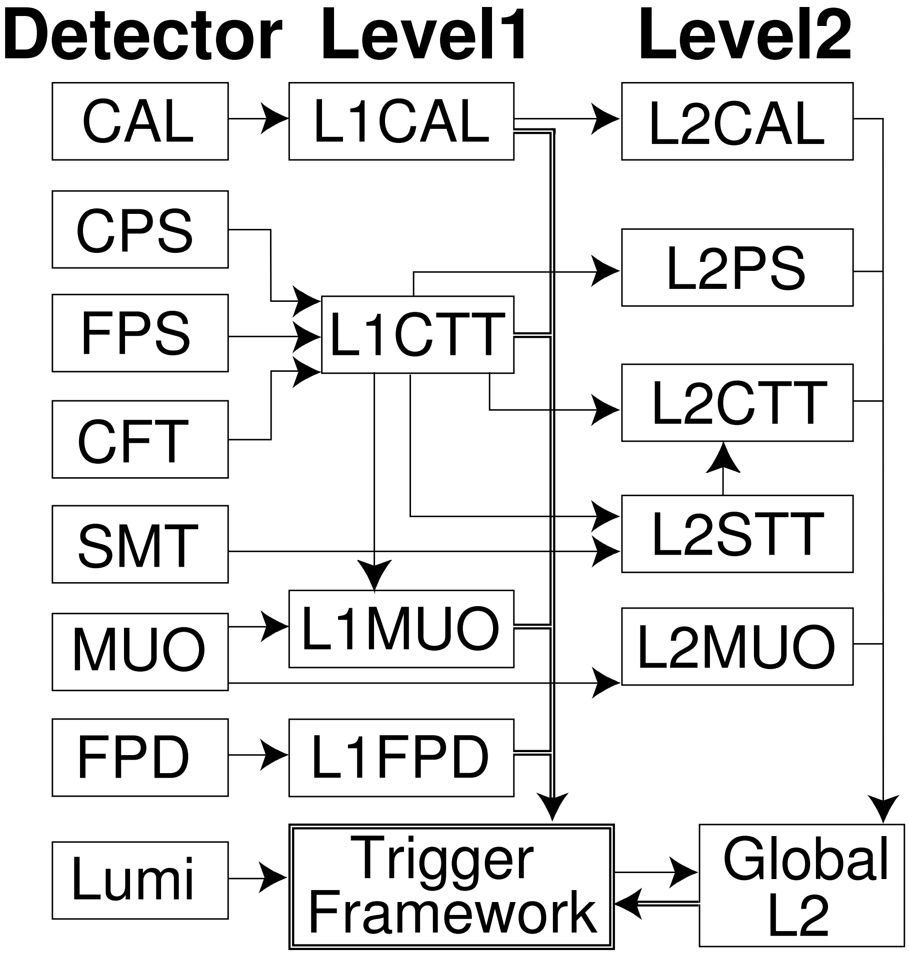

Figure 2.21: A flowchart representing how each sub-detector contributed to each of the three levels of the DØ trigger

Chapter 3

Data Sample and Monte Carlo Samples Used

In this chapter, the data samples and Monte Carlo (MC) samples used in for the present study are described.

3.1 $\gamma + b$-jet samples

3.1.1 Datasets

Data samples used for the work of this thesis are: DØ Run 2b data from Run 2b1, covering runs from 221698-234913, and corresponding to an integrated luminosity of about 1.2 fb^{-1}; from Run 2b2 – Run 2b3, covering runs from 237342–262856, and corresponding to an integrated luminosity of about 5.2 fb^{-1}; and from Run 2b4, covering runs from 264071–27016 corresponding to an integrated luminosity of about 1.2 fb^{-1}. To reduce the data size, the `EMInclusive` skim was used preselected by the Common Sample group according to the `'1 EMloose'` subskim definition satisfying the criteria where each event must contain at least one EM object found by Simple Cone EM clustering algorithm [60] with

- $|\mathrm{ID}| = 10, 11$
- $p_T \geq 20$ GeV.

Runs in the data sample are required to pass data quality selections provided with `dq_defs` package of version v2011-03-18. The datasets have been selected using a logical OR combination of the unprescaled EM triggers of versions 15–16 with calorimeter-based only requirements:

```
v15:
E1_SHT25 E1_SH35 E1_L70
E2_SHT25 E2_SH35 E2_L70
E1_ISHT22 E1_ISH30
E2_ISHT22 E2_ISH30

v155:
E1_SHT25 E1_LH2SH27 E1_LH2L70 E1_SHT50 E1_SH60 E1_L80
E2_SHT25 E2_LH2SH27 E1_LH2L70 E2_SHT50 E2_SH60 E2_L80
E1_LH2ISH24 E2_LH2ISH24

v16:
E1_SHT25 E1_LH2SH27 E1_SHT27 E1_LH3SH27 E1_LH2L70 E1_SHT50 E1_SH60
E1_L80 E1_SHT27_NOLUM
E2_SHT25 E2_LH2SH27 E2_SHT27 E2_LH3SH27 E2_LH2L70 E2_SHT50 E1_SH60 E2_L80
E1_LH2ISH24 E1_LH3ISH25
E2_LH2ISH24 E2_LH3ISH25
```

After applying all the quality criteria and trigger conditions described above, the integrated luminosity of the dataset is found to be 7.63 ± 0.46 fb^{-1} (0.60 fb^{-1} in v15, 1.18 fb^{-1} in v155 and 5.85 fb^{-1} in v16).

3.1.2 Monte Carlo Samples

Monte Carlo samples of signal and background processes are generated using PYTHIA v6.4 with CTEQ6L1 parton distribution functions and are passed through a GEANT-3 [61] based simulation of the DØ detector. The same algorithms as for data are used to reconstruct the events.The inclusive $\gamma +$ jets processes include $qg \to q\gamma$, $q\bar{q} \to g\gamma$, and $gg \to g\gamma$ parton scatterings. The $\gamma + b$ and $\gamma + c$ events are obtained by generating inclusive $\gamma +$ jets events as above, and then passing them at the generator level through a `d0_mess` [62] filter that requires at least one b (c) quark in the event. In order to cover a large range with sufficient event statistics even at large values of p_T^γ, the events are generated in several bins of parton $\hat{p}_T$.

The dijet background events are filtered at the generator level for the EM-like jets by imposing the cuts described in [63]. The events are also generated in several $\hat{p}_T$ bins. Tables 3.1–3.5 give an overview of the signal and background Monte Carlo samples used in this analysis.

Process	$\hat{p}_T$(GeV)	Event ID	# events	MC version
$\gamma +$ jets	20–40	86116, 86117	500 k	p21.11.00
	40–80	86118, 86119	500 k	p21.11.00
	80–160	86120, 86121	500 k	p21.11.00
	160–320	86122, 86123	500 k	p21.11.00
$\gamma + b$	20–40	137712	200 k	p21.11.00
	40–980	107172, 107176	1000 k	p21.11.00
	80–980	107177, 107178	400 k	p21.11.00
	160–980	107179	200 k	p21.11.00
$\gamma + c$	20–40	137713	200 k	p21.11.00
		146112,146113,146114	600 k	p21.11.00
	40–980	106852, 106856	1000 k	p21.11.00
		146115,146116,146117	600 k	p21.11.00
	80–980	106857, 106858	400 k	p21.11.00
		146118,146119,146120	600 k	p21.11.00
	160–980	106859	200 k	p21.11.00
		146121,146122,146123	600 k	p21.11.00

Table 3.1: Run2b1: PYTHIA Signal Monte Carlo samples.

Process	$\hat{p}_T$(GeV)	Event ID	# events	MC version
$\gamma+$jets	25–300 (with MPI)	146492, 146551	3000 k	p21.11.00

Table 3.2: Run2b1: SHERPA Monte Carlo samples.

Process	$\hat{p}_T$(GeV)	Event ID	# events	MC version
$\gamma+$jets	20–40	125996, 125997	500 k	p21.18.00
	40–80	125998, 125999	500 k	p21.18.00
	80–160	126000, 126001	500 k	p21.18.00
	160–320	126002, 126003	500 k	p21.18.00
$\gamma+b$	20–40	137714	200 k	p21.18.00
	40–80	137716	200 k	p21.18.00
	80–160	137718	200 k	p21.18.00
	160–980	137720	200 k	p21.18.00
$\gamma+c$	20–40	137715	200 k	p21.18.00
		146133,146134,146135	600 k	p21.18.00
	40–80	137717	200 k	p21.18.00
		146124,146125,146126	600 k	p21.18.00
	80–160	137719	200 k	p21.18.00
		146127,146128,146129	600 k	p21.18.00
	160–980	137721	200 k	p21.18.00
		146130,146131,146132	600 k	p21.11.00

Table 3.3: Run2b2: Signal Monte Carlo samples.

Process	$\hat{p}_T$(GeV)	Event ID	# events	MC version
$\gamma+$jets	20–40	154596, 154597	600 k	p21.21.00
	40–80	154598, 154599	600 k	p21.21.00
	80–160	154600, 154601	600 k	p21.21.00
	160–320	154602, 154603	600 k	p21.21.00

Table 3.4: Run2b3: Signal Monte Carlo samples.

Process	$\hat{p}_T$(GeV)	Event ID	# events	MC version
Z+jet	$15 < m_{ee} < 60$	86887–86902	1,840 k	p21.11.00
($Z \to ee$)	$60 < m_{ee} < 130$	86882–86886, 86893–86897		
		94342–94351	3.730M	p21.11.00
	$130 < m_{ee} < 250$	86892,94192–94194	0.55M	p21.11.00
W+jet				
($W \to e\nu$)	107962–108581		12.7M	p21.11.00

Table 3.5: Run2b1: PYTHIA background Monte Carlo samples.

3.2 $Z+$ jets samples

3.2.1 Datasets

The data sample for this analysis was collected from Fermilab Tevatron $p\bar{p}$ collisions at center-of-mass energy $\sqrt{s}$ = 1.96 TeV using the D0 detector. The data was selected from the 2MUhighpt and 2EMhighpt Common Samples Group skims listed in Table 3.6. This covered Run2a, Run2b1, Run2b2, Run2b3 and Run2b4 which accounted for total integrated luminosity 9.7 fb^{-1}.

Run IIa Data Samples
CSG_CAF_<SKIM>_PASS3_p18.14.00
Run IIb1 Data Samples
CSG_CAF_<SKIM>_PASS2_p21.10.00
Run IIb2 Data Samples
CSG_CAF_<SKIM>_PASS4_p21.10.00 CSG_CAF_<SKIM>_PASS4_p21.10.01 CSG_CAF_<SKIM>_PASS4_p21.10.02 CSG_CAF_<SKIM>_PASS4_p21.10.04 CSG_CAF_<SKIM>_PASS4_p21.10.00_p20.12.05_allfix
Run IIb3 Data Samples
CSG_CAF_<SKIM>_PASS5_p21.16.07_fix CSG_CAF_<SKIM>_PASS5_p21.16.07_reduced2 CSG_CAF_<SKIM>_PASS5_p21.16.08
Run IIb4 Data Samples
CSG_CAF_<SKIM>_PASS6_p21.20.00_p20.18.02b CSG_CAF_<SKIM>_PASS6_p21.20.00_p20.18.02b_fix CSG_CAF_<SKIM>_PASS6_p21.20.00_p20.18.03 CSG_CAF_<SKIM>_PASS6_p21.20.00_p20.18.04 CSG_CAF_<SKIM>_PASS6_p21.20.00_p20.18.05

Table 3.6: $Z+$jets samples

Events containing Z bosons decaying to dielectron (ee) and dimuon ($\mu\mu$) are used for present work. For the ee final state, an "OR" of the single electron triggers was used, with an efficiency of close to 100%. For the $\mu\mu$ final state, an "OR" of the single muon triggers was used, with an efficiency of 78%. The treatment of systematic uncertainty of the muon trigger is discussed in Section 6.4. The data was filtered by the CafeDataQualityProcessor [64] using standard data quality definition *dq_defs/2009-06-13* which removes bad runs and luminosity blocks as defined by the SMT, CFT, Calorimeter, and Muon groups. The integrated luminosity of the data sample *after the data quality selection* was measured using the standard luminosity tools (dq_util/util/lumitool.py) [64], and found to be 9.7 fb^{-1} for Run IIb. In addition, a cut was applied removing events that contained bad event quality flags from both data and Monte Carlo.

3.2.2 MC Samples

The present work makes use of several Monte Carlo (MC) samples for the Z+jets events selection and the estimation of background contributions. With the exception of the multijet background, all significant background processes are estimated from MC simulation: $t\bar{t}$, WZ, WW, and ZZ. The details of these MC samples are outlined in this section.

The MC samples used here were generated with the p20.09.03 release. The certified CAF trees of the Common Samples Group [65] produced with the release p21.11.00 were used, which are listed in Tables 3.7–3.9 in this section. The Z+jets MC samples are given in different bins of dilepton invariant mass. Also the cross-section, MC event IDs and total number of events for each MC sample are listed in the table. The WW, WZ and ZZ processes were generated using Pythia, while the $t\bar{t}$ and Z+jets processes were generated with Alpgen [66] interfaced with Pythia. The $Z +$ jets MC samples were generated with Alpgen separately for each number of additional partons. The initial and final state parton radiation was then added to the event using Pythia, applying a matching scheme [67] to avoid double counting. To simulate the underlying event, the so-called "DØ-Tune" (Tune A with CTEQ6L1 PDF) was used.

The Z+jets MC samples consist events with only light partons, called Z+LP, and events with heavy-flavour partons, called Z+HF. Samples were generated specifically for $Z + 2b(2c)$ jets with additional light parton jets. Some of these samples overlap in the final state phase space with the events which were generated for $Z +$

light partons (nlp). In order to avoid double counting the overlapping events, events with b or c quark jets in the final state from the $Z + nlp$ sample and events with c quark jets in the final state from the $Z + 2b + nlp$ samples [68] were removed. The cross-sections for these HF skimmed samples were then scaled to reflect the removal of those events.

The generated background and signal samples were processed with the standard DØ simulation chain which includes a full GEANT 3 detector simulation. Zero-bias events taken from data are overlayed onto the MC events to reproduce the beam conditions during actual data collection. The events were reconstructed using the DØ data reconstruction program, d0reco, in the DØ release versions p17.09.00, p17.09.06 (Run 2a) and p20.08.02, p20.09.02, p20.09.03 (Run 2b), respectively. The reconstructed events were converted into CAF trees using the DØ analysis package tmb_analyze in the release versions p18.14.00 (Run 2a) and p21.11.00 (Run 2b), respectively. During the processing of the MC events, duplicated events and events for which the zero-bias overlay does not pass data quality criteria were removed.

Sample cross-sections were taken from several different sources depending on whether the samples were produced using Pythia or ALPGEN + Pythia. The WZ, WW, and ZZ cross-sections are taken from MCF [69] as these samples were generated using Pythia exclusively. These cross-sections are NLO, and use CTEQ6.1M PDF's. Additional NLO corrections were applied to the ALPGEN Z+jets cross-sections and are described next.

Process	Mass Range (GeV)	$\sigma\times$ BR (pb)	MC Event ID	Generator	# Events
$Z/\gamma^* + 0lp \to \mu\mu$	$15 < M(Z) < 75$	338.363	70293, 90692, 90694, 90696, 93640 93641, 93642, 93643, 93644, 93645, 93646	ALPGEN + PYTHIA	1805548
$Z/\gamma^* + 0lp \to \mu\mu$	$75 < M(Z) < 130$	133.103	66676, 67492, 74177, 74178, 74179 74180, 93654, 93655, 93656	ALPGEN + PYTHIA	1036678
$Z/\gamma^* + 0lp \to \mu\mu$	$130 < M(Z) < 250$	1.335	89672, 89673	ALPGEN + PYTHIA	271249
$Z/\gamma^* + 0lp \to \mu\mu$	$M(Z) > 250$	0.072	87913, 91359, 91360	ALPGEN + PYTHIA	541752
$Z/\gamma^* + 1lp \to \mu\mu$	$15 < M(Z) < 75$	39.942	70294, 86940, 86941, 90698	ALPGEN + PYTHIA	336634
$Z/\gamma^* + 1lp \to \mu\mu$	$75 < M(Z) < 130$	40.677	66677, 67512, 74181, 74182	ALPGEN + PYTHIA	616917
$Z/\gamma^* + 1lp \to \mu\mu$	$130 < M(Z) < 250$	0.931	89674	ALPGEN + PYTHIA	173777
$Z/\gamma^* + 1lp \to \mu\mu$	$M(Z) > 250$	0.036	87914, 91365, 91366	ALPGEN + PYTHIA	450281
$Z/\gamma^* + 2lp \to \mu\mu$	$15 < M(Z) < 75$	9.870	70297, 86947, 90700	ALPGEN + PYTHIA	197528
$Z/\gamma^* + 2lp \to \mu\mu$	$75 < M(Z) < 130$	9.7514	66678, 68072, 74183	ALPGEN + PYTHIA	432267
$Z/\gamma^* + 2lp \to \mu\mu$	$130 < M(Z) < 250$	0.480	89675	ALPGEN + PYTHIA	173118
$Z/\gamma^* + 2lp \to \mu\mu$	$M(Z) > 250$	0.011	87915, 91370	ALPGEN + PYTHIA	354830
$Z/\gamma^* + 3lp \to \mu\mu$	$15 < M(Z) < 75$	2.739	70298, 90702, 91232	ALPGEN + PYTHIA	317512
$Z/\gamma^* + 3lp \to \mu\mu$	$75 < M(Z) < 130$	3.1148	66679, 68132, 74184	ALPGEN + PYTHIA	166902
$Z/\gamma^* + 3lp \to \mu\mu$	$130 < M(Z) < 250$	0.053	89676	ALPGEN + PYTHIA	164316
$Z/\gamma^* + 3lp \to \mu\mu$	$M(Z) > 250$	0.0066	70298, 90702, 91232	ALPGEN + PYTHIA	354415
$Z/\gamma^* + 2b + 0lp \to \mu\mu$	$15 < M(Z) < 75$	0.5087	89378	ALPGEN + PYTHIA	188546
$Z/\gamma^* + 2b + 0lp \to \mu\mu$	$75 < M(Z) < 130$	0.4175	68979	ALPGEN + PYTHIA	179558
$Z/\gamma^* + 2b + 0lp \to \mu\mu$	$130 < M(Z) < 250$	0.0034	86577	ALPGEN + PYTHIA	90624
$Z/\gamma^* + 2b + 0lp \to \mu\mu$	$M(Z) > 250$	0.00034	88011	ALPGEN + PYTHIA	178546
$Z/\gamma^* + 2b + 1lp \to \mu\mu$	$15 < M(Z) < 75$	0.1988	89379	ALPGEN + PYTHIA	92018
$Z/\gamma^* + 2b + 1lp \to \mu\mu$	$75 < M(Z) < 130$	0.1904	68982	ALPGEN + PYTHIA	96941
$Z/\gamma^* + 2b + 1lp \to \mu\mu$	$130 < M(Z) < 250$	0.0018	89381	ALPGEN + PYTHIA	46222
$Z/\gamma^* + 2b + 1lp \to \mu\mu$	$M(Z) > 250$	0.00018	88012	ALPGEN + PYTHIA	180821
$Z/\gamma^* + 2b + 2lp \to \mu\mu$	$15 < M(Z) < 75$	0.01835	89380	ALPGEN + PYTHIA	89922
$Z/\gamma^* + 2b + 2lp \to \mu\mu$	$75 < M(Z) < 130$	0.09859	68985	ALPGEN + PYTHIA	47925
$Z/\gamma^* + 2b + 2lp \to \mu\mu$	$130 < M(Z) < 250$	0.00088	89382	ALPGEN + PYTHIA	45903
$Z/\gamma^* + 2b + 2lp \to \mu\mu$	$M(Z) > 250$	0.0001	88013	ALPGEN + PYTHIA	187820
$Z/\gamma^* + 2c + 0lp \to \mu\mu$	$15 < M(Z) < 75$	4.144	86952	ALPGEN + PYTHIA	180580
$Z/\gamma^* + 2c + 0lp \to \mu\mu$	$75 < M(Z) < 130$	0.9322	71095	ALPGEN + PYTHIA	187636
$Z/\gamma^* + 2c + 0lp \to \mu\mu$	$130 < M(Z) < 250$	0.0076	86580	ALPGEN + PYTHIA	79493
$Z/\gamma^* + 2c + 0lp \to \mu\mu$	$M(Z) > 250$	0.00062	87932	ALPGEN + PYTHIA	191017
$Z/\gamma^* + 2c + 1lp \to \mu\mu$	$15 < M(Z) < 75$	0.9530	89413	ALPGEN + PYTHIA	93093
$Z/\gamma^* + 2c + 1lp \to \mu\mu$	$75 < M(Z) < 130$	0.5481	71095	ALPGEN + PYTHIA	187636
$Z/\gamma^* + 2c + 1lp \to \mu\mu$	$130 < M(Z) < 250$	0.00439	91576	ALPGEN + PYTHIA	45857
$Z/\gamma^* + 2c + 1lp \to \mu\mu$	$M(Z) > 250$	0.00044	87933	ALPGEN + PYTHIA	170822
$Z/\gamma^* + 2c + 2lp \to \mu\mu$	$15 < M(Z) < 75$	0.3431	89412	ALPGEN + PYTHIA	95436
$Z/\gamma^* + 2c + 2lp \to \mu\mu$	$75 < M(Z) < 130$	0.0985	71097	ALPGEN + PYTHIA	49608
$Z/\gamma^* + 2c + 2lp \to \mu\mu$	$130 < M(Z) < 250$	0.00283	89415	ALPGEN + PYTHIA	47946
$Z/\gamma^* + 2c + 2lp \to \mu\mu$	$M(Z) > 250$	0.00026	87934	ALPGEN + PYTHIA	181158
$ZZ \to 2j2\ell$		0.226	88817	PYTHIA	105325
$WZ \to 2j2\ell$		0.275	88818, 88819	PYTHIA	273344
$WW \to incl$		12.35	86772, 86773, 86779, 86780	PYTHIA	675814
$tt \to 2b2\ell2\nu + 0lp$		0.33	87299, 87300, 87301, 87302	ALPGEN+PYTHIA	749642
$tt \to 2b2\ell2\nu + 1lp$		0.14	87313, 87314, 87315	ALPGEN+PYTHIA	452177
$tt \to 2b2\ell2\nu + 2lp$		0.07	87322, 87323	ALPGEN+PYTHIA	281453

Table 3.7: The p20 MC samples used, and their cross-sections (before any scaling corrections), SAM request ID's and number of events generated after removing events failing DQ cuts. Here ℓ stands for any of the charged leptons: e or μ. “lp” stands for ”light-parton” in ALPGEN, and indicates the number of hard jets at the parton level for each ALPGEN+Pythia sub-sample. “excl.” means that the sub-sample is exclusive and requires exactly the number of light partons indicated, whereas “incl.” denotes that all higher parton multiplicity states were also allowed.

sample	cross-section(xBR)	MC Event ID	# Events
$t\bar{t}(\rightarrow \ell^+\ell^-) + 0$lp excl.	0.352 pb	87299,87300/1/2	750k
$t\bar{t}(\rightarrow \ell^+\ell^-) + 1$lp excl.	0.142 pb	87313/4/5	450k
$t\bar{t}(\rightarrow \ell^+\ell^-) + 2$lp incl.	0.068 pb	87322/3	280k
WW incl.	11.6 pb	86772/3/9,86780	710k
WZ incl.	3.25 pb	86774/5/6/7	630k
ZZ incl.	1.33 pb	86778,86787/8	540k

Table 3.8: The p20 MC samples used, and their cross-sections (before any scaling corrections), SAM request ID's or dataset definition names, and number of events generated after removing events failing DQ cuts.

sample	cross-section (xBR)	MC Event ID	# Events
Z+0lp excl. (M_Z=15-75 GeV)	337 pb	702723,87252/3/4,91538 91540/2,93635/8/9	1580k
Z+0lp excl. (M_Z=75-130 GeV)	132 pb	67713,72772/3 93632,93634	1010k
Z+0lp excl. (M_Z=130-250 GeV)	0.891 pb	87262/3	350k
Z+1lp excl. (M_Z=15-75 GeV)	40.0 pb	70274,87255/6/7 91539,91541/3	1580k
Z+1lp excl. (M_Z=75-130 GeV)	40.1 pb	67714,72792/3	570k
Z+1lp excl. (M_Z=130-250 GeV)	0.376 pb	87264	180k
Z+2lp excl. (M_Z=15-75 GeV)	9.95 pb	70275,87258/9,91544/6	550k
Z+2lp excl. (M_Z=75-130 GeV)	9.98 pb	67715,72812	270k
Z+2lp excl. (M_Z=130-250 GeV)	102 fb	87265	160k
Z+3lp incl. (M_Z=15-75 GeV)	2.77 pb	70276,87260/1,91545/7	540k
Z+3lp incl. (M_Z=75-130 GeV)	3.30 pb	67716,72832	130k
Z+3lp incl. (M_Z=130-250 GeV)	33.1 fb	87266,91112	300k
Z+2b+0lp excl. (M_Z=15-75 GeV)	0.518 pb	89372	170k
Z+2b+0lp excl. (M_Z=75-130 GeV)	0.401 pb	68978	200k
Z+2b+0lp excl. (M_Z=130-250 GeV)	3.40 fb	86575	90k
Z+2b+1lp excl. (M_Z=15-75 GeV)	0.207 pb	89375	85k
Z+2b+1lp excl. (M_Z=75-130 GeV)	0.173 pb	68981	93k
Z+2b+1lp excl. (M_Z=130-250 GeV)	1.67 fb	89376	45k
Z+2b+2lp incl. (M_Z=15-75 GeV)	78.3 fb	89374	82k
Z+2b+2lp incl. (M_Z=75-130 GeV)	107 fb	68984	44k
Z+2b+2lp incl. (M_Z=130-250 GeV)	0.938 fb	89377	44k
Z+2c+0lp excl. (M_Z=15-75 GeV)	4.09 pb	86951	180k
Z+2c+0lp excl. (M_Z=75-130 GeV)	0.901 pb	87892	180k
Z+2c+0lp excl. (M_Z=130-250 GeV)	7.50 fb	86578,87893	180k
Z+2c+1lp excl. (M_Z=15-75 GeV)	1.03 pb	87895,91548	180k
Z+2c+1lp excl. (M_Z=75-130 GeV)	0.506 pb	71093	90k
Z+2c+1lp excl. (M_Z=130-250 GeV)	4.33 fb	87896,91575	90k
Z+2c+2lp incl. (M_Z=15-75 GeV)	0.382 pb	87898,91549	170k
Z+2c+2lp incl. (M_Z=75-130 GeV)	0.286 pb	87899	50k
Z+2c+2lp incl. (M_Z=130-250 GeV)	2.67 fb	87900,91577	90k

Table 3.9: The p20 MC samples used, and their cross-sections (before any scaling corrections), SAM request ID's or dataset definition names, and number of events generated after removing events failing DQ cuts.

Chapter 4

Event Reconstruction

After passing all levels of the trigger system, the data from an event is stored so that it can be used for data analysis. In order to have useful information, the data must be transformed from detector hits and energy deposits into physics objects. DØ has developed various reconstruction algorithms that reconstruct the energy and paths of particles as they move in the detector, interact, and decay. This chapter describes the methods and algorithms relating to the reconstruction of each particle's tracks, primary interaction vertices, photons, jets, and missing energy used in this analysis.

4.1 Track reconstruction

Particle paths are reconstructed as tracks in DØ tracking volume. As the charged particles move through the SMT and CFT, their paths are curved by the magnetic field of the solenoid magnet. These particles would deposit small amounts of energy within the layers of the tracking material. Each of these energy deposits is called a hit. So at their most basic level, particle tracks are reconstructed from a collection of hits from a single particle. We reconstruct track of each particle from the collection of its hits using the DØ tracking algorithms. The tracking algorithm first takes hit information from the SMT and from it forms a pool of track hypotheses. The initial track hypothesis requires its first hit to be either from one of the barrels or from an F disk. The second hit must be in a layer farther from the beam pipe than the first one. They should be close in ϕ such that $\Delta\phi(1,2) < 0.08$. The third hit must be located in a layer farther from the beam than both the first and second hits. The radius of the circle in the transverse plane fitted to the hits must be more than 30 cm corresponding to the track p_T of 180 MeV. At each layer a χ^2 of hits with respect to the track is calculated and the hit becomes associated with the track if it is χ^2 is less than a certain value. If there is no hit in the layer, the algorithm continues and records a "miss" for this track. At the end of this procedure, a list of tracks is produced along with hits, "misses", and $\chi^2 - s$. If the number of hits is less than 3 in the SMT, then this algorithm finds "CFT only" tracks.

4.2 Primary Vertex reconstruction

Primary vertex is the point in space at which the hard scattering proton and antiproton collision occurs. Due to the fact that there are multiple proton and antiproton interactions in any given event, we reconstruct the primary interaction vertex from the track information. It is important to be certain that the reconstructed vertex corresponds to the hard scattering process that triggered the event.

The location of the PV is reconstructed using the adaptive primary vertex algorithm [70]. This algorithm consists of three steps: track selection, vertex fitting and vertex selection.

Track Selection requires tracks to have:

- $p_T > 0.5$ GeV
- two or more hits registered in the SMT and assign the tracks to a vertex to which the extrapolated paths of the tracks point.

This process removes poorly measured and fake tracks. We shift through all hits in the SMT using this method to create an initial list of primary vertex candidates. χ^2 of fit based on the impact parameter of associated track is minimized in order to determine the position of each vertex. The impact parameter IP is the minimum distance from a track to the primary vertex. Thus tracks that originated from that vertex will have a smaller IP.

After establishing a preliminary list of primary vertices, the beam spot information is considered to determine the distance of closest approach (dca) of tracks. In this step, tracks which are not associated to any primary vertex candidate go through a much more restrictive selection of $dca/\sigma_{dca} < 3$. Tracks subjected to this additional requirement are re-fitted to each of the primary vertices.

Thus the two-pass method gives more tracks on average for a given vertex than the single-pass technique. This is beneficial because more the tracks with a high transverse momentum associated with a primary vertex, the higher is our confidence for choosing the correct primary vertex.

To determine the primary interaction vertex associated with the hard scattering process a selection technique is used. It should be noted that tracks coming from soft scattering processes and minimum bias events have smaller values of p_T than those coming from hard scattering process. To determine the probability of a track coming from one of these events, a distribution in $\log_{10} p_T$ of these minimum bias process is used. A probability is assigned for each track of $p_T > 0.5$ GeV. The product of these individual track probabilities is the probability of vertex:

$$\Pi_i P^i_{tracks} = P_{PVz} \tag{4.1}$$

This is then weighted so that it is independent of the track multiplicity of vertex.

4.3 EM object reconstruction

Electrons and photons would deposit a large majority of their energy within the first four layers of the DØ calorimeter. Mostly these particle showers would consist of photons converting into electron-positron pairs and in turn these particles would produce photons through Bremsstrauhlung. The transverse width of showers is small compared to that of the jets containing hadrons.

The energies of the cells of calorimeter and their resulting towers are used to reconstruct the energy of an EM object. There are two algorithms for the treatment of calorimeter towers for reconstructing EM objects. The first one is the SimpleCone algorithm [60] and the second one is called cellNN. Although this second algorithm has valuable techniques for reconstructing EM objects at low photon momentum ($E_T^\gamma < 10$ GeV), it was not used in this analysis.

The SCone algorithm is discussed briefly below as it is used for EM object energy reconstruction and the technique it uses is very similar to the one used to determine jet energy deposition in the calorimeter.

4.3.1 The SCone algorithm

In SCone algorithm, a list of energetic towers, ordered in decreasing E_T are taken and looped over each of them. A tower is removed from the list of the towers if its energy exceeds 500 MeV. These high-energy towers are then used as seed towers. A circle of radius 0.4 in η-ϕ is made about the position of each seed tower and the towers energy is taken to be the initial energy of the cluster. The remaining energetic towers are looped over to find more towers within the circle. Similarly we can make these circles at all of the layers. As the layers farther away from the beam pipe are larger due to increased radial distance, these circles differ in size. We can combine them to form a cone about the energetic tower.

If additional towers are found within this cone, then the energy of these towers is added to the total energy of the cluster. The energy-weighted position of this larger energy cluster is recalculated. This process is repeated until it exhausts the list of all towers, producing a total energy and position of this energy cluster of the EM object. The EM object energy cluster has to meet quality criteria:

- it must be formed of at least two towers and
- it must have energy exceeding 1 GeV.

This suppresses noise and low energy clusters. After meeting these requirements, the cluster is selected for the list of EM objects.

After finishing the first round of EM clustering, the list of recently calculated EM objects must meet additional criteria. First, its energy is recomputed for a cone of 0.2 ($R = 0.2$) and this new energy should be at least 1.5 GeV. The fraction of the cluster's energy that comes from the EM portion must be greater than 90%. The EM cluster must also be well isolated within the detector. Isolation is defined as:

$$iso = \frac{E_{total}(R < 0.4) - E_{EM}(R < 0.2)}{E_{EM}(R < 0.2)} \tag{4.2}$$

where $E_{total}(R < 0.4)$ is the total energy deposited in the calorimeter in a cone of radius R = 0.4 and $E_{EM}(R < 0.2)$ is the energy deposited in the EM portion of the calorimeter in a cone of radius R = 0.2. Iso tells how well isolated an EM object is within a calorimeter. A small isolation ($iso < 0.2$) means that no other particles travelled through the detector near the EM object. A larger value corresponds to a case if one or more particles were to pass through the detector within radius $R < 0.4$.

4.3.2 Electromagnetic Energy Scale

The energy scale for photons and electrons is calculated using the Z boson. The invariant mass peak of the Z boson is known to high precision and the absolute peak can be matched by using electrons and positrons from $Z \rightarrow e^- e^+$. The energy contributions coming from each layer are chosen as the ones that minimize the width of the Z peak. It is interesting to compare the measurements of the layer weights from Run II and Run I at DØ. Since in Run I there was less material before the calorimeter, the EM showers deposited a maximum energy at the third EM layer. This also explains the interesting segmentation choice of the EM layers in the calorimeter as they were chosen to improve the resolution for where the maximum sensitivity was needed. During the upgrade for Run II, a silicon system, fiber tracker, solenoid and layer of lead were installed in front of the calorimeter. As a result of these changes, the maximum shower layer moved closer to the first EM layer.

Due to a small difference between energy of the photon and the electron response, there is an additional correction applied to energy of the photon. The details of this study are given in DØ Note [71]. It shows that before the correction was applied the EM energy scale systematically overestimated the energy of photons. The correction for photons varies from 2.0% for p_T^γ 30 GeV to 1.0% for p_T^γ 150 GeV, with a corresponding uncertainty coming from this correction between $0.5 - 0.9\%$ depending on p_T^γ.

4.3.3 EM Object Identification Algorithms

A number of event topologies exist which contain objects whose signature resembles with that of photon. These topologies are known as background which mimic the signal and need to be minimized as much as possible. The dominant background for electron and photon production is from dijet events, where one jet deposits a large fraction of its energy in the EM layers of the calorimeter. We refer to such events as fake photons. This can occur if the jet contains a neutral pion (π^0), for example, that carries most of the momentum associated with the jet. π^0 decays to two photons more than 98% of the time [60]. Due to more energy and low mass (134.79 MeV $/c^2$) of π^0, the opening angle between two photons is very small and the two photons appear as one in the detector. Although the total fraction of dijet events is small, the cross section for dijet production is significantly larger than that of the final states containing photons and electrons. This results in a large number of fake photon candidates, and sophisticated algorithms have been built to distinguish these objects. The two important variables in EM object identification have been already discussed in Section 4.3.1, the isolation and EM fraction requirements.

In addition to these requirements there are two widely used discriminants for photon selection at DØ. The first is based on the transverse shower width in the third calorimeter EM layer and is calculated as follows:

$$\sigma_{r\phi} = \sum_{i=0}^{Ncells} \frac{E_i \times R_{Cal}^2 \times \sin^2(\phi_c - \phi_i)}{E_c} \tag{4.3}$$

where R_{Cal} is the radial distance from the beam pipe to the third calorimeter EM layer, E_i is the calorimeter cell energy, E_c is the cluster energy, ϕ_i is the ϕ position of cell and ϕ_c is the position of EM cluster. The second discriminant uses the fact that photons do not leave tracks in the tracking volume of detector, but the background jets have multiple tracks associated to their clusters. The list of reconstructed tracks is looped over and a spatial matching procedure is performed for each EM cluster. χ^2 is calculated to find the quality of the track-to-cluster fit, and χ^2 is used to calculate the probability that our data matches the physical track of the photon. For photons this probability will still be small and only the highest probability of a matched track is kept.

4.4 Jet reconstruction

Jets are formed both by the hadronization of quarks produced in the hard interaction of an event, and by the soft gluon radiation in the detector. The characteristic of jets is that they deposit large amounts of energy in the hadron calorimeter. The schematic view can be seen in Figure 4.1. Jets with higher energy will deposit their

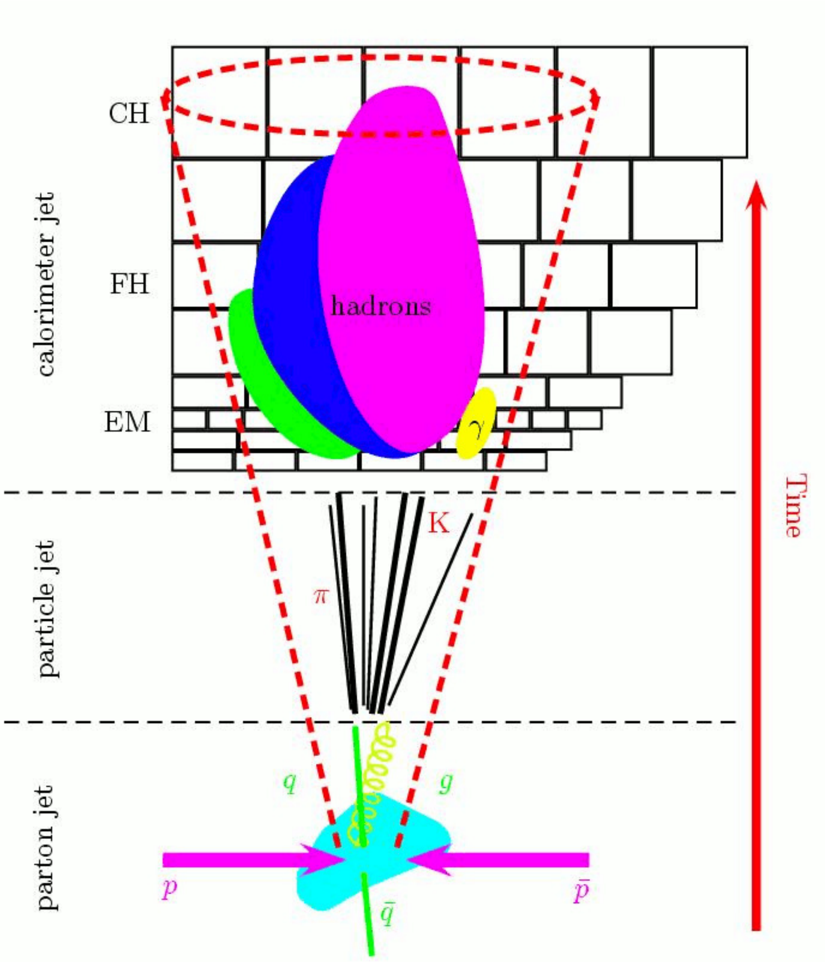

Figure 4.1: The jet showering in the detector.

energy in more collimated showers than will jets of lower energy. Jets are reconstructed in the calorimeter using the Run II Cone algorithm [72]. This technique is divided into three stages. The first stage is very similar to the SCone method used for photon energy clustering which was discussed earlier. This stage is known as pre-clustering and is described as follows:

- Make a list of all energetic towers with $E_T > 500$ MeV, ordered in decreasing E_T
- Form a circle of radius $\mathcal{R} = \sqrt{(\Delta\phi^2 + \Delta y^2)} = 0.3$ about a position of any given tower

- loop over all energetic towers within a distance of the seed cluster of $\Delta\mathcal{R} < 0.5$ and add the tower's energy to the seed cluster
- if the number of towers $N_{towers} < 1$, add the cluster to final list of pre-clusters.

After the pre-cluster list has been formed, it is re-ordered by descending E_T. In the second stage, this list of pre-clustered objects is taken to be the list of proto-jet candidates. For each pre-cluster P_i, the distance to each of its spatially neighboring pre-clusters P_j, where $P_j \neq P_j$, is calculated. A proto-jet candidate is formed if $\Delta\mathcal{R}(P_j, P_j) > 0.25$. The list of energetic towers is looped over, and E_T of each tower within this cone is summed with that of proto-jet and the position of proto-jet position is re-computed. This process goes until one of two cases occurs:

- all towers are looped
- the proto-jet has a stable position, such that $\Delta\mathcal{R}$ between two iterations of its position is < 0.001
- the limit of 50 towers iteration is reached.

Each proto-jet in the final list of proto-jets must exceed an energy threshold of 6 GeV, or else it is tossed out of the list. In the third stage of jet energy clustering, it is precisely determined whether the energy of proto-jet energy is actually only a part of a larger jet, or whether the energy is actually of multiple jets which have been interpreted as a single jet. To identify such events, we use the spacial midpoints of these jets. The technique used for accounting for these multi-jet cases is detailed as follows:

- A list of neighbouring proto-jets is made within the distance $0.5 < \Delta\mathcal{R} < 1.0$ for each proto-jet
- The clustering is redone without a $\Delta\mathcal{R}$ distance condition if there are proto-jets in this list

- Once the new proto-jet is formed, it is checked if the towers are shared among other proto-jets. In case it is true, following method is applied:
    - (i) If more than half of the energy of proto-jet is shared with another proto-jet, then the two proto-jets are merged into one
    - (ii) If less than half of the energy of proto-jet is shared with another proto-jet, then the energy is assigned to the closer of the two proto-jets and removed from the other.
- The final list of proto-jets is subjected to threshold of 6 GeV.

The proto-jets passing all these requirements are stored as calorimeter jets.

4.4.1 Jet Energy Scale

The energy resolution ($\frac{\sigma(E)}{E}$) of the calorimeter is given by the equation

$$\frac{\sigma(E)}{E} = \frac{A}{\sqrt{E}} + \frac{B}{E} + C \tag{4.4}$$

where A, B and C are constants. In this equation, there are parts that describe the energy resolution:

- the stochastic response ($\frac{A}{\sqrt{E}}$)
- instrumental effects ($\frac{B}{E}$)
- the constant term (C).

The first term accounts for the fluctuations in energy deposited per distance as the incoming particle creates a shower in the calorimeter. This effect significantly contributes to the entire accessible energy at the Tevatron due to dependence on the energy of the incoming particle. The second term is due to instrumental effects, such as electronic noise and pedestal fluctuations. Because this term is proportional to $\frac{1}{E}$, it significantly contributes to the overall energy resolution at low energies. The third term is a constant and the major contributions to its uncertainty come from calibration errors, higher order effects such as cell response linearity fitting, gain switching, non-uniformities in absorber material, and the amount of upstream material of the calorimeter. These things limit the performance of the calorimeter at high E_T.

Hence there are limitations to the calorimeter energy resolution that are inherent in the detector. There are many effects that must be understood even when considering just particle showers within the calorimeter. These are mainly energy loss of particle before reaching the calorimeter, the difference in energy response based on particle type, energy from other $p\bar{p}$ interactions convoluted with that of the measured particle, or showering effects of the particles that cannot be simulated with the available energy reconstruction algorithms. The true energy of the original jet can be determined using techniques that parameterize these effects. This is the main objective when applying the JES corrections, which is based on the energy depositions in the calorimeter [73]. The true energy of jet E_{jet}^{Part} can be parameterized in the following way:

$$E_{jet}^{Part} = \frac{E_{jet}^{Measured} - E_0(R, \eta, L)}{R_{jet}(E_{jet}^{Measured}, \eta) \times R_{cone}(R, E_{jet}^{Measured}, \eta)} \tag{4.5}$$

where the response (R) is written down in terms of the calorimeter response to hadronic jets (R_{jet}) due to the amount of measured energy ($E_{jet}^{Measured}$) and the fraction of energy of the jet which lies within the reconstruction cone (R_{cone}). These effects depend on instantaneous luminosity (L) and η and are therefore parameterized with respect to these quantities.

The jet energy scale can be separated into three parts: the fraction of energy of the jet inside the reconstruction cone (R_{cone}), the offset energy (E_0) and the calorimeter response to hadronic jets (R_{jet}). The fraction of the energy inside the reconstruction cone can be known by changing the size of the reconstructed cone. $\mathcal{R} = 0.5$ and $\mathcal{R} = 0.7$ are two standard cone sizes used at DØ. The energy measurement stability is studied against luminosity, pseudorapidity and the amount of hadronic energy deposited. The offset energy comes from adding the noise effects and the pile up from previous events.

4.5 Heavy Flavour Jet Identification

After the reconstruction of primary vertex and jets, their information is used to ascertain those jets coming from hadronized heavy flavour (HF) quarks. There are numerous algorithms that have been developed by the DØ collaboration to optimize the selection of these jets. Some of the discriminants use track-based techniques, and others use variables ascertained by reconstructing the displaced vertices, which we call "secondary vertices". For present study we determined the HF content of the sample of $\gamma + b$-jet and $\gamma + 2b$-jet events. Thus, an efficient algorithm that utilizes the unique properties of tracks and secondary vertices of jets that originate from HF quarks is required. This algorithm will suppress light jets (initiated by u, d and s quarks or gluons) and enrich our sample in HF jets. To understand these algorithms better, the general method of secondary vertex reconstruction is discussed below which is foundation for both vertex- and track-based techniques used at DØ.

4.5.1 Secondary Vertex Reconstruction

The decay of bottom and charm hadrons occurs at measurable distances from the primary interaction vertex because of their long lifetimes. The decay tracks originate from a secondary vertex which is displaced from the primary vertex. These tracks contribute a large χ^2 to the fitting of the primary vertex because they have

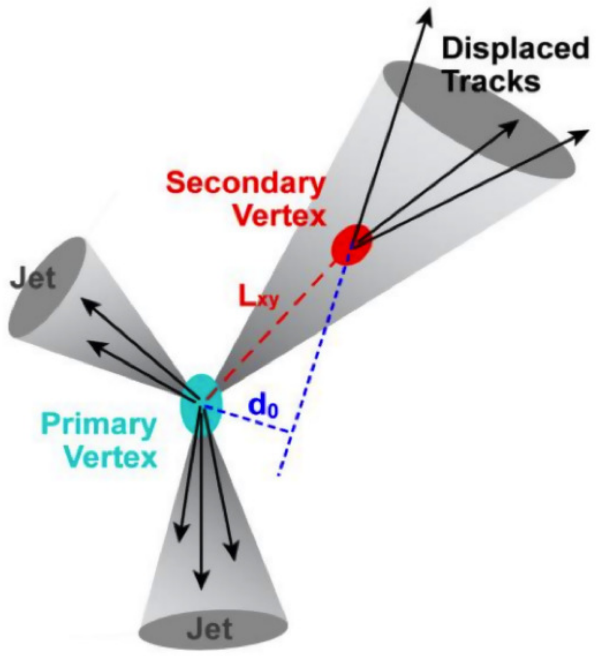

Figure 4.2: An example of a jet with tracks from a secondary vertex recoiling off two jets originating from the Primary Vertex. A secondary vertex is a signature of a HF jet. The displacement of the vertex, L_{xy}, and the IP, denoted d_0 in this figure, allow us to discriminate this jet from their light counterparts.

a larger IP than those tracks which come directly from hard scatter processes. A similar procedure is used to reconstruct additional vertices within jets [74]. In this technique, preselected tracks are to be found within the reconstructed jet and each track must have $|dca_{xy}| < 0.15$ cm, $|dca_z| < 0.4$, $p_T > 0.5$ GeV, and at least 2 SMT hits. From the list of tracks, the secondary vertex satisfies following:

- Tracks with large IP significance ($|S_{IP}| > 3.0$) are selected
- All 2-track seed vertices are found from these selected tracks
- Based on the χ^2 of the vertex, additional tracks pointing to seeds are attached
- Vertices based on decay length, collinearity angle and vertex χ^2 are selected.

This procedure gives two sets of lists as an output, one for the vertices from tracks with $|S_{IP}| > 0$ and the other from tracks with $|S_{IP}| < 0$. A track with

$|S_{IP}| > 0$ would indicate that the decay vertex was on the same side of the primary vertex as was the jet. On the other hand, a track with $|S_{IP}| < 0$ would imply a decay vertex on the side opposite from the jet. The vertices made from the tracks with negative impact parameter significance are known as negative tagged. Jets with these negative tagged vertices are mainly light flavour.

After forming the lists of secondary vertices, the next and final step is to make sure that the position of each reconstructed vertex is within the jet cone. This is done by subjecting it to $\Delta\mathcal{R}(vtx, jet) < 0.5$. The secondary vertices that pass this requirement are associated to the jet and their information is assessed in the search for HF jets.

4.5.2 *b*-jet identification algorithms

There are at present three low-level tools at DØ used to identify whether a jet is produced from a *b*-quark. The inputs to these tools can be combined using multivariate techniques to further improve their individual discriminating power.

Counting Signed Impact Parameter (CSIP) CSIP is the most basic algorithm utilized at DØ for HF jet identification [75–77]. It uses tracks with large $|S_{IP}|$ values as the basis for its discrimination algorithm. Tracks associated to the jet are required to pass through a preliminary set of selection criteria, including a track $p_T$greater than 1.0 GeV. At least two SMT hits must be associated to the track and it must have an $|dca_{xy}| < 0.2$ cm. The list of tracks that satisfy these criteria is stored. The S_{IP} of each track in the list is calculated. A scale factor a was introduced to optimize the discrimination of this variable: $S_{IP} \to RS_{IP} = S_{IP}/a$, where the optimal value of a was found to be 1.2. To select a jet as HF, it must have at least two tracks with $RS_{IP} > 3$, or at least three tracks with $RS_{IP} > 2$. A combined single discriminant can be achieved using CSIP information by summing together the weighted number of tracks that have $RS_{IP} > 3$ with the weighted number of tracks that have $RS_{IP} > 2$.

Jet Lifetime Impact Parameter (JLIP) The JLIP algorithm verifies that all of the tracks in a jet originate from within the PV [75]. First, the probability that each track originated from within the PV is calculated. These probabilities are then combined for all the tracks matched to a jet to determine the probability that the track originated from the PV. The probability of jet (P_{jet}) is defined such that the smaller value of P_{jet} is less likely to have originated from the primary vertex. Therefore, light jets will have a flat JLIP distribution ranging from 0 to 1, while HF jets will peak at low values.

Secondary Vertex Mass The secondary vertex mass, M_{SV}, is the invariant mass reconstructed from the momenta of all tracks associated with the most significant secondary vertex. b-jets tend to have a greater M_{SV}.

Secondary Vertex Tagger (SVT) The SVT technique provides many interesting quantities to increase the fractions of heavy flavour jets in a given sample. Comparing the outputs of different SVT techniques provides us with most of our discriminating power [78]. The individual discriminants comprising the SVT are discussed below.

The transverse decay length of the secondary vertex (DL_{XY}) is defined as the difference in the transverse positions between the primary vertex and secondary vertex. DL_{XY} and the uncertainty associated with it ($\sigma_{DL_{XY}}$) are used to calculate the transverse decay length significance as $S_{DL_{XY}} = \frac{s_{DL_{XY}}}{\sigma_{DL_{XY}}}$. A minimal requirement on this quantity applies a cut on the decay length significance such that $S_{DL_{XY}} > 2.5$. There are other discriminants coming from each secondary vertex, including χ^2 value of fitted position, the total number of tracks associated to it, and its reconstructed mass. Using the combinations of these variables, more strict conditions can be applied to the jet to further increase the fraction of heavy flavor jets in the data sample. In the following section we will discuss how further improvements have been achieved using an extended set of input variables and making use of decision trees and a neural network. The new algorithm which results from these improvements is known as the MVA *bl* discriminant ($\mathrm{MVA_{bl}}$) or MVA *b*-tagger.

4.6 $\mathrm{MVA_{bl}}$ algorithm

To build the $\mathrm{MVA_{bl}}$ algorithm, two samples are built: 10^6 signal events (MC sample of di-*b* jet events) and 10^6 background (MC sample of light jet events). A large number of variables are taken (discussed in details in [79]) and six random forests (RF) are trained [80] using the root Toolkit for Multivariate Analysis (TMVA) [81] framework. One RF is trained using the IP-properties and the five other RFs are trained using the sets of SVT variables obtained from the five different SVT configurations. These six RFs are then combined using a neural network implementation, the TMultilayerPercepton (MLP), from the root [82] framework. This neural network uses the non-linear correlations between these inputs to produce the $\mathrm{MVA_{bl}}$ output. This process gives enhanced discrimination over the DØ Neural Net (NN) algorithm by using an order of magnitude more variables for training. The final trained algorithm highly suppresses the background events using the complementary information supplied by these RFs.

4.6.1 Input Variables

In addition to the M_{SV} and JLIP variables discussed above, the $\mathrm{MVA_{bl}}$ makes use of 7 more input variables, which are as follows:

(i) The reduced JLIP (rJLIP). This is the value that the JLIP would acquire if the track which is least likely to have originated from the PV is removed

(ii) The number of tracks that are used in the SV reconstruction

(iii) The number of SVs

(iv) The value of χ^2/NDF in the SV fit

(v) The decay length significance in the transverse plane with respect to the PV, S_{xy}

(vi) $\Delta\mathcal{R}$, in Δ, ϕ space between the jet axis and the vector constructed from the difference in PV and SV locations

(vii) A composite variable based on the number of tracks with an IP significance greater than some optimized value.

MVA$_{\mathrm{bl}}$ constructs a continuous distribution in which, jets that are b-like are close to the upper limit of the distribution at 1, while the light jets are close to the lower limit at 0. Figure 4.3 shows the output of the MVA for b-jets, c-jets and light-jets. When compared to the previous DØ NN algorithm, the MVA$_{\mathrm{bl}}$ algorithm shows a significant improvement in discriminating between b-jets, c-jets and light-jets. A measure of this discriminating power is given by the performance profile, or the identification efficiency, of a b-jet as a function of the misidentification rate. A performance comparison of the DØ NN and MVA$_{\mathrm{bl}}$ algorithms can be seen in Figure 4.4. At low values of misidentification rates MVA$_{\mathrm{bl}}$ performs much better than the DØ NN algorithm, while at high values they produce similar b identification efficiencies. The DØ NN algorithm was trained using only nine variables combined with a neural network. The enhanced performance of the MVA$_{\mathrm{bl}}$ algorithm is due to the large increase in the number of variables used in the training and the two step procedure which allowed for a combination of complementary information [79].

Based on this, we can have a set of benchmark points, known as operating points (OPs), for which we precisely measure the efficiency and misidentification rates. For the MVA$_{\mathrm{bl}}$ algorithm there are twelve OPs assigned with the following names:

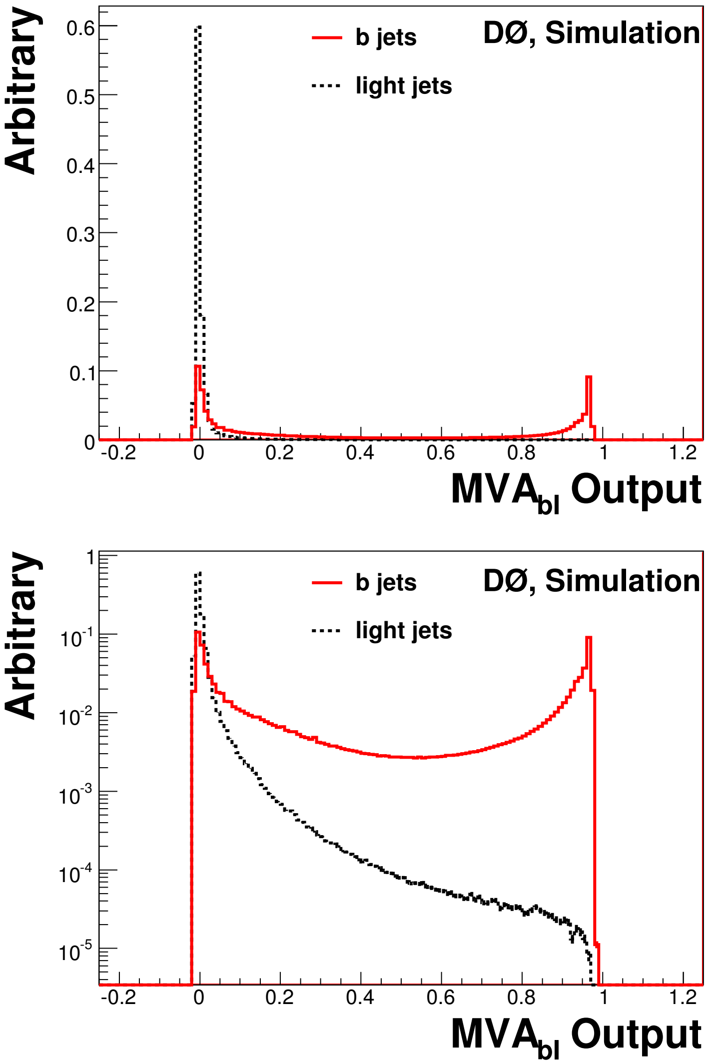

Figure 4.3: The MVA$_{\mathrm{bl}}$ output for light flavoured jets (dashed line) and b-jets (solid line) in simulated events, in linear scale (top) and logarithmic scale (bottom). The distributions are normalized to unity.

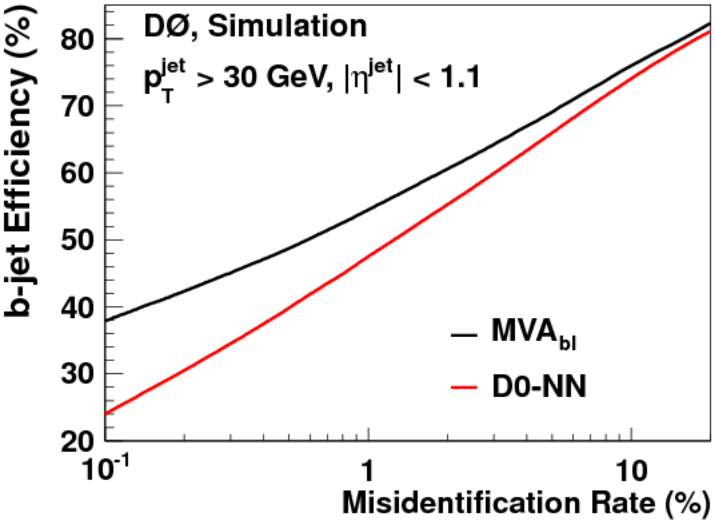

Figure 4.4: The performance profile of the MVA$_{\rm bl}$ (in black) and DØ NN algorithm (in red) for jets with $|\eta| < 1.1$ and $p_T > 30$ GeV for MC .

L6 , MVA$_{\rm bl} > 0.020$;

L5 , MVA$_{\rm bl} > 0.025$;

L4 , MVA$_{\rm bl} > 0.035$;

L3 , MVA$_{\rm bl} > 0.042$;

L2 , MVA$_{\rm bl} > 0.05$;

Loose , MVA$_{\rm bl} > 0.075$;

oldLoose , MVA$_{\rm bl} > 0.10$;

Medium , MVA$_{\rm bl} > 0.15$;

Tight , MVA$_{\rm bl} > 0.225$;

VeryTight , MVA$_{\rm bl} > 0.30$;

UltraTight , MVA$_{\rm bl} > 0.40$;

MegaTight , MVA$_{\rm bl} > 0.50$.

4.7 Missing Transverse Energy (E_T^{miss})

Neutrinos are weakly interacting particles which pass through the detector without producing any electronic signal. So, neutrinos are not detected at all in the DØ detector, and their presence must be realized from energy imbalance in the transverse plane. Before the collision, the proton and antiproton only have momentum in the z direction, so the momentum in the xy plane, the transverse momentum, is zero. Due to conservation of energy and momentum, the momentum after collision will be zero too. This fact can be used to determine the presence of particles that escape the detector without being detected neutrinos being the most likely candidates. The missing transverse energy, (E_T^{miss}), is defined as the negative of the vectorial sum of the transverse momenta of particles observed in the detector. We calculate the E_T^{miss} by adding up vectorially the transverse energies in all cells of the EM and FH layers of the calorimeter [83]. There are some corrections which are applied to the missing transverse energy for the following cases:

- The missing transverse energy needs to be corrected if there are reconstructed muons in the event. Because muons deposit a small amount of its energy in the calorimeter, it must be subtracted.
- The jet energy scale correction alters the balance in the transverse plane. The momentum component due to each jet energy scale needs to be subtracted from the raw E_T^{miss} .
- The E_T^{miss} is corrected for the coarse hadronic calorimeter energy belonging to the jets in each event. Due to the presence of large amount of noise, the energy in the coarse hadronic calorimeter is not taken into account.
- There are also small corrections required when there are electrons and photons in the event due to the electron and photon energy scales.

Now the foundation has been laid for the studies presented in this thesis. Next step is to utilize these physical objects and calculate the desired cross sections which is described in next two chapters.

Chapter 5

$\gamma + 2b$-jet Differential Cross section Measurements

This chapter presents the measurement of production cross section of $\gamma + 2b$-jet and the ratio of $\gamma + 2b$-jet to $\gamma + b$-jet.

For this firstly, the signal events were selected and then the efficiency of signal events to pass that selection criteria was calculated. After that the signal purity was estimated. The following sections will describe all the steps and elements that lead to the measured cross section.

5.1 Event Selection

The selection criteria for direct photon plus at least two heavy flavour jets is optimized such that it identifies the signal events and minimizes the background events. It is divided into two parts: photon selection and jet selection. Then their corresponding efficiencies for individual requirements were calculated which was followed by the estimation of the photon purity and amount of heavy flavour jets in data sample. The analysis was done in each region of p_T^γ with five bins corresponding to [30-40, 40-50, 50-65, 65-90, 90-200 GeV]. Events were selected if they satisfied the following criteria:

- The primary vertex has at least three associated tracks and $|z_{PV}| < 60$ cm
- There should be at least one photon with $p_T^{\gamma} > 30$ GeV and $|y^{\gamma}| < 1$. Standard DØ fiducial cuts are applied to avoid inter-calorimeter boundaries and cracks. A photon candidate should satisfy the selection criteria described in detail in the next section.
- There should be at least two jets with $p_T^{\text{jet}} > 15$ GeV and $|y^{\text{jet}}| < 1.5$
- The photon candidate and a jet have to be separated by $\Delta R > 0.7$
- To suppress background from $W \to e\nu$ events and cosmics, the missing transverse energy in the event is required to fulfill $E_T^{\text{miss}} < 0.7 \times p_T^{\gamma}$.

Also, since the measurement of cross section involves *isolated* photons, the true/generator level photons were required to be isolated in $R = 0.4$ by a total scalar pT sum of all stable particles. That is the definition of the (isolated) photon+$b(2\ b)$ jet production cross section. The theoretical predictions to which the measured cross-sections were compared to were also done with same isolation condition.

5.2 Photons

To select photon candidates for data and Monte Carlo event analyses the CORE-2 photon definition with a set of selections that have been certified by EMID group were used. The description of those selections is provided below :

- EM object is reconstructed using Simple Cone algorithm
- Central photons are considered with $|y^{\gamma}| < 1.0$ and $p_T^{\gamma} > 30$ GeV
- To avoid inter-calorimeter boundaries and cracks, the EM η and ϕ fiducial cuts are applied

- Each candidate is required to deposit more than 97% of the detected energy in the EM section of the calorimeter (EMfrac > 0.97),
- And to be isolated in the angular region between $R = \sqrt{\Delta\eta^2 + \Delta\phi^2} = 0.2$ and $R = 0.4$ around the gravity center of the cluster: $Iso(\Delta R_{02}) < 0.07$. Here $Iso(\Delta R_{02)} = (E_{iso}^{Tot} - E_{iso}^{Core})/E_{iso}^{Core}$, where E_{iso}^{Tot} is overall (EM+hadronic) tower energy in the (η, ϕ) circle of radius $R = 0.4$ and E_{iso}^{Core} is EM tower energy within a radius of $R = 0.2$.
- Photon candidate is also isolated in the tracker by $sum_{track}^{P_T} < 1.5$ GeV, where $sum_{track}^{P_T}$ is a scalar sum of track transverse momenta (p_T^{tr}) in the ring of $0.05 \leq R \leq 0.4$. Only the tracks produced within 2 cm from the primary vertex in z with $p_T^{tr} > 0.4$ GeV are considered.
- The probability to have any track spatially matched to the EM cluster is required to be < 0.
- HMx7(8) <30.0 is required for CC photons;
- Energy weighted EM cluster width in $r \times \phi$ ($\Sigma(R, \phi)$) is restricted at EM3 layer to $\Sigma(R, \phi) < 18\ cm^2$
- Finally, a cut on the photon artificial neural network (ANN) output is required $O^{\mathrm{NN}} > 0.3$ for CC photons. It is based on the photon ANNs trained for CC Photons.

5.3 Jets

Jets were reconstructed using the DØ Iterative Midpoint Cone algorithm with a cone size $R = 0.5$. Jets were selected if they fulfilled the *good* jet criteria as defined in [84] and the jet energies were corrected by the standard JES with muon corrections. The jets were also required to satisfy the b-tagging requirements which will be described in the following section.

5.4 Cross Section Calculation

It is important to know how physical observables which we utilized for the selection criteria translate into the measured calculation. This was achieved by combining acceptance ($\mathcal{A}$), luminosity ($\mathcal{L}$), trigger efficiency (ϵ_t), photon and jet selection efficiencies ($\epsilon_s^{\gamma}, \epsilon_s^{\text{jet}}$), primary vertex efficiency (ϵ_{pv}), b-tagging efficiency ($\epsilon_{bb}^{\text{jet}}$), E_T^{miss} efficiency ($\epsilon_{E_T^{\text{miss}}}$), photon and b-jet purities ($\mathcal{P}_{\gamma}, \mathcal{P}_b$) to evaluate the differential cross sections as shown in Equation 5.1:

$$\frac{\mathrm{d}\sigma}{\mathrm{d}p_T^{\gamma}} = \frac{N_{\text{Events}}\ \mathcal{P}_{bb}\ \mathcal{P}_{\gamma}}{\Delta p_T^{\gamma}\ \epsilon_t\ \epsilon_s^{\gamma}\ \epsilon_s^{\text{jet}}\ \epsilon_{pv}\ \epsilon_{bb}^{\text{jet}}\ \epsilon_{E_T^{\text{miss}}}\ \mathcal{L}\ \mathcal{A}}. \tag{5.1}$$

This section explains each of these factors in more details to provide the measured cross section.

5.4.1 Efficiencies

5.4.1.1 Trigger

Triggering is done with respect to the photon candidates electromagnetic (EM) calorimeter energy distribution. Triggers are contained in the trigger list which contains all the triggers used in a given timespan when collecting data. The triggers within them have improved over the time. For this analysis, the data was selected using a logical OR combination of the unprescaled CALONLY EM triggers (of versions v15, v155, v16). Only one trigger was required to be satisfied or fired for the considered event. However, the differences in trigger are mainly because of the threshold p_T of the object, many of these will overlap and will have satisfied multiple triggers. It is important to note that the triggers used were unprescaled which means that the rate at which they were fired is not limited due to an overabundance of events , thus this potential bias can be avoided. Their efficiency was calculated using photon identification tools in the Common Analysis Format (CAF) framework by EMID group. Typical trigger efficiencies for the OR combination in the first bin of our measurements (30–40) in CC is $\gtrsim 96\%$ and almost 100% for $p_T^\gamma > 40$ GeV.

5.4.1.2 Vertex selection

Events were required to have a z position of the best primary vertex within $|z_{PV}| <$ 60 cm from the center of the detector and to have at least three tracks associated to it, $N_{PV}^{tracks} \geq 3$. The photon can be in central or forward rapidity region and the jet satisfies the b-tagging requirement. Efficiency to pass these two criteria was calculated using Pythia $\gamma + b$ MC for different run periods. The efficiency was calculated with requirement of the b-jet with $p_T^{\text{jet}} > 15$ for CC. The vertex selection efficiency is $\approx(96 - 98)\%$, depending on p_T^γ.

5.4.1.3 Photon selection

Photon candidates with transverse momenta greater than 30 GeV and $|y| < 1.0$ were ordered in p_T and made to go through various selection criteria to reject the jets that deposit their energy in the EM calorimeter (EM-like jets) as discussed earlier in Section 4.3.3. Jets in general consist of mainly light mesons, and there are high momenta mesons in EM-like jets. These mesons decay to photons and deposit their energy in EM layers of the calorimeter, mimicking the signal of direct photons. Typically, these type of mesons are created through charge-exchange, such as:

$$\pi^- p \to \pi^0 n$$

where n is the neutron. In this case, the produced π^0 meson almost always decays into two photons and if the π^0 meson has enough of the original partcile's momentum, then the two photons will be collinear and can be reconstructed as single photon candidate. The final state of dijet events has a much larger cross-section than that of direct photon and jet. Thus, even though only a small fraction of jets are EM-like, dijet events containing one EM-jet will greatly outnumber the signal events. However, the properties of EM-like jet differ from direct photons in some ways. EM-like jets have a large particle multiplicity from the hadronization of gluons or quarks as compared to the direct photons. Thus the energy depositions of EM-like jets in the calorimeter is more likely to be spatially wider and less constrained to the EM layers of the calorimeter. Also, the charged particles within these jets interact with the CFT and SMT, and the tracks associated with these clusters. On the other hand, single photons do not have tracks as they most of the times convert to electron positron pairs in the calorimeter. These EM-jet like properties provide the basis for discriminants which are essential for the identification and the removal of background from the signal photon sample. This criteria have been optimized to retain a very high signal efficiency, while rejecting the background jets. The efficiency was calculated with respect to the photon criteria listed earlier in Section 5.1 for the events preselected with the reconstruction level cuts shown below in Eq. (5.2).

$$
\begin{aligned}
&\text{Generation level}: p_T^{\gamma} > 30\,\text{GeV},\ |\eta| < 1.0,\ E_T^{sum}(R_{\gamma}^{iso} = 0.4) < 2.5\,\text{GeV} \\
&\text{Reconstruction level}: p_T^{\gamma} > 30\,\text{GeV},\ |\eta| < 1.0,\ |\eta^{det}| < 1.0,\ EMfrac > 0.90, \\
&\qquad Iso < 0.15,\ |ID| = 10, 11 \text{ in } \eta \text{ and } \phi \text{ fiducial regions.}
\end{aligned} \tag{5.2}
$$

Even after this, there existed a large amount of background , mainly from dijet events. To further suppress this background and to estimate amount of signal γ-ANN was used. It was used to provide a criterion for increased photon purity and as shape template for photon purity estimation. With the help of neural networks, one can perform a multidimensional cuts, which reduces the background further more by taking into account the correlations among various discriminants. The main advantage of using neural network is that it can be trained to recognize patterns among identification variables. It is trained such that signal events peak at one, while that of background yields an output zero. The photon ANNs in CC regions have been extensively tested on $Z \to ee$ and $Z \to l^+l^-\gamma$ events in MC and data. Fig. 5.1 show ANN outputs O^{NN} in those events [86]. The shape of output for data indicates that a significant contribution of EM-like jets contaminate signal. Therefore, to improve the fraction of events coming from signal photons in the data sample, photon candidate's γ-ANN output was required to be greater than 0.03 ($O^{\mathrm{NN}} > 0.3$).

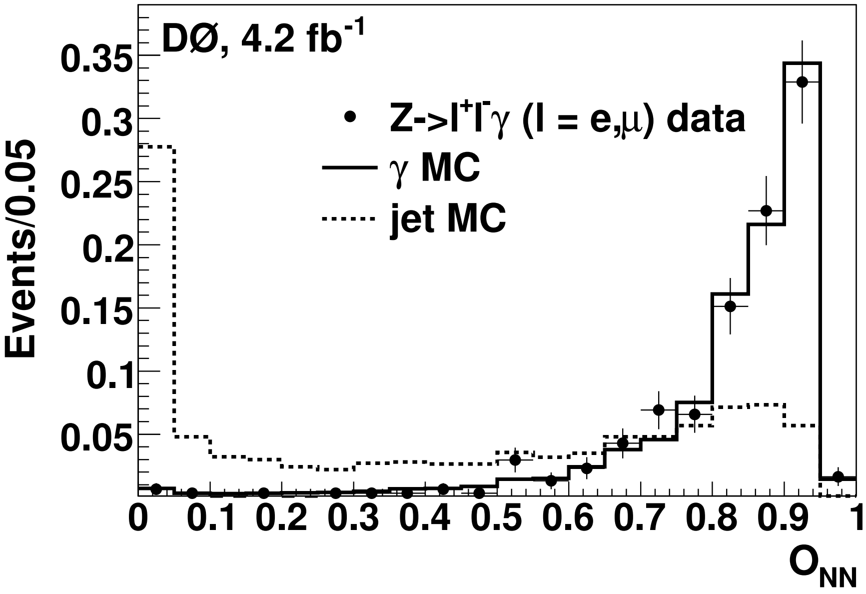

Figure 5.1: Comparison of the normalized O^{NN} spectra for photons from the photon MC and $Z \to l^+l^-\gamma$ data data and for misidentified jets from dijet MC in CC regions.

The MC modeling of the O^{NN} shape for EM-jets was validated in a sample of selected photon candidates by inverting the photon isolation ($Iso > 0.07$), a requirement that significantly enriches the sample in jets. The comparison of data to MC ANN outputs in CC rapidity regions is shown in Fig. 5.2. The photon efficiency to pass photon identification criteria is $(71 - 82)\%$ with 3% systematic uncertainty.

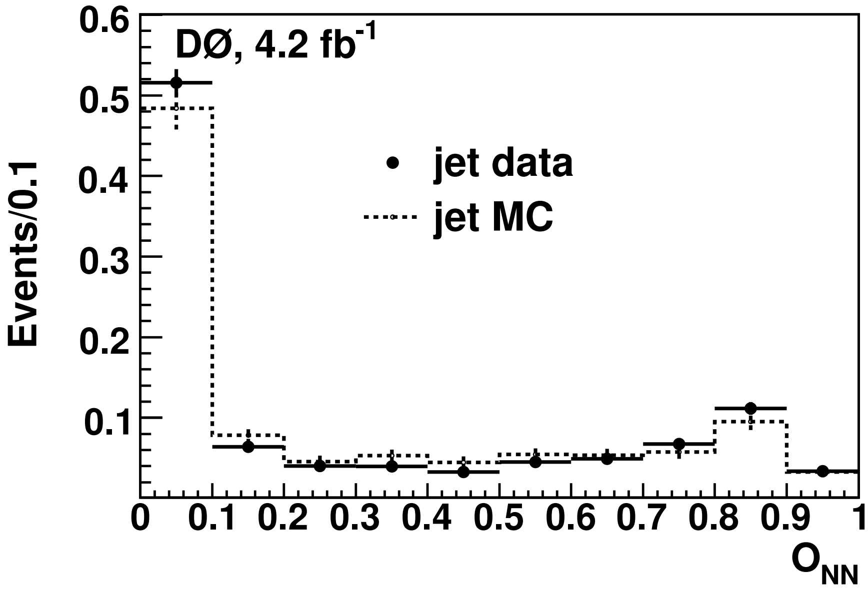

Figure 5.2: Comparison of the normalized O^{NN} spectra for EM-jets in data and MC in CC regions.

5.4.1.4 E_T^{miss} cut

Missing transverse energy (E_T^{miss}) in photon plus at least one (two) heavy flavor jet events is expected to be low, but there are two potentially large backgrounds which are expected to have large E_T^{miss}. The first of these is when a W boson decays into electron and neutrino ($W \to \nu$), and the electron is misidentified as photon. Additional jets from this interaction could be heavy flavor, but the presence of neutrino in the event results in large E_T^{miss}. The second case is from a cosmic muon that, through bremsstrahlung deposits a large amount of energy in the EM calorimeter. If this were to happen within the time frame of a heavy flavour dijet event then a photon and heavy flavour jets would possibly be reconstructed. In this case, there wil be an overall abundance of energy (large E_T^{miss}) because the cosmic muon's energy does not arise from the interaction.

To reject the events from either of these two cases, we imposed a E_T^{miss} limit. The condition to be used must be sufficiently loose to still retain a high signal efficiency. Applying $E_T^{\mathrm{miss}} < 0.7 \times p_T^{\gamma}$, the signal efficiency was high ($\geq 98\%$).

5.4.2 Taggability and b-tagging

Prior to applying b-tagging on jets, at least two jets were required to pass the taggability criteria. This requirement imposes a set of geometric constraints to ensure that the jet has sufficient information to be classified as a heavy flavor candidate. For a jet to be taggable, it must have at least two associated tracks with $p_T > 0.5$ GeV, the leading track must have a p_T of at least 1.0 GeV and both tracks must have at least one hit in the SMT. Figure. 5.3 illustrates the taggability efficiency of jets in γ+jet MC as a function of the photon p_T in central region. The 4% uncertainty on the taggability scale factor was used later for the cross section calculation.

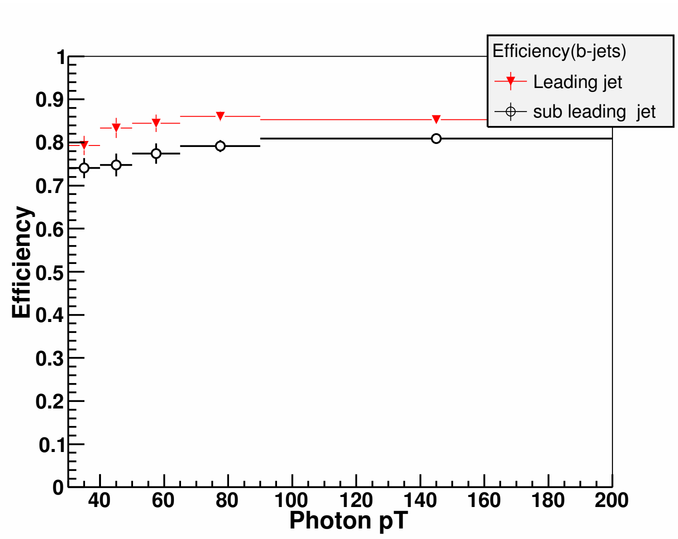

Figure 5.3: The jet taggability efficiency in MC for the leading b-jet and sub-leading b-jet in events with central photons a with b-ID scale factor applied.

In order to enrich the γ+jet sample with heavy-flavour jets, an MVA based b-tagging algorithm (MVA$_{\mathrm{bl}}$ tagger) was applied that exploits the longer lifetimes of b-flavoured hadrons in comparison to their lighter counterparts. The MVA$_{\mathrm{bl}}$ output distributions for three different flavored jets is illustrated in Figure. 4.3 in section 4.6.1. The events with at least one (two) b-tagged jet satisfying the VeryTight operating point of the MVA$_{\mathrm{bl}}$ tagger which corresponds to MVA$_{\mathrm{bl}}$ cut value of greater than 0.3 were selected. Depending on p_T^{γ}, this selection has an efficiency of (13 −

21)% for a $b\bar{b}$-jet pair with relative systematic uncertainties of $(4-6)\%$, caused by uncertainty on the data-to-MC correction factors. Only $(0.2-0.4)\%$ of light jets are misidentified as heavy-flavour jets.

5.4.2.1 Photon purity

After application of all selection requirements, 3,816 events remain in the data sample with "γ-candidate+b-jet" events. This sample is contaminated with a background stemming from QCD jets in which one of jets has fluctuated into a well-isolated single EM cluster. The cluster is caused mainly by energetic (single or multiple) π^0, η, K_s^0 or ω mesons decaying into photons in the final state. As a rule these background particles are accompanied by soft hadrons whose energy is mostly deposited in the electromagnetic shower developing within the EM cluster.

To reduce and estimate a remaining fraction of such a background we need physical variables sensitive to the internal structure of the shower. Additionally, behavior of these variables in MC simulation should be very close to those in data. The outputs of the photon artificial neural networks (ANN) for CC photons, trained on p20 MC direct photon and di-jet events and certified by EMID group.has been chosen as a discriminant between signal and background events.

Before estimating photon fractions, we have preselected signal MC and data events with the main photon and jet ID cuts listed in section 5 (i.e. including b-jet ID with requirement of $\mathrm{MVA_{bl}} > 0.3$). Due to a small statistics remaining in the EM-jet sample, events with different jet flavors have been re-weighted using TRFs for the output cut $\mathrm{MVA_{bl}} > 0.3$ instead of requiring a real "VeryTight" b-tag. Since the signal events cannot be identified on the event by event basis, their fraction (purity) $\mathcal{P}$ is determined for a given p_T bin statistically. The photon purity is defined as the ratio

$$\mathcal{P} = \frac{N^{\gamma}}{N^{\gamma} + N^{\mathrm{jet}}}, \tag{5.3}$$

where N^γ ($N^{\rm jet}$) is the number of single photons (EM-jets) that passed selection criteria (section 5.4.1.3), including photon ANN cuts , $O_{NN} > 0.3$.

To determine purity we have used a statistical/probabilistic method. The ANN output in data is fitted by ANN outputs from MC photon and EM-jet samples using TFractionFitter from ROOT package [1]. This routine correctly incorporates statistical errors in MC and data histograms and was specially written for fitting MC fractions to data histograms. With this technique, we have calculated the purities for the two photon rapidity regions as a function of p_T^γ. The MC-to-data template fit was done without imposing limits on the fractions of the signal and background samples to reflect and satisfy their possible statistical fluctuations (i.e., we do not require that the fractions are constraint to the interval [0,1]).

Test plots with results of individual fits in some p_T^γ intervals are presented in Figs. 5.4. Here, MC histograms are weighted according to their fractions found from the fit. The errors shown on the plots are statistical. They correspond to 68% confidence level for the two parameter fit (these parameters are the fitted values of signal and background fractions in the data) [88]. The uncertainty of the found purity points at high p_T intervals is mostly caused by data statistics, as well as by the statistics of the EM-jets sample which remained after the photonic selections. An independent fit is performed in each p_T^γ bin. We get photon fractions between 62% and 90%, which are shown in Fig. 5.5. Additional systematic uncertainty of photon purity is due to the fragmentation model used in PYTHIA and is caused by uncertainty in the fragmentation functions $D_{\pi,\eta}(z)$ at high z (or at small values of the isolation parameter $\epsilon = (1-z)/z$) [63, 89]. This uncertainty was estimated by increasing and decreasing amount of π^0 and η mesons in the EM-jet sample by a factor 2 and calculating purity using modified templates for EM-jets. It is found to be about 6% at $p_T^\gamma \simeq 30$ GeV, and $\leq 1\%$ at $p_T^\gamma \gtrsim 70$ GeV.

---

[1] It is based on the HMCMLL routine [88] from the HBOOK package.

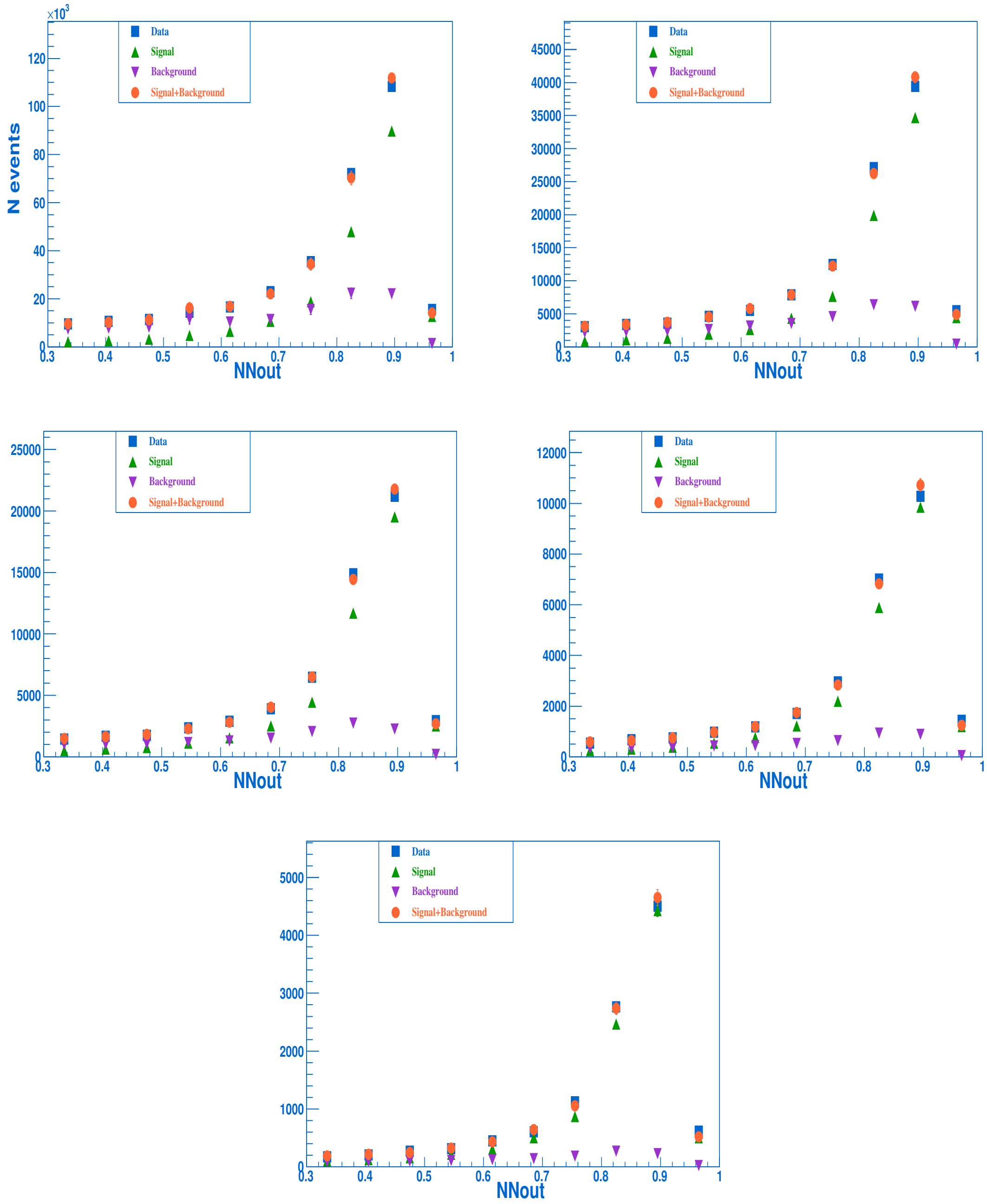

Figure 5.4: Distribution of the number of events in data over photon ANN output after the cut $O_{\rm NN} > 0.3$ for six p_T^γ intervals from 30 to 200 GeV. The fitted (to the data) distributions of the MC photons and EM-jets are also shown. They are weighted by their fractions found from the fit.

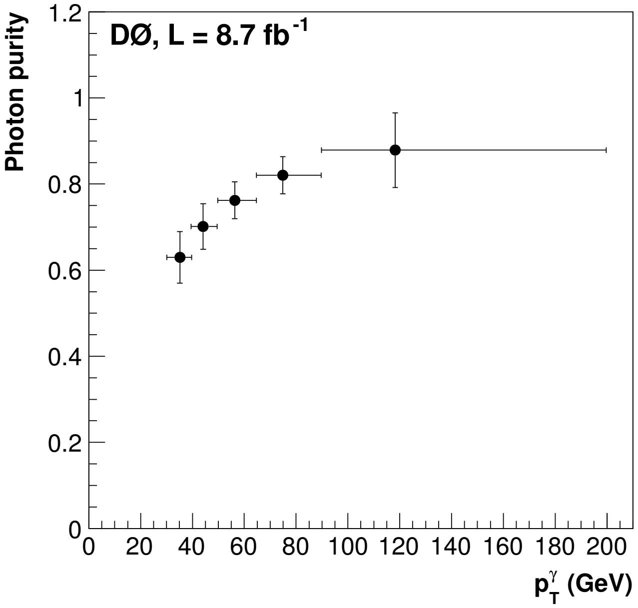

Figure 5.5: Photon purity as a function of p_T^γ in the selected data sample. The error bars include statistical and systematic uncertainties added in quadrature.

5.4.3 $\mathbf{D_{MJL}}$ Tagger

To further separate the b-quark jets from c and light-jets in the b-jet enriched sample, a discriminant ($\mathrm{D_{MJL}}$) was constructed from two variables which exploits the properties of tracks associated with the b-tagged jet. Equation 5.4 shows how the value of the $\mathrm{D_{MJL}}$ is calculated.

$$D_{\mathrm{MJL}} = \frac{M_{\mathrm{svt}}/5 - ln(JLIP)/20}{2} \tag{5.4}$$

Here, $JLIP$ stands for joint lifetime impact parameter and gives an overall probability for a jet to originate from the PV. Equation 5.5 shows how JLIP is calculated. The value is a product of the probability of each track originating at the PV (P^l_{track}).

$$JLIP = \prod_{l}^{N_{Tracks}} P^l_{Track} \tag{5.5}$$

In Figure. 5.6 (a) shows that jets from b quarks usually have smaller values of JLIP probability, where as light jets mostly have small values, as their tracks originate from the PV. M_{SVT} is the invariant mass of the tracks forming the secondary vertex, which provides good discrimination between b, c and light jets due to different masses of the quarks (Figure. 5.6 (b)). The two variable takes into account the kinematics and geometry of the event, respectively, and the $\mathrm{D_{MJL}}$ thus formed from the combination has an improved discriminating power for b, c and light jets. The typical value for negative log of $JLIP$ falls between 0 and 20, while the typical M_{SVT} is between 0 and 5 GeV. In the construction of the MJL discriminant, the distribution of the two variables have been forced to be mostly between 0 and 1.

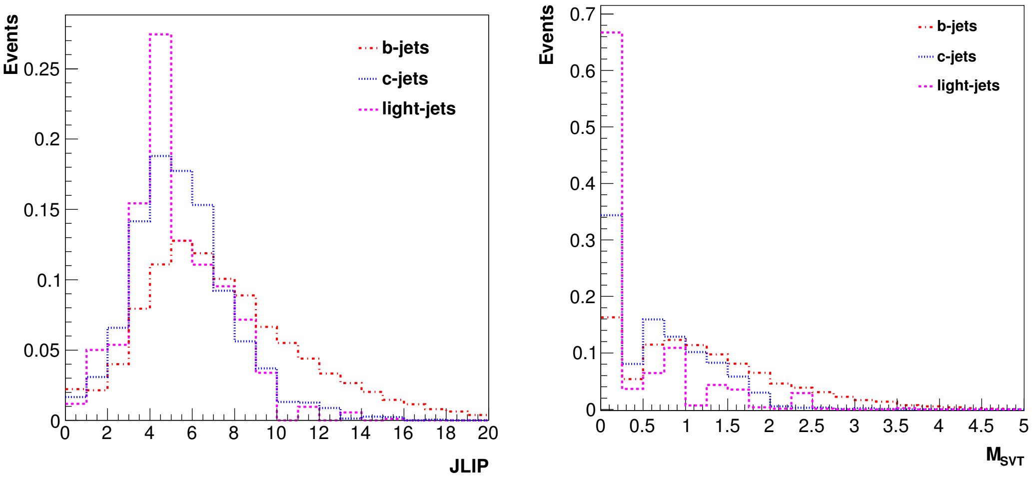

(a) -log(JLIP) (b) SVT Mass

Figure 5.6: (a) -log(JLIP) distributions and (b) SVT Mass distributions for b, c and light jets.

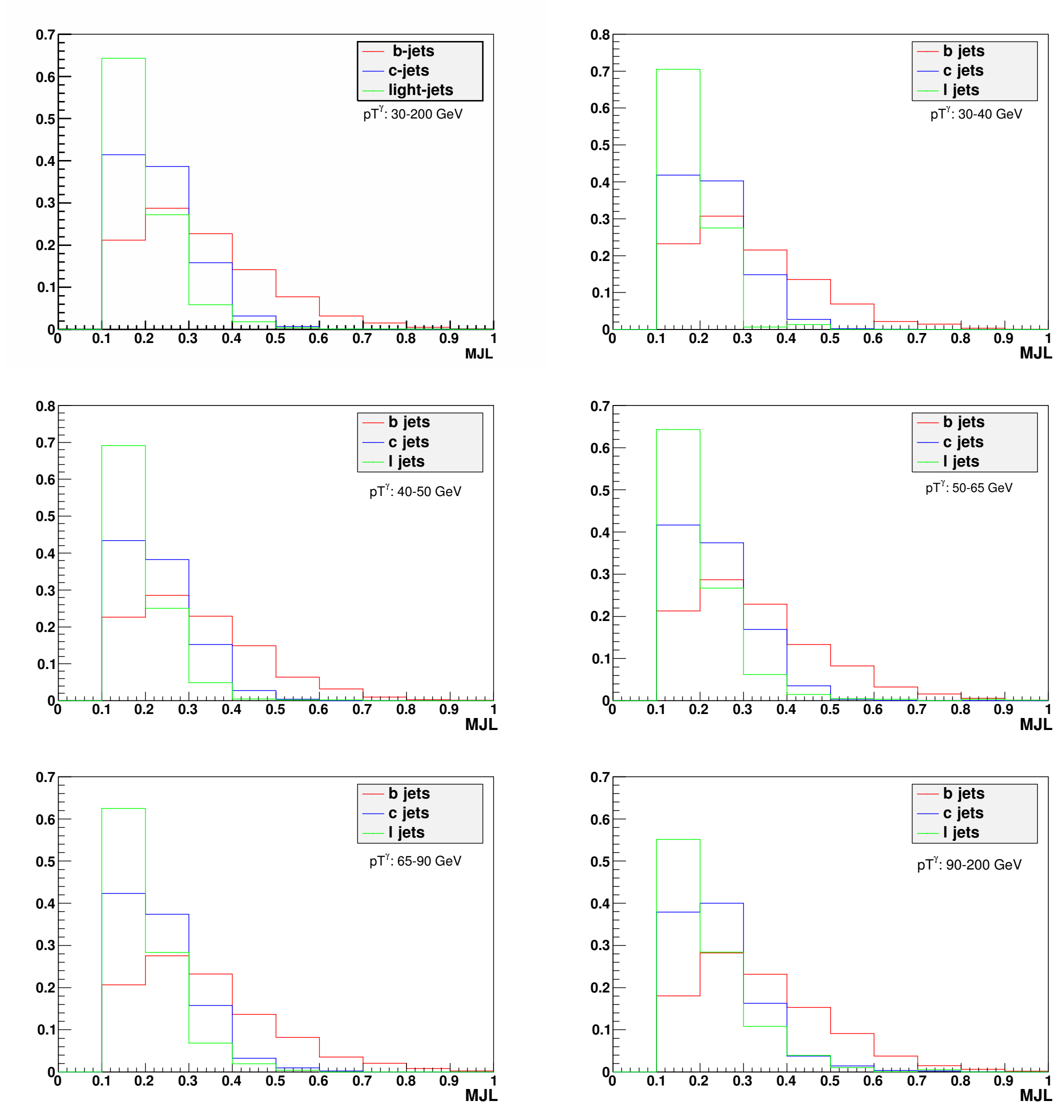

Figure 5.7: $D_{\rm MJL}$ distributions for b, c and light quark jets passing VeryTight MVA BL tagger operating point for photons in different bins of photon transverse momentum.

p_T^γ (GeV)	bb	cc	bc	bl	cl	ll
30 – 40	0.72±0.05	0.26±0.05	0.01±0.002	0.0	0.01±0.001	0.0
40 – 50	0.72±0.05	0.24±0.05	0.02±0.004	0.01±0.01	0.01±0.001	0.0
50 – 65	0.71±0.04	0.18±0.03	0.03±0.01	0.05±0.02	0.03±0.01	0.0
65 – 90	0.73±0.02	0.19±0.02	0.02±0.004	0.03±0.01	0.02±0.01	0.0
90 – 200	0.81±0.02	0.12±0.02	0.03±0.01	0.02±0.01	0.01±0.002	0.0

Table 5.1: The fractions of various compositions of jets beauty, charm and light flavor jets in SHERPA sample.

Figures. 5.7 show the $\mathrm{D}_{\mathrm{MJL}}$ distributions of tagged jets of different flavors in different photon transverse momentum bins which provide good discrimination between b jet versus c and light jets counterparts. As it can be seen that the b-jets have a larger M_{SVT} on average than c-jets or light jets due to the large mass of b hadrons. With tighter requirements on b-tagging operating point, the discrimination between shapes for c and light jets reduces, but, the overall discrimination between b-jets and others remain very well preserved and this is very important for the current analysis. The dependence of the jet flavour templates on photon p_T was studied and they showed a weak dependence on photon p_T. The data sample with two HF-tagged jets was fitted to templates consisting mainly of 2 b-jet and 2 c-jet events, as determined from MC simulation. The remaining jet flavour contributions in the sample (e.g., light+light jets, light+$b(c)$ jets, etc) were small and were subtracted from the data. The fractions of these rarer jet contributions were estimated from SHERPA simulation (which has been found to provide a good description of the data), and vary in the range $(5-10)\%$. The predictions from SHERPA sample are shown in Table. 5.1. We did the same studies for PYTHIA. The difference in the values of these fractions obtained from SHERPA and PYTHIA, $(2-4)\%$, was assigned as a systematic uncertainty on the background estimate. The fraction of 2 b-jet events were determined by performing a two-dimensional (corresponding to the 2 b-jet candidates) maximum likelihood fit of D_{MJL} distributions of 2 jet events in data using the corresponding templates for 2 b-jets and 2 c-jets. These jet flavour templates were obtained from MC simulations. Figures 5.8 show results of these likelihood fits in all the photon p_T bins considered in the analysis. These figures shows the one-dimensional projection onto the highest p_T jet D_{MJL} axis of the 2D fit, normalized to the number of events in data, for photons with $30 < p_T^{\gamma} < 200$ GeV. An independent fit was performed in each p_T^{γ} bin, resulting in extracted fractions of 2 b-jet events between 76% and 87%. It can be seen that the distribution of the $\mathrm{D}_{\mathrm{MJL}}$ in data is described reasonably well with the photon plus jet components of different flavours. The 2 b-jet and b-jet fractions determined from the template fitting is shown in Fig. 5.9 for different photon p_T bins considered in the analysis for the central and forward photons. As one can see, the b-jet fraction tends to increase slightly with rise in photon p_T as well.

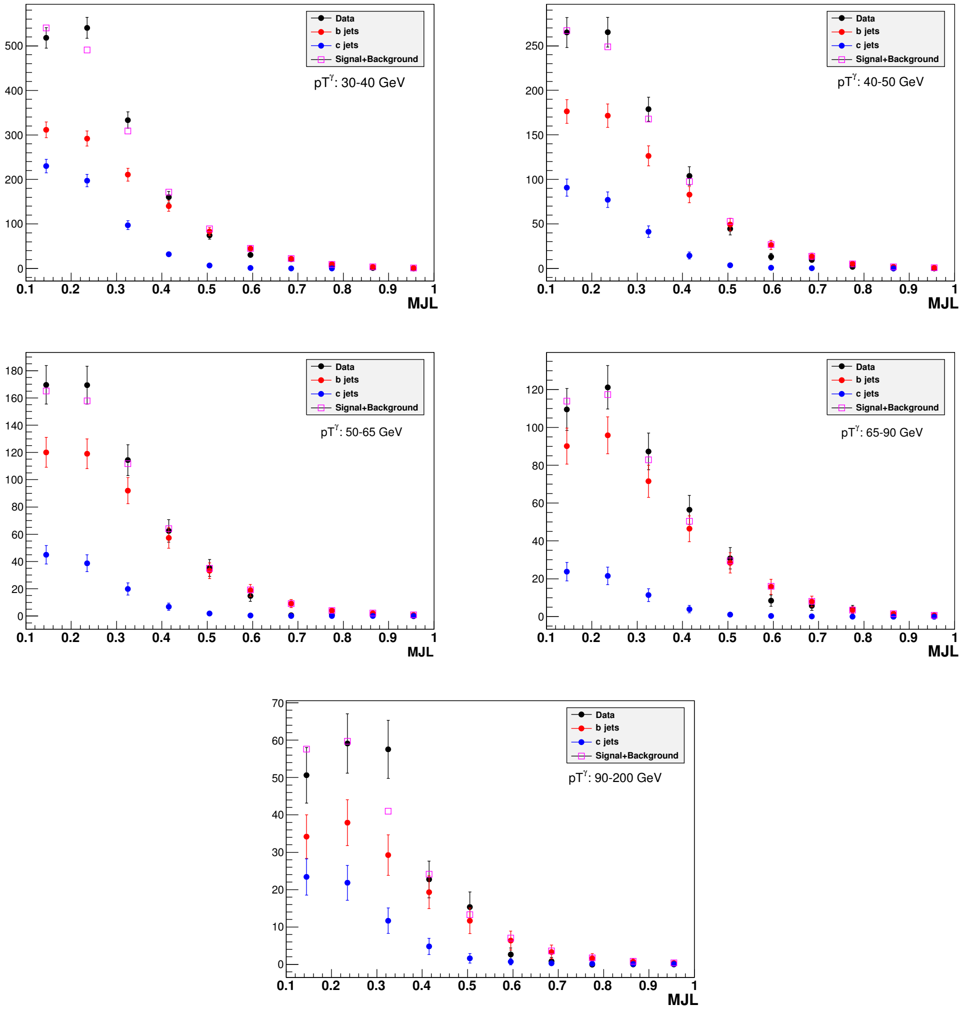

Figure 5.8: Results of the D_{MJL} fit for central photons in different p_T^γ bins.

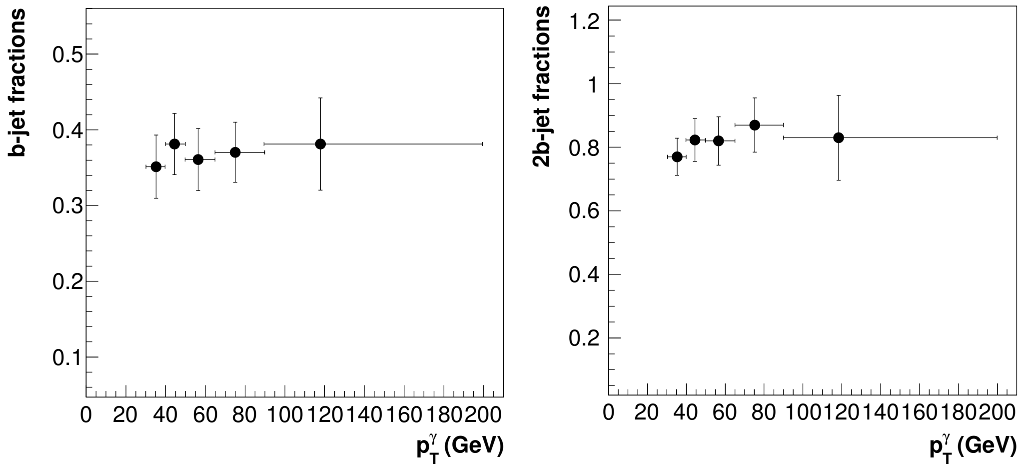

Figure 5.9: The b (left) and 2 b-jet (right) fractions in data as a function of p_T^γ derived from the template fit to the heavy quark jet data sample after applying all selections. The error bars show both statistical and systematical uncertainties summed in quadrature. Binning is the same as used for template fitting.

5.4.4 Acceptance

An important factor to be taken into account when analyzing DØ data is the efficiency of the detector itself to measure the signal events. This is very important for photons especially because their showers are small spatially. In order to understand this thoroughly the amount of signal lost to the constraints enforced by the detector geometry was studied. The photon and 2 b-jet acceptances using $\gamma+$ jet simulated samples were calculated. Simulated γ+jet samples used were generated from leading order Monte Carlo event generators PYTHIA and SHERPA (details in Section 3.1.2). Figures. 5.10 - 5.11 show the normalized distribution of the number of events in data, PYTHIA and SHERPA for photon and 1st and 2nd jet in p_T and η after the jet taggability requirement. Also, data points here were corrected for the photon purity (estimated in Section 5.4.2) and b-purity (estimated in section 5.4.2.1). As one can see from the plots , that SHERPA describes the data better, therefore SHERPA samples were used to calculate central acceptance values.

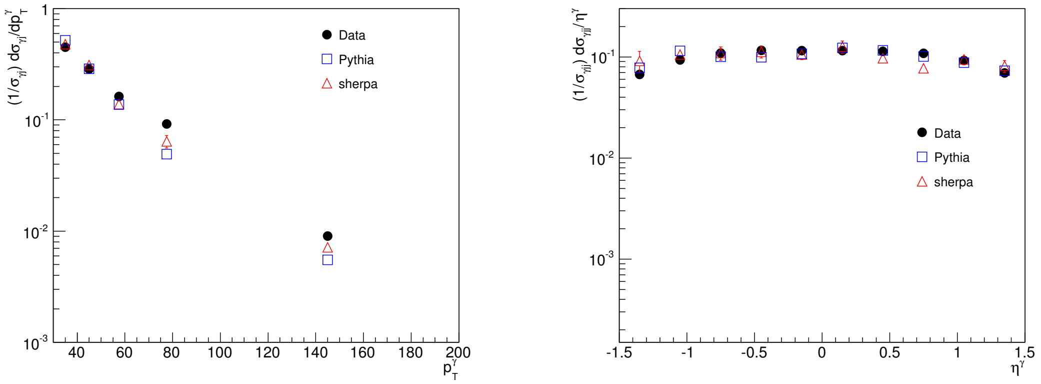

Figure 5.10: The normalized photon p_T (left)and η (right) distributions in data (in black) and PYTHIA (in blue) and SHERPA (in red) MC.

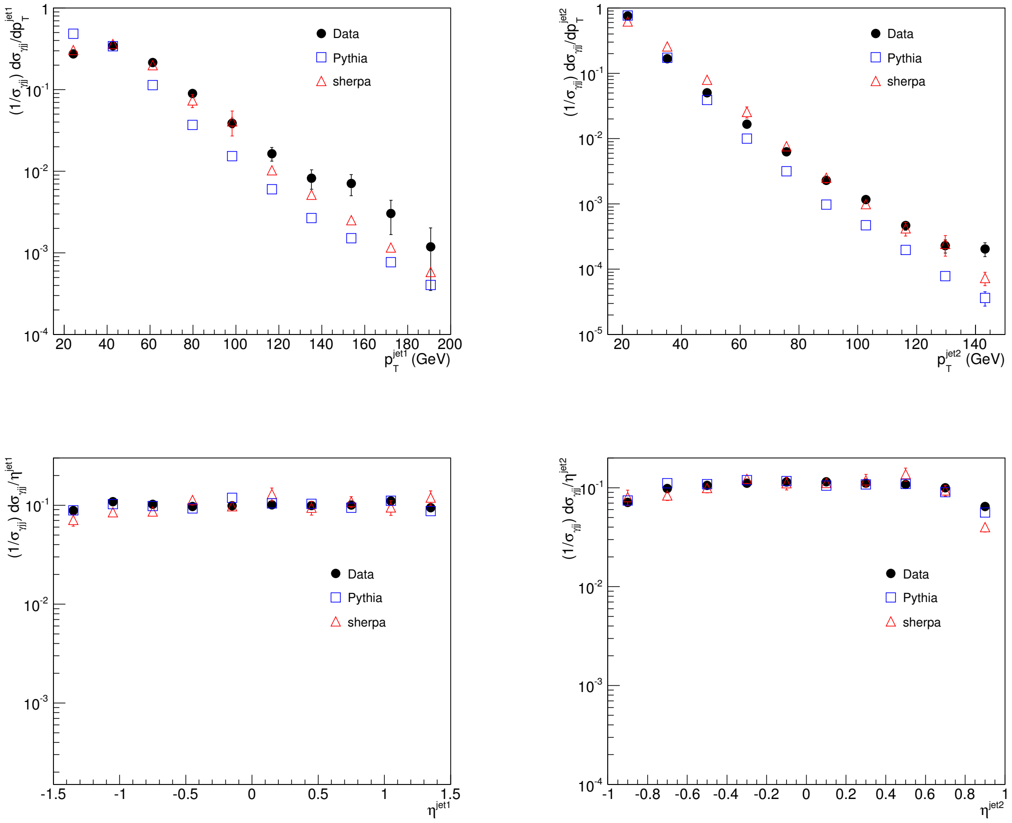

Figure 5.11: The normalized leading jet p_T and η (left), and sub leading jet p_T and η (right) distributions in data (in black) and PYTHIA (in blue) and SHERPA (in red) MC.

5.4.4.1 Photon acceptance

The photon acceptance A is calculated as

$$A = \frac{N_i^{\rm reco}}{N_i^{\rm part}}, \tag{5.6}$$

where $N_i^{\rm reco}$ and $N_i^{\rm part}$ are the numbers of events at the reconstruction and generator (true) level, respectively, in p_T^γ bin i. It takes into account the events lost due to geometric and basic kinematic selection criteria which are aimed at keeping just EM clusters reconstructed in the fiducial regions in η and ϕ of the calorimeter (i.e. to avoid inter-calorimeter section boundaries and edges) [50], and also "removes" events present at the reconstruction level but absent at the generator level.

The acceptance was calculated first from MC "γ +jet" events. Then additional correction due to MC/data difference were applied which are caused by a wrong simulation of the energy leakage nearby the calorimeter cracks in ϕ^{det} in CC region. Some part of photons can be also lost due to finite calorimeter acceptance in η_{det}. For this reason, a photon being produced with high physical rapidity and high z_{vtx} may not produce an EM cluster and one should correct for this effect.

The acceptance was calculated with respect to the photon selection criteria defined in equation 5.2. Only the fiducial areas of calorimeter were tested by these studies. By imposing, these requirements one can avoid the low efficiency calorimeter cells as well as the outer edges of the calorimeter walls (in η), where the reconstruction is mush less robust. These requirements give us much more stable and reliable energy measurement. The plot shown in Figure. 5.12 shows the size of the corrections for photon acceptances vs. p_T^γ in the central regions. The set of triangles on the plot (central photons) shows final acceptance with in "ϕ fiducial" requirement and contains 1.09 data/MC correction factor.

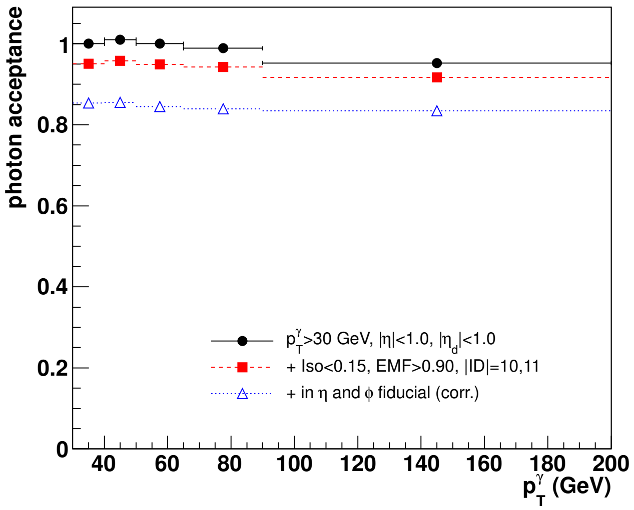

Figure 5.12: The photon acceptance as a function of direct photon p_T for the photons in the central region $|\eta| < 1.0$.

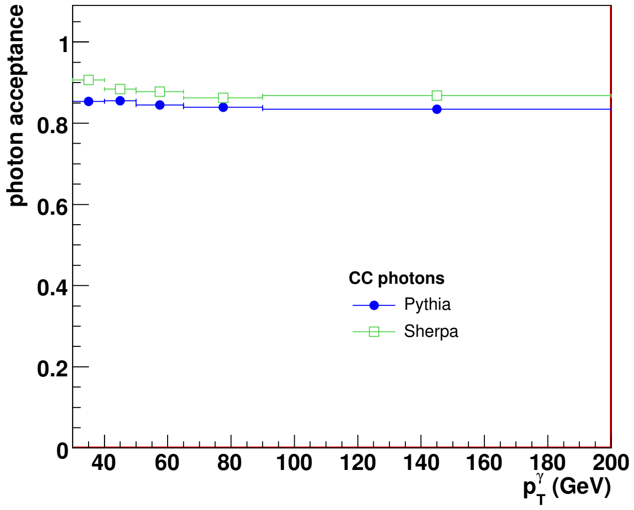

Figure 5.13: Comparison of photon acceptances in the PYTHIA and SHERPA event generators for the photons in the central region $|\eta| < 1.0$.

Figure. 5.13 compares photon acceptances calculated in PYTHIA and SHERPA event generators. The difference in two model is taken as systematic uncertainty for model dependence.

5.4.4.2 Jet acceptance

The jet acceptance was calculated according to Eq. (5.6) with respect to the event sample preselected with the photon selections of Eq. (5.2). and using following similar requirements at the generator and reconstruction levels:

$$\text{Generation level}: \ 2\text{b true jets with}\, p_T^{jet} > 15\,\text{GeV},\ |\eta| < 1.5;$$

$$\text{Reconstruction level}: 2\text{b reco jets with}\, p_T^{jet} > 15\,\text{GeV},\ |\eta| < 1.5. \tag{5.7}$$

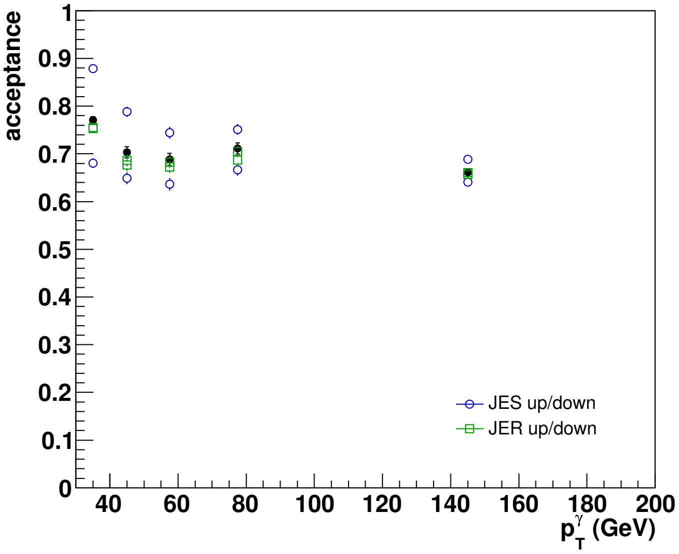

Figure 5.14: The jet acceptance with standard JES and jet p_T resolution acceptances as a function of direct photon p_T for the photons in the central region $|\eta| < 1.0$.

The reconstructed (raw) jet p_T was scaled with JES corrections and over-smeared to match the data. The combined photon and jets acceptance with respect to the p_T and rapidity selections varies between 66% and 77% in different p_T^γ bins. Figure 5.14 shows uncertainties related with standard JES and jet p_T resolution addition to the central corrections. The details of all the systematic uncertainties that go into the cross section due to acceptance calculation are described later in Section 5.6.

5.5 Theory Correction for Hadronization and MPI Effects

The theoretical cross sections (presented in section 5.7) use the jet algorithm running at the parton level. The photon isolation is also defined at the parton level.

To compare the theoretical predictions with our results they have to be corrected for the parton-to-hadrons fragmentation effect and the effect caused by the parton interactions in addition to the main hard scattering process (MPI effect). Fragmentation and MPI effects were estimated using PYTHIA 6.4 with interface to Run II cone DØ algorithm (cone R=0.5) and D0JetSim [90]. To have a better view of the tendencies, a lower p_T^γ bin, $25 - 30$ GeV was also added.

The correction were estimated in three stages:

a) Fragmentation effect (done without MPI):

Two separate calculations were done for jet algorithm working on the particle level and on the parton levels (MSTP(111) = 0 or 1). Then the cross section ratio with the particle to parton jets was calculated. The results are shown in Fig. 5.16 by full black circles. One can see that this correction depends on p_T^γ and for the first bin of our measurement (30–40) is about 9–10% and then decreasing with p_T^γ.

b) MPI effect.

This was done in two steps. First, without the particle level photon isolation cut $Iso(R = 0.4) < 2.5$ GeV and then with this cut. PYTHIA parameters for tune A set (with CTEQ5L PDFs) described in [91] were used. Then two separate calculations were done, one with multiple parton interactions switched on and one with off (MSTP(81)=0 and 1), and the cross section ratio of the 1st to 2nd was obtained. The results are shown in Figs. 5.17 by open blue squares. Due to additional contribution of energy to the jet cone, it becomes easier to pass the jet $p_T > 15$ GeV cut and thus the cross section increases (more at smaller p_T^γ).

Then the photon isolation requirement was added. Since it is the same ($Iso(R = 0.4) < 2.5$ GeV) for all p_T^γ bins and the additional parton interactions (in good approximation for the p_T^γ range considered) do not correlate with the main hard interaction, it decreased the cross section for all p_T^γ bins by about 5%. The effect of MPI events on the photon isolation is discussed in more details in [86]. In Fig. 5.15 (taken from [86], Sec IX) distributions of total p_T sum in the photon isolation cone ($R = 0.4$) are shown for the photon events simulated with PYTHIA in the four cases:

(i) without hadronization and MPI effects (but with ISR/FSR),

(ii) with hadronization, but without MPI,

(iii) with MPI Tune A and MPI Tune S0.

From analysis and comparison of those events one can conclude that

(i) additional parton interactions lead to a noticeable p_T increase in the isolation cone;

(ii) the change of shape is consistent between the two tunes considered (Tune A and S0), and

(iii) contribution from the hadronization effect is negligible as compared with MPI one.

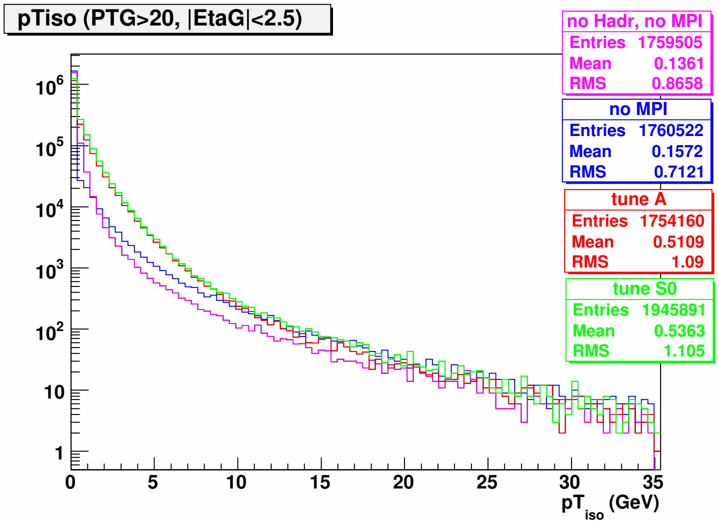

Figure 5.15: Total p_T sum in the photon isolation cone ($R = 0.4$) for the photon events (pT_{iso}) simulated with PYTHIA in the four cases: (1) without hadronization and MPI effects (but with ISR/FSR), (2) with hadronization, but without MPI; (3a) with MPI Tune A and (3b) with MPI Tune S0.

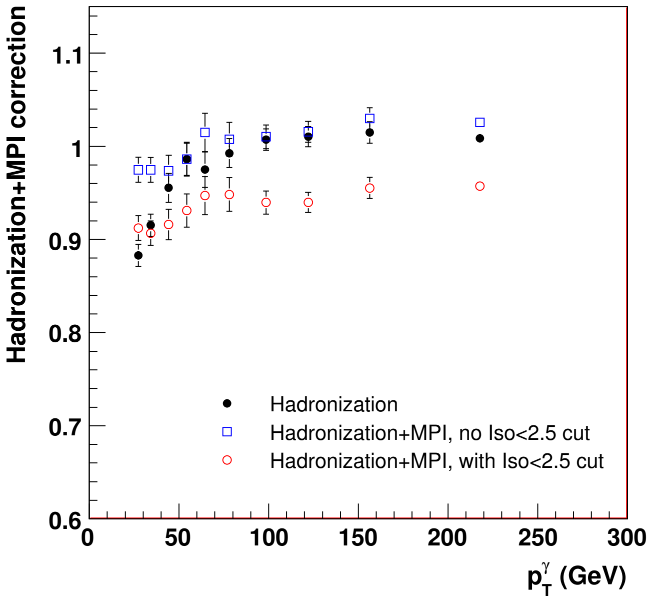

Figure 5.16: Theory correction factors due to the parton-to-hadrons fragmentation and MPI effects in $\gamma + b$ events with CC.

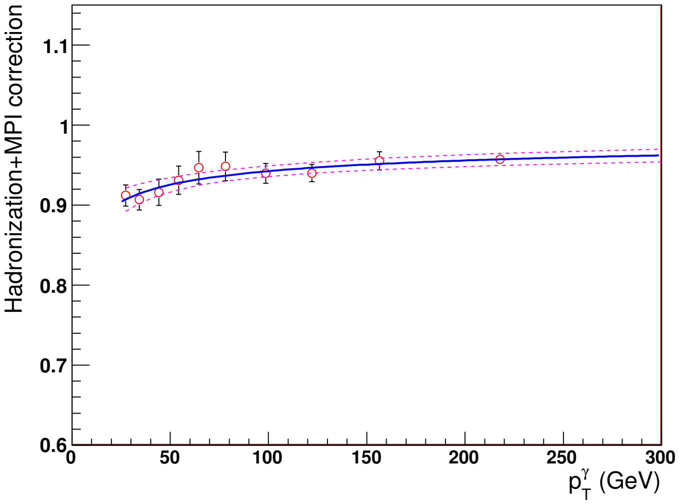

Figure 5.17: Fit to the final hadronization+MPI correction factors in $\gamma + b$ events with CC.

The final corrections, shown in Fig. 5.16 by open red circles, were fitted and also shown separately in Fig. 5.17. As we see, the theory predictions should be multiplied by $0.90 - 0.95$ with about $2 - 3\%$ uncertainty. Corrections for the CC and EC cross sections are close to each other within 1.5%.

5.6 Systematic Uncertainties

The sources of experimental systematic uncertainties (in %) for the measured $\gamma+2$ b-jet and $\gamma + b$- jet production cross section are shown in Tables 5.2 and 5.3. One can see that the largest uncertainty was caused by the 2 b-jets fractions and acceptances. The relative uncertainties of the estimated 2 b-jet fractions range from 5% to 14%, increasing at higher p_T^γ and are dominated by the limited data statistics. Also, the difference in the values of the fractions obtained from SHERPA and PYTHIA, $(2-4)\%$, was assigned as a systematic uncertainty on the background estimate.

p_T^γ bin (GeV)	Lumi	Accpt	ϵ_s^γ	γ-Purity	γ ES	TRF	b-Purity
30 – 40	6.1	+14.1/-11.9	3.0	5.1	5.8	5.6	5.2
40 – 50	6.1	+13.2/-9.7	3.0	4.3	4.0	5.5	6.0
50 – 65	6.1	+8.5/-7.5	3.0	3.1	4.0	5.4	7.2
65 – 90	6.1	+6.6/-6.3	3.0	3.1	2.8	5.0	8.0
90 –200	6.1	+4.3/-3.1	3.0	8.0	2.8	6.2	13.3

Table 5.2: Systematic uncertainties (in %) $\gamma + 2b$-jet cross section due to b-jet and γ fractions, TRF with taggability (TRF), γ energy scale (γ ES), γ selection efficiency, γ and jet acceptance (Accpt) and luminosity (Lumi). Central photons.

p_T^γ bin (GeV)	Lumi	Accpt	ϵ_s^γ	γ-Purity	γ ES	TRF	b-Purity
30 – 40	6.1	+4.3/-4.1	3.0	5.1	5.8	1.3	2.9
40 – 50	6.1	+6.1/-5.9	3.0	4.4	4.0	1.3	2.6
50 – 65	6.1	+1.8/-1.5	3.0	3.1	4.0	1.5	2.8
65 – 90	6.1	+1.8/-0.8	3.0	3.1	2.8	1.3	2.7
90 –200	6.1	+1.0/-0.6	3.0	8.1	2.8	3.3	5.3

Table 5.3: Systematic uncertainties (in %) $\gamma + b$-jet cross section due to b-jet and γ fractions, TRF with taggability (TRF), γ energy scale (γ ES), γ selection efficiency, γ and jet acceptance (Accpt) and luminosity (Lumi). Central photons.

p_T^γ bin (GeV)	JES“+”	JES“-”	JER“+”	JER“-”	Model	Total
30 – 40	13.9	11.7	2.3	2.0	1.0	+14.1/-11.9
40 – 50	12.1	7.7	2.4	3.8	3.2	+13.2/-9.7
50 – 65	8.2	7.5	2.2	0.8	0.4	+8.5/-7.5
65 – 90	5.7	6.2	3.3	1.0	0.3	+6.6/-6.3
90 – 200	4.2	3.1	0.6	0.2	0.4	+4.3/-3.1

Table 5.4: Jet acceptance uncertainties (in %) for the central photons.

Uncertainties on the acceptance was due to the jet energy scale [73], jet energy resolution. Additional uncertainty was assigned due to the difference between jet acceptances estimated from default SHERPA and reweighted SHERPA. A data like model was constructed by reweighting the photon p_T in SHERPA and the acceptances were recalculated. For this purpose, sub leading jet distribution was taken which has worst agreement with data as seen in Figure 5.10. The ratio of data to MC for sub leading jet p_T distribution was taken as reweight factor and was applied for each event. All the uncertainties related with the jet acceptance are summarized in Table 5.4. The relative systematic uncertainties on 2 b-jet selection were $(5-6)\%$, primarily due to uncertainties on the data-to-MC correction factors. Uncertainties of a smaller size were also caused by photon fractions. The main systematic uncertainty in the photon fractions was due to the fragmentation model implemented in PYTHIA [63]. This uncertainty was estimated by varying the production rate of π^0 and η mesons by $\pm 50\%$ with respect to their central values [92], and was found to be about 6% at $p_T^\gamma \approx 30$ GeV, and $\leq 3\%$ at $p_T^\gamma \gtrsim 70$ GeV. Then there were uncertainties due to photon selection (photon ID scale factors), luminosity and photon energy scale. The later is obtained by calculating the cross section with uncertainties on the photon energy scale varied up and down. Uncertainties of other sources (trigger efficiency, PV selection, missing E_T, $\Delta R(\gamma, jet)$) are $\lesssim 1\%$ each and, being negligibly small, are not shown in the tables. The systematic uncertainties on the ratio vary within $(11-15)\%$, being largest at high p_T^γ. The major sources of systematic uncertainties were attributed to the jet acceptances and the estimation of b-jet and 2 b-jet fractions obtained from the template fits to the data and are summarized in Table 5.5.

p_T^γ bin (GeV)	A_{bb}	$b\bar{b}$-Purity	b-Purity	δ_{stat}	δ_{total}
30 – 40	+9.9/-8.2	5.2	2.9	2.2	14.3
40 – 50	+9.8/-6.7	6.0	2.6	2.5	14.1
50 – 65	+6.9/-6.2	7.2	2.8	2.8	15.1
65 – 90	+4.8/-6.0	8.0	2.7	3.4	13.1
90 –200	+3.4/-2.7	13.3	5.3	3.4	18.2

Table 5.5: Systematic uncertainty for the ratio $\sigma(\gamma + 2\ b)/\sigma(\gamma + b)$ due to jet acceptance $(A_{\text{bb}}, A_{\text{b}})$, and found $b\bar{b}$ and b jet fractions.

5.7 Results

5.7.1 $\gamma + 2b$-jet cross-section

Next acceptance ($\mathcal{A}$), luminosity ($\mathcal{L}$), trigger efficiency (ϵ_t), photon and jet selection efficiencies ($\epsilon_s^\gamma, \epsilon_s^{\text{jet}}$), primary vertex efficiency (ϵ_{pv}), b-tagging efficiency ($\epsilon_{bb}^{\text{jet}}$), E_T^{miss} efficiency ($\epsilon_{E_T^{\text{miss}}}$), photon and b-jet purities ($\mathcal{P}_\gamma, \mathcal{P}_b$) are combined to calculate the differential cross sections using Equation (5.1). The total number of events, γ+2b-jet candidates, remaining after application of all the selection criteria with the central photons were 3816. These events were used to calculate the cross sections in 5 p_T^γ bins, 30–200 GeV, with the central photons.

The results of the measurements are shown in Table 5.6 as well as in Figure. 5.18. The cross sections are shown as a function of p_T^γ with the full experimental errors (systematic $\oplus$ statistical). As we see that in the range of $30 < p_T^\gamma < 200$ GeV the $\gamma + b$ cross sections with central photons fall by almost four orders of magnitude. Statistical uncertainty due to data statistics vary from 4.3% in the first p_T^γ bin to 7–9% in the last bin, the remaining fraction of the statistical uncertainty is due to MC statistics used to calculate photon and jet acceptance and efficiencies. The systematic uncertainties vary within 17–21% depending on the p_T^γ bin. The main two sources of systematic uncertainties were caused by the b-jet fraction and b-jet acceptances. (as given in Section 5.6).

The behaviour of the theoretical scale uncertainties is shown in Figure. 5.19. They are obtained by simultaneous variation of all the three scales by a factor of two and four, up and down, $\mu_{R,F,f} = 0.5p_T^\gamma$, $\mu_{R,F,f} = 2p_T^\gamma$, $\mu_{R,F,f} = 0.25p_T^\gamma$, and $\mu_{R,F,f} = 4p_T^\gamma$. Comparison to PYTHIA predictions and SHERPA predictions is also shown.

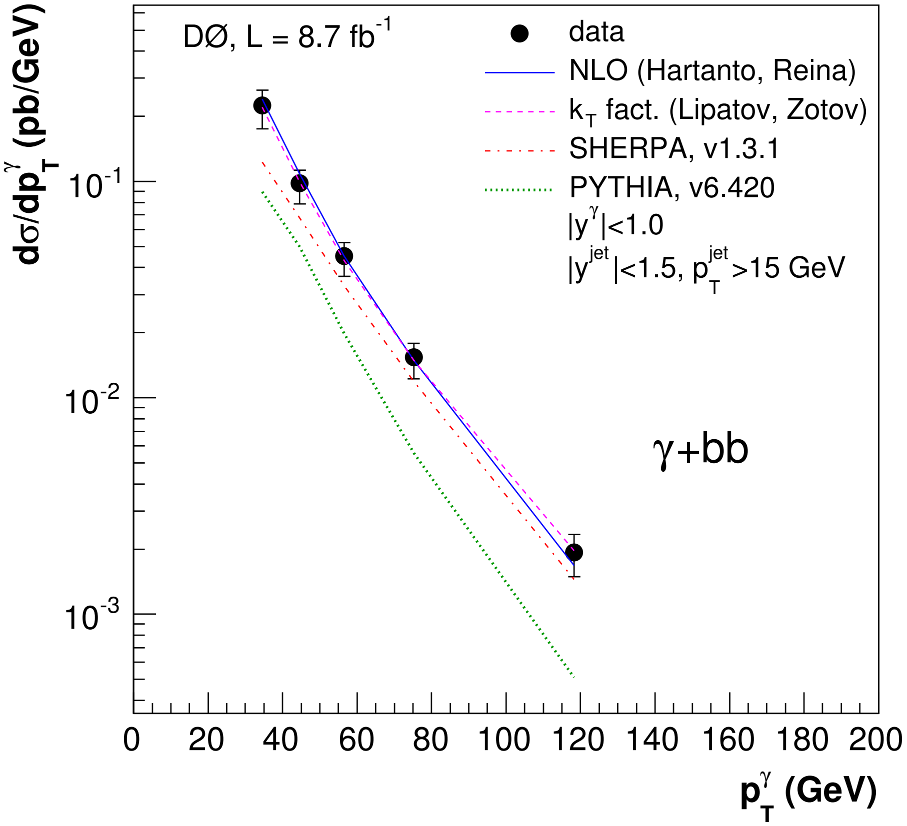

Figure 5.18: The $\gamma + 2b$-jet cross sections as a function of p_T^γ with central ($|\eta| < 1.0$, full circles). The uncertainties on the points in data are the full experimental uncertainties. The lines here are predictions done by NLO(voilet solid line with uncertainties from scale dependencies), kT Factorization (red dashed line), SHERPA MC (blue dashed line) and PYTHIA MC (green dashed line).

p_T^γ bin (GeV)	$\langle p_T^\gamma \rangle$ (GeV)	$\mathrm{d}\sigma/\mathrm{d}p_T^\gamma$ (pb/GeV)							
		Data	$\delta_{\mathrm{stat}}(\%)$	$\delta_{\mathrm{syst}}(\%)$	$\delta_{\mathrm{tot}}(\%)$	NLO	k_T fact.	PYTHIA	SHERPA
30 – 40	34.5	2.24×10^{-1}	4.3	$+19/-17$	$+19/-18$	2.39×10^{-1}	2.20×10^{-1}	8.96×10^{-2}	1.23×10^{-1}
40 – 50	44.6	9.80×10^{-2}	5.4	$+18/-15$	$+19/-16$	1.08×10^{-1}	9.96×10^{-2}	4.99×10^{-2}	6.79×10^{-2}
50 – 65	56.6	4.52×10^{-2}	6.2	$+15/-14$	$+16/-16$	4.51×10^{-2}	4.31×10^{-2}	1.99×10^{-2}	3.29×10^{-2}
65 – 90	75.2	1.54×10^{-2}	7.2	$+14/-14$	$+16/-16$	1.49×10^{-2}	1.48×10^{-2}	5.57×10^{-3}	1.19×10^{-2}
90 – 200	118.3	1.93×10^{-3}	9.1	$+19/-18$	$+21/-21$	1.67×10^{-3}	1.96×10^{-3}	5.12×10^{-4}	1.45×10^{-3}

Table 5.6: The differential $\gamma + 2$ b-jet production cross sections $\mathrm{d}\sigma/\mathrm{d}p_T^\gamma$ in bins of p_T^γ for $|\eta^\gamma| < 1.0$, $p_T^{\mathrm{jet}} > 15$ GeV and $|y^{\mathrm{jet}}| < 1.5$ together with statistical uncertainties (δ_{stat}), total systematic uncertainties (δ_{syst}) and total uncertainties (δ_{tot}) which are obtained by adding δ_{stat} and δ_{syst} in quadrature. The last four columns show theoretical predictions obtained with NLO QCD, k_T factorization, and with the PYTHIA and the SHERPA event generators.

The NLO predictions are based on Fixed-flavor scheme or four-flavor-number scheme (4FNS). The b quark is treated as massive and no b-quark parton density is assumed in the initial state. The complete structure of calculation and details of the techniques used in its realization are published [29].

The prediction based on kT-factorization [93] approach contains additional contributions to the cross sections due to resummation of the gluon radiation diagrams with k_T^2 above a scale μ^2,O(1 GeV), where kT denotes the transverse momentum of the radiated gluon. Apart from this resummation, the non-vanishing transverse momentum distribution of the colliding particles are taken into account. These effects lead to a broadening of the photon transverse momentum distribution in this approach. The scale uncertainties on these predictions vary from 31% (-28%) at $30 < p_T^\gamma < 40 GeV$ to about 5% (-14%) for the central photons and 26% (-13%) for the forward photons in the last p_T^γ bins. The predictions from PYTHIA MC event generator with CTEQ6.1L PDF set includes only $2 \rightarrow 2$ matrix elements (ME) with $gb \rightarrow \gamma b$ and $q\bar{q} \rightarrow b\bar{b}$ scatterings (defined at LO) and, with $g \rightarrow b\bar{b}$ splitting in the parton shower (PS). The SHERPA predictions with CTEQ6.6M PDF set includes all the MEs with one photon and up to three jets, with at least one b-jet in our kinematic region. In particular, it accounts for an additional hard jet that accompanies the photon associated with a $b\bar{b}$ pair. All the theoretical predictions are obtained including the isolation requirement on the photons $E_T^{iso} < 2.5$ GeV at the particle level. The ratio of the measured $\gamma + 2b$-jet cross sections to the theoretical predictions are presented in Figure. 5.19.

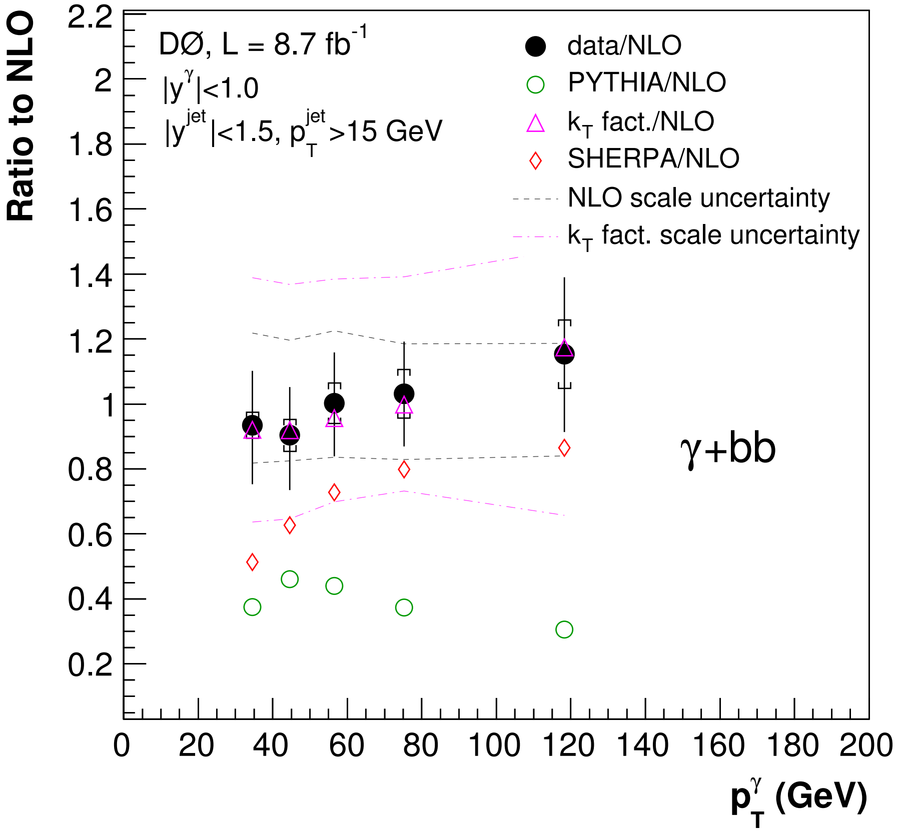

Figure 5.19: The $\gamma + 2b$-jet cross section ratio of data to theory as a function of p_T^γ with photons in the central rapidity region, $|\eta| < 1.0$. This includes the theoretical scale uncertainties. The uncertainties on the points in data include both statistical (inner line) and the full uncertainties (the entire line).

5.7.2 $\gamma + b$-jet cross-section

To calculate the rate of $\gamma + 2b$-jet events in $\gamma + b$-jet events the ratio of cross sections of $\gamma + 2b$-jet to $\gamma + b$-jet was taken. So the $\gamma + b$-jet cross sections were reproduced in our pT bins. Following the same procedure as for $\gamma + 2b$-jet and combining acceptance ($\mathcal{A}$), luminosity ($\mathcal{L}$), trigger efficiency (ϵ_t), photon and jet selection efficiencies ($\epsilon_s^\gamma, \epsilon_s^{\text{jet}}$), primary vertex efficiency (ϵ_{pv}), b-tagging efficiency (ϵ_b^{jet}), E_T^{miss} efficiency ($\epsilon_{E_T^{\text{miss}}}$), photon and b-jet purities ($\mathcal{P}_\gamma, \mathcal{P}_b$) , the differential cross sections were evaluated.

$$\frac{\mathrm{d}\sigma}{\mathrm{d}p_T^\gamma} = \frac{N_{\mathrm{Events}}\ \mathcal{P}_b\ \mathcal{P}_\gamma}{\Delta p_T^\gamma\ \epsilon_t\ \epsilon_s^\gamma\ \epsilon_s^{\mathrm{jet}}\ \epsilon_{pv}\ \epsilon_b^{\mathrm{jet}}\ \epsilon_{E_T^{\mathrm{miss}}}\ \mathcal{L}\ \mathcal{A}}. \tag{5.8}$$

The results of the measurements are shown in Figure. 5.20 as well as in Table 5.7 as a function of p_T^γ with the full experimental errors (systematic $\oplus$ statistical).

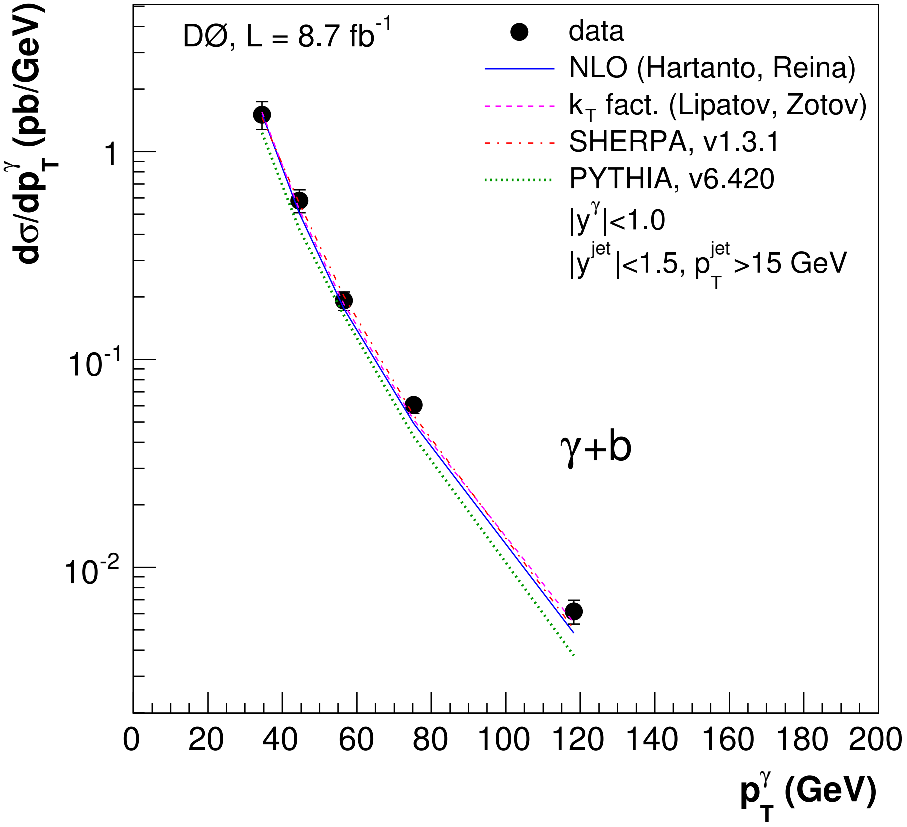

Figure 5.20: The $\gamma + b$-jet cross sections as a function of p_T^γ with central ($|\eta| < 1.0$, full circles). The uncertainties on the points in data are the full experimental uncertainties. The lines here are predictions done by NLO(violet solid line with uncertainties from scale dependencies), SHERPA MC (blue dashed line) and PYTHIA MC (green dashed line).

p_T^γ bin (GeV)	$\langle p_T^\gamma \rangle$ (GeV)	$\mathrm{d}\sigma/\mathrm{d}p_T^\gamma$ (pb/GeV)							
		Data	$\delta_{\mathrm{stat}}(\%)$	$\delta_{\mathrm{syst}}(\%)$	$\delta_{\mathrm{tot}}(\%)$	NLO	k_{T} fact.	PYTHIA	SHERPA
30 – 40	34.5	1.51	2.3	12	12	1.52	1.69	1.23	1.46
40 – 50	44.6	5.83×10^{-1}	2.4	11	12	5.06×10^{-1}	5.70×10^{-1}	4.23×10^{-1}	5.65×10^{-1}
50 – 65	56.6	1.92×10^{-1}	2.8	9	10	1.75×10^{-1}	1.98×10^{-1}	1.63×10^{-1}	2.02×10^{-1}
65 – 90	75.2	6.06×10^{-2}	3.3	9	9	4.93×10^{-2}	5.43×10^{-2}	4.27×10^{-2}	5.41×10^{-2}
90 – 200	118.3	6.15×10^{-3}	3.3	13	13	4.83×10^{-3}	5.68×10^{-3}	3.76×10^{-3}	5.05×10^{-3}

Table 5.7: The differential $\gamma + b$-jet production cross sections $\mathrm{d}\sigma/\mathrm{d}p_T^\gamma$ in bins of p_T^γ for $|\eta^\gamma| < 1.0$, $p_T^{\mathrm{jet}} > 15$ GeV and $|y^{\mathrm{jet}}| < 1.5$ together with statistical uncertainties (δ_{stat}), total systematic uncertainties (δ_{syst}), and total uncertainties (δ_{tot}) that are obtained by adding δ_{stat} and δ_{syst} in quadrature. The last four columns show theoretical predictions obtained with NLO QCD, k_{T}-factorization, and with the PYTHIA and the SHERPA event generators.

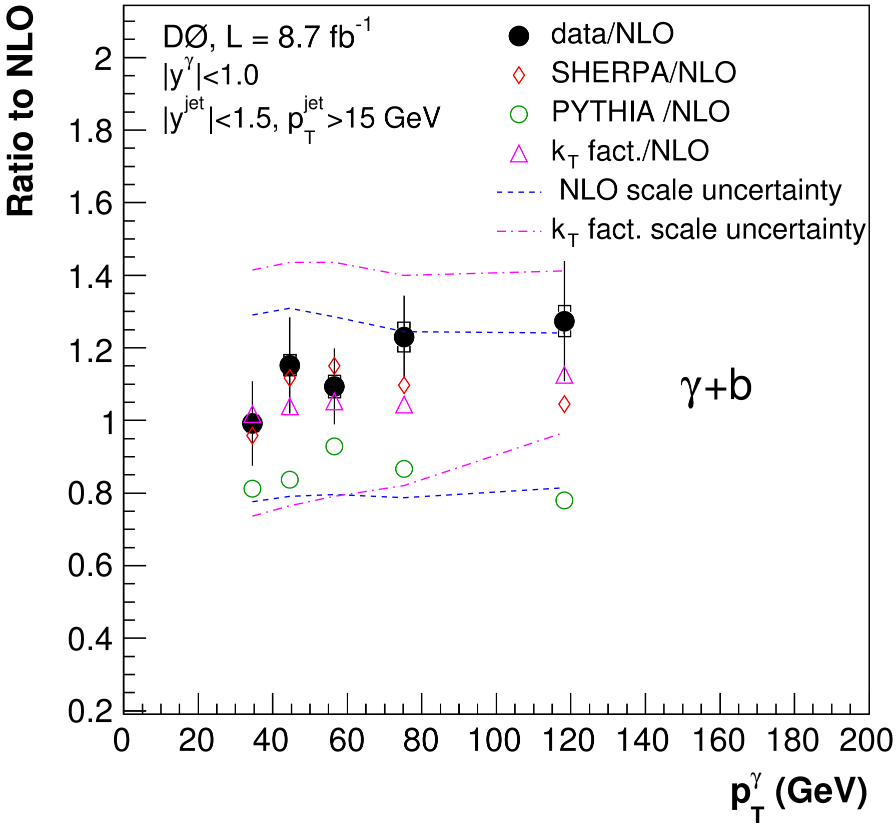

Figure 5.21: The $\gamma + b$-jet cross section ratio of data to theory as a function of p_T^{γ} with photons in the central rapidity region, $|\eta| < 1.0$. This includes the theoretical scale uncertainties. The uncertainties on the points in data include both statistical (inner line) and the full uncertainties (the entire line).

5.8 Ratio $\sigma(\gamma + 2\ b - \text{jet})/\sigma(\gamma + b - \text{jet})$

The ratio of $\gamma + 2b$-jet to $\gamma + b$-jet was calculated using following form:

$$\frac{\sigma(\gamma + 2b)}{\sigma(\gamma + b)} = \frac{N_{\gamma\,+\,b\bar{b}\text{ Events}}\ \mathcal{P}_{bb}\ \mathcal{A}_{\text{bb}}}{N_{\gamma\,+\,b\text{ Events}}\ \mathcal{P}_{b}\ \epsilon_b^{\text{jet2}}\ \mathcal{A}_{\text{b}}}. \tag{5.9}$$

The results of the measurements are shown in Figure 5.22 as well as in Table 5.8 as a function of p_T^{γ} with the full experimental errors (systematic $\oplus$ statistical).

The several systematic uncertainties cancelled out in the ratio measurement. The sources of systematic errors are shown in Table 5.5. The systematic errors from photon selection and leading jet ID (TRF SF) cancelled out in ratio as we see from Equation 5.9.

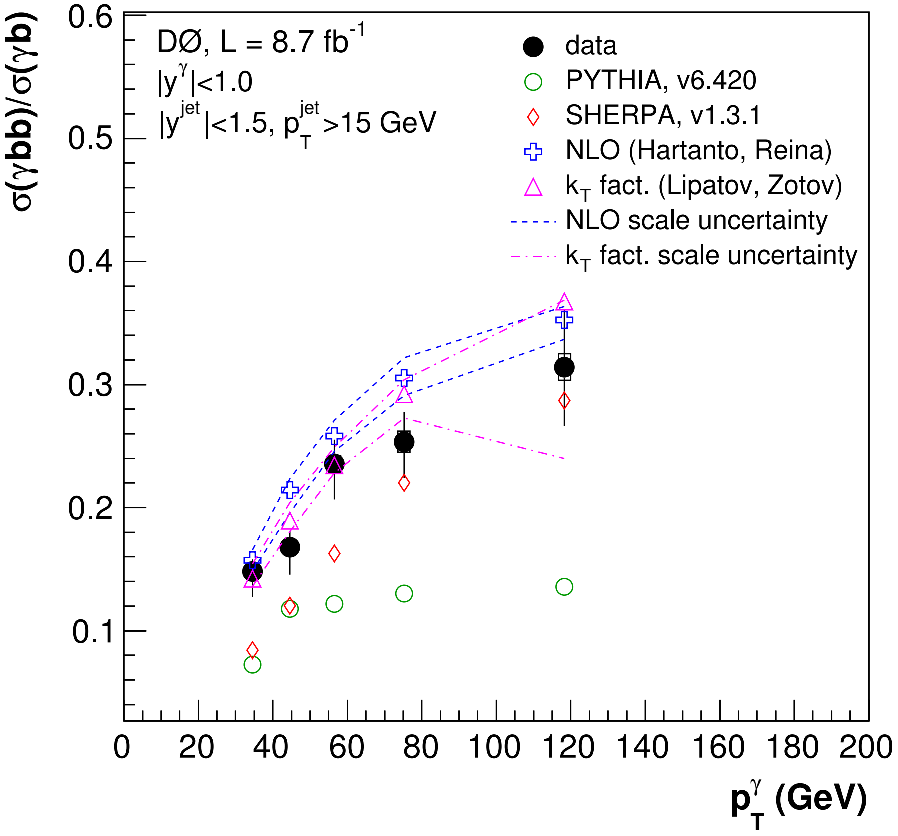

Figure 5.22: The ratio of $\gamma + 2b$-jet cross section to $\gamma + b$-jet as a function of p_T^{γ} with photons in the central rapidity region, $|\eta| < 1.0$ and its comparison with theory. The uncertainties on the points in data include both statistical (inner line) and the full uncertainties (the entire line).

p_T^γ bin (GeV)	$\langle p_T^\gamma \rangle$ (GeV)	$\sigma(\gamma+2\ b)/\sigma(\gamma+b)$							
		Data	$\delta_{\text{stat}}(\%)$	$\delta_{\text{syst}}(\%)$	$\delta_{\text{tot}}(\%)$	NLO	k_{T} fact.	PYTHIA	SHERPA
30 – 40	34.5	1.48×10^{-1}	2.3	$+14/-6$	$+14/-6$	1.58×10^{-1}	1.42×10^{-1}	7.25×10^{-2}	8.42×10^{-2}
40 – 50	44.6	1.68×10^{-1}	2.5	$+13/-7$	$+13/-8$	2.04×10^{-1}	1.89×10^{-1}	1.18×10^{-1}	1.20×10^{-1}
50 – 65	56.6	2.36×10^{-1}	2.8	$+12/-8$	$+12/-8$	2.59×10^{-1}	2.34×10^{-1}	$1.22\ \times10^{-1}$	1.63×10^{-1}
65 – 90	75.2	2.54×10^{-1}	3.3	$+11/-8$	$+12/-10$	3.05×10^{-1}	2.92×10^{-1}	1.30×10^{-1}	2.20×10^{-1}
90 – 200	118.3	3.14×10^{-1}	3.4	$+15/-14$	+15/-15	3.52×10^{-1}	3.67×10^{-1}	1.36×10^{-1}	2.87×10^{-1}

Table 5.8: The $\sigma(\gamma+2\ b\text{-jet})/\sigma(\gamma+b\text{-jet})$ cross section ratio in bins of p_T^γ for $|\eta^\gamma| < 1.0$, $p_T^{\text{jet}} > 15$ GeV and $|y^{\text{jet}}|<1.5$ together with statistical uncertainties (δ_{stat}), total systematic uncertainties (δ_{syst}) and total uncertainties (δ_{tot}) which are obtained by adding δ_{stat} and δ_{syst} in quadrature. The last four columns show theoretical predictions obtained with NLO QCD, k_{T} factorization, and with the PYTHIA and the SHERPA event generators.

Chapter 6

Measurement of Ratio $\sigma(p\bar{p} \rightarrow Z + 2\ b\ \text{jets})/\sigma(p\bar{p} \rightarrow Z + 2\ \text{jets})$

The ratio of cross sections for the inclusive production of Z+2 b-jet events to Z+2-jet events was also measured using the same analysis techniques as used in photon plus heavy flavour jets. The measurement is parallel to the $\gamma + 2b$-jet production cross section, taking advantage of the b-tagging technique and flavour fraction extraction developed for the study of photon plus heavy flavour jets . This chapter describes the selection for $Z + 2$ b-jet events and $Z + 2$-jet events, their corresponding efficiencies, background estimations and finally combining all the ingredients to give us ratio measurement. The results were compared to the theoretical predictions. Systematic uncertainties related to the measurement are discussed in details.

6.1 Event Selection

The analysis preselection requires a reconstructed Z boson candidate decaying as $Z \rightarrow \mu\mu$ or $Z \rightarrow ee$ plus at least two hadronic jets. The pre-selections on muons for reconstruction of Z in dimuon channel, electrons for reconstruction of Z in dielectron channel and jets are outlined in the following sub-sections. Although the reconstruction of Z is different, the jet selection and b-tagging performed are the same in the $Z \to \mu\mu$ and $Z \to ee$ channels. The following selection cuts are used in the present analysis.

6.1.1 Primary Vertex

A primary vertex (PV) is required with at least three associated tracks and reconstructed z-position within 60 cm of the center of the detector ($z = 0$) along the direction of the beam.

6.1.2 Muons

Events are required to have at least two muons as defined by the standard MuonSelector in CAFé [94] (Tag Nv04-04-00).

- $p_T > 15$ GeV
- Loose muon ID requirements
- A matched central track
- A distance of closest approach $d < 0.004$ cm for tracks with SMT hits, and $d < 0.2$ cm for tracks without any SMT hits
- $|\eta_{det}| < 2.0$

The muon p_T in data and MC is corrected using the primary vertex information for each event if the muon track has no associated SMT hits. The η_{det} is the pseudorapidity η at which the particle enters the detector used to identify it.

6.1.2.1 Reconstructed $Z \to \mu\mu$ boson

A good Z candidate is required in each event, reconstructed from a pair of selected muons.

- $70 < M_{\mu\mu} < 110$ GeV
- pseudo-acolinearity > 0.05 (anti-cosmic)[1]
- Muons with opposite sign charge
- *product scaled isolation* $I(\mu_1)I(\mu_2) < 0.03$ (for dimuon only)

The product scaled isolation variable is the product of the scaled isolation variables (equation. 6.1) for each of the two muons which form the Z candidate. The scaled isolation variable $I(\mu_i)$ for muon i is:

$$I(\mu_i) = \frac{E_T^{cal}(0.1 - 0.4) + p_T^{trk}(0.5)}{p_T^i} \tag{6.1}$$

where $E_T^{cal}(0.1 - 0.4)$ is the calorimeter E_T inside a hollow cone of $0.1 < \Delta R < 0.4$ around the muon; $p_T^{trk}(0.5)$ is the vector sum of the transverse momenta of all tracks in a cone $\Delta R < 0.5$ around the muon; and p_T^i is the transverse momentum of the muon.

6.1.3 Electrons

The dielectron channel contains events where the two electrons are reconstructed either in the central cryostat (CC: $|\eta_{det}| < 1.1$) or in the endcap cryostat (EC: $1.5 < |\eta_{det}| < 2.5$) region of the calorimeter. The electron candidates with $p_T > 15$ GeV are considered. Electrons are required to pass the standard ElectronSelector in caf_util (Np21-br-112) using selection criteria defined in the emid_cuts package. The chosen criteria maintain the highest efficiency for signal for a manageable multijet background. For Run IIb, each electron must pass Loose version 11 quality:

- Isolated EM cluster $f_{iso} < 0.1$,

---

[1] The pseudo-acolinearity between two directions is calculated by the ZmumuSelector as$(\pi - \Delta(\phi 1, \phi 2)) + |(\pi - (\theta 1 + \theta 2))|$. By construction it is small when directions are colinear.

- Energy fraction in EM calorimeter $f_{EM} > 0.95$,
- Shower shape cut: HMx7 < 35 in CC, or HMx8 < 20 in EC;
- IsoHC4$<$ 3 in CC, or IsoHC4 < 2 in EC;
- NNout7$>$ 0.2 in CC, or NNout3 > 0.4 in EC;
- TrkMatchChi2$>$ 0.001 or EMHits_e_f$>$ 0.4 in CC,

The `HMx<N>` are H-matrix calorimeter shower shape variables. The IsoHC4 is a track isolation variable. The `NNout<N>` are outputs of neural-networks with `<N>` input variables including the energy deposited and number of hit cells in the first EM layer, the track isolation and energy deposited in the central preshower detector.

6.1.3.1 Reconstructed $Z \to ee$ boson

A good Z candidate is required in each event, reconstructed from a pair of selected electrons, with invariant mass $70 < M_{ee} < 110$ GeV.

6.1.4 Jets

Jets reconstructed using the Run 2 cone algorithm with $\Delta\mathrm{R} < 0.5$ are called JCCB jets. At least two 'good' JCCB jets are required in each event, satisfying the following requirements:

- *corrected* $p_T > 20$ GeV
- $|\eta| < 2.5$
- all jets must have vertex confirmation

Jet energies are corrected using the standard jet energy scale (JES) corrections. In order to suppress additional jets originating from minimum-bias secondary interactions, the jets used in Run IIb are required to originate from the primary vertex. The vertex confirmation requires that at least two tracks associated with the jet are matched to the primary vertex. For dielectron and dimuon events, all jets were required to be isolated from each electron and muon by $\Delta\mathcal{R} > 0.5$. A missing $E_T^{miss} < 60$ cut was applied to all events to reduce the potential background from top-pair events.

6.1.5 *b*-Tagging

Taggability criteria were also applied to ensure that the jet has sufficient information to be classified HF candidate. For this, the jet was required to have at least two associated tracks with $p_T > 0.5$ GeV and the track leading in p_T must have $p_T > 1.0$ GeV, and each track must have at least one SMT hit.

Light jets were suppressed using a dedicated HF tagging algorithm as used in photon plus heavy flavour jets. In this analysis, at least two of the jets were required to have an $\mathrm{MVA_{bl}}$ value greater than 0.15 which corresponds to the MEDIUM operating point.

In order to select $Z + 2$ b-jet events, the jets were b-tagged using the package *btags_cert*. The tagging was applied *after* the JetSSR processor in MC so that the jet $p_T > 15$ GeV cut required for taggability is applied to the smeared jet p_T. Taggability was applied directly to both data and MC after vertex confirmation in Run IIb. Since the taggability rates measured in data and MC disagree, corrections were applied to the MC to bring them into agreement. For the present analysis direct tagging was applied on the jets and data to MC scale factors were used as provided by the b-id group. The MC samples were corrected to account for some detector effects not adequately modeled by the simulation. Many of the corrections are integrated with the vjets_cafe framework. These corrections were done in previous measurement of the ratio of inclusive cross sections $\sigma(p\bar{p} \to Z + b)/\sigma(p\bar{p} \to Z + j)$ and can be found documented in Ref [95].

6.2 Z+jet Selection

Z boson candidates were reconstructed and identified through pairs of isolated, high p_T electrons or muons with dilepton invariant mass, $70 < M_{ll} < 110$ GeV, near the Z boson mass (M_Z) of 91.2 GeV. The Z+jet sample was then selected by requiring the presence of at least two reconstructed hadronic jets with $|\eta| < 2.5$, with the leading jet of $p_T > 20$ GeV. Table 6.1 shows the number of events for the data, various background components, the expected Z+jet events at the preselection level (events with Z boson associated with at least two jets) for both dimuon and dielectron channels.

Sample	Dimuon	Dielectron
data	10801	10149
$Z + 2j$	8490	7490
$Z + 2b$	173	166
$Z + 2c$	277	257
Multijet	36	912
ZZ	88	85
WZ	92	84
WW	6	5
$t\bar{t}$	35	32

Table 6.1: The data, backgrounds, and expected Z+jets events are listed in the preselected event sample.

6.2.1 Dimuon Channel

Some of the kinematic distributions for the Z candidates in the inclusive sample and $Z+ \geq 2$ before any b-tagging are shown here (Figures. 6.1 - 6.6). The errors are due to the statistics in the MC samples, and are not at all correlated to the uncertainty of their cross sections.

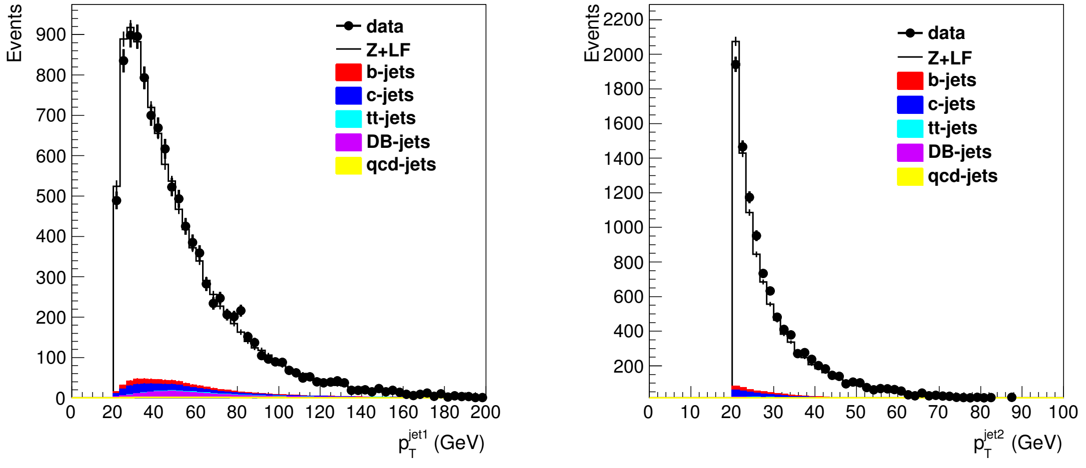

Figure 6.1: The leading and sub leading jet P_T spectrum for data and background in $Z+\geq 2$ jets sample before any b-tagging is applied.

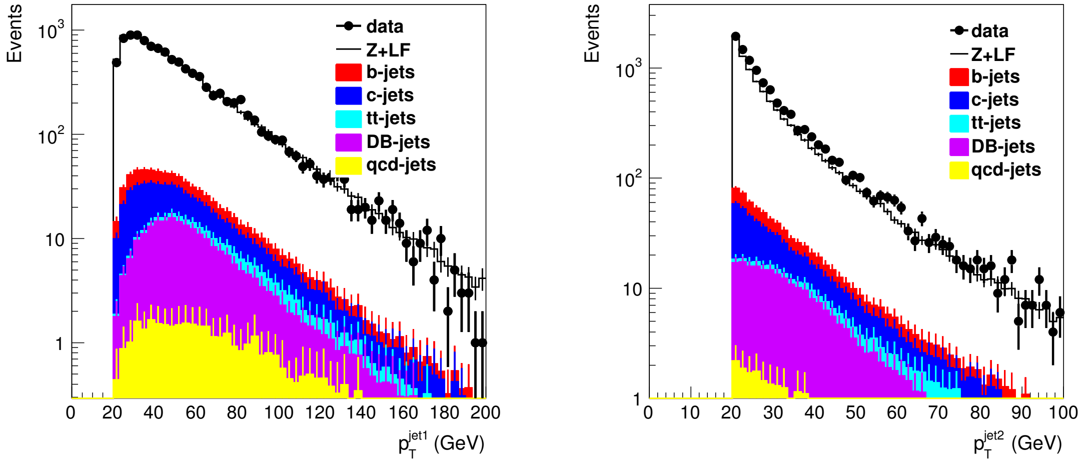

Figure 6.2: The leading and sub leading jet P_T spectrum for data and background in $Z+\geq 2$ jets sample before any b-tagging is applied, in log scale.

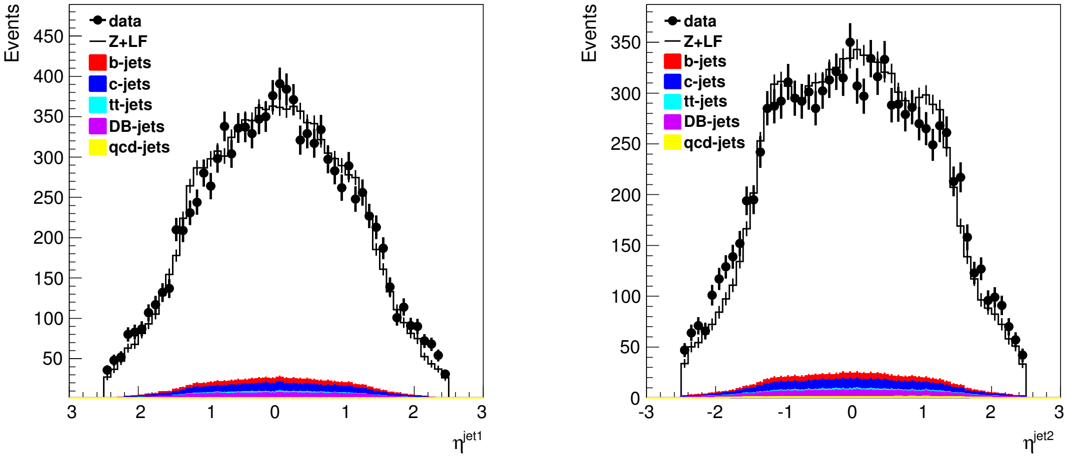

Figure 6.3: The leading and sub leading jet η spectrum for data and background in $Z+\geq 2$ jets sample before any b-tagging is applied.

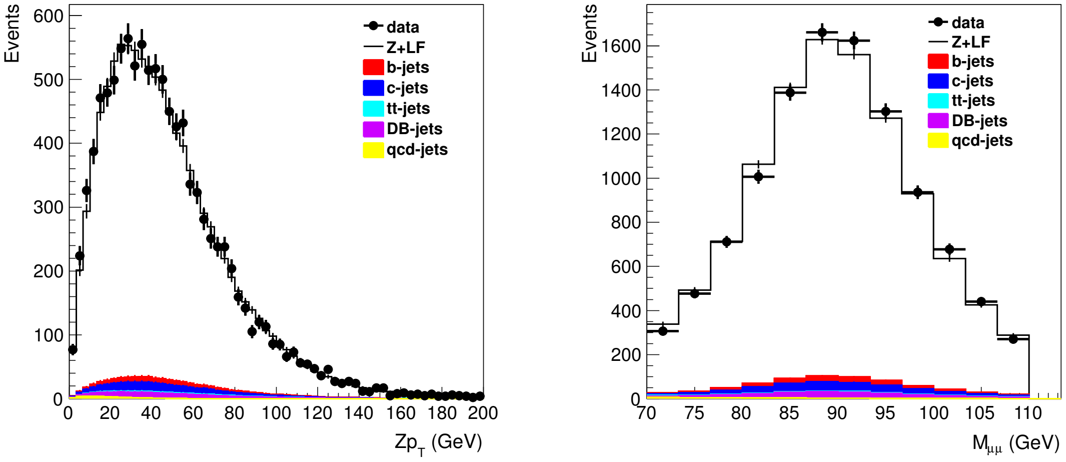

Figure 6.4: The Z P_T spectrum and invariant dimuon mass for data and background.

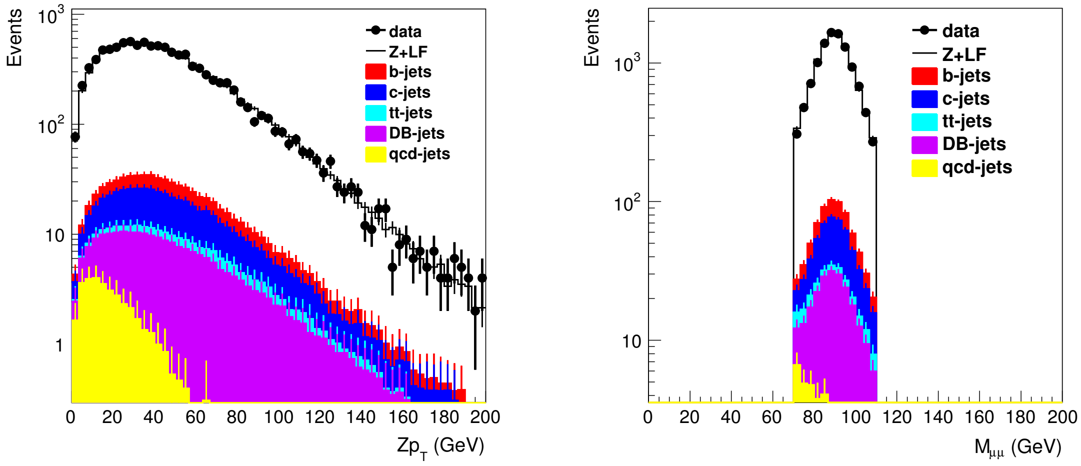

Figure 6.5: The Z P_T spectrum for data and background, in log scale.

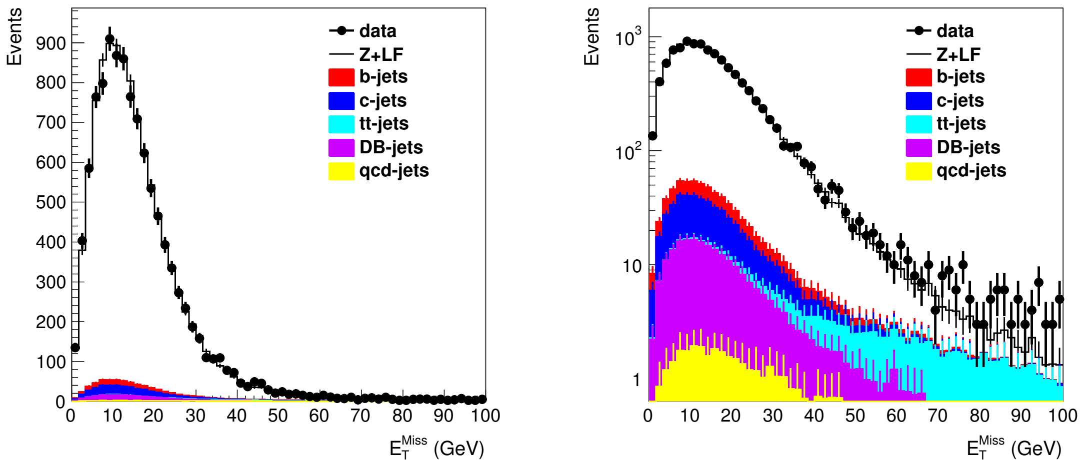

Figure 6.6: The Missing E_T spectrum for data and background and in log scale on right.

6.2.2 Dielectron Channel

Here are the kinematic distributions for the $Z \rightarrow ee$ candidates in the inclusive sample and $Z+ \geq 2$ before any b-tagging are shown here (figs. 6.7 - 6.12).

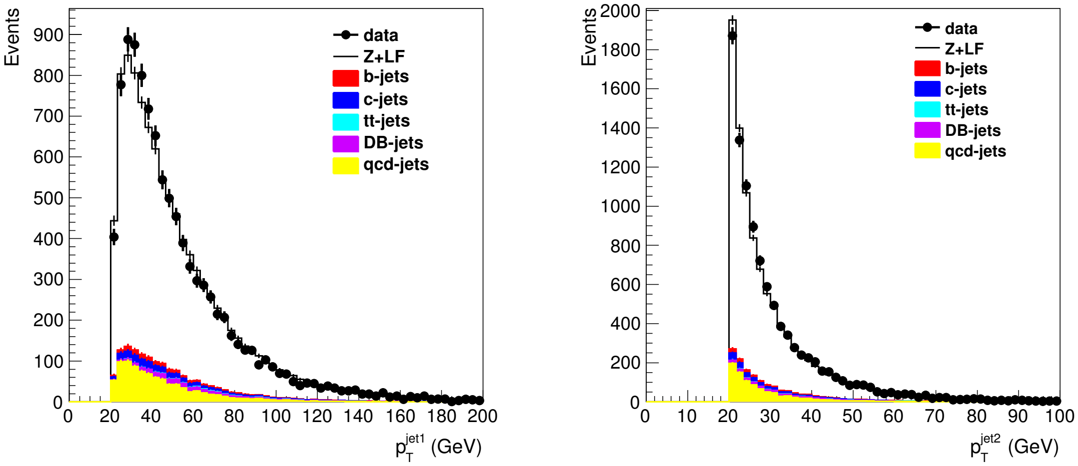

Figure 6.7: The leading and sub leading jet P_T spectrum for data and background in $Z+\geq 2$ jets sample before any b-tagging is applied.

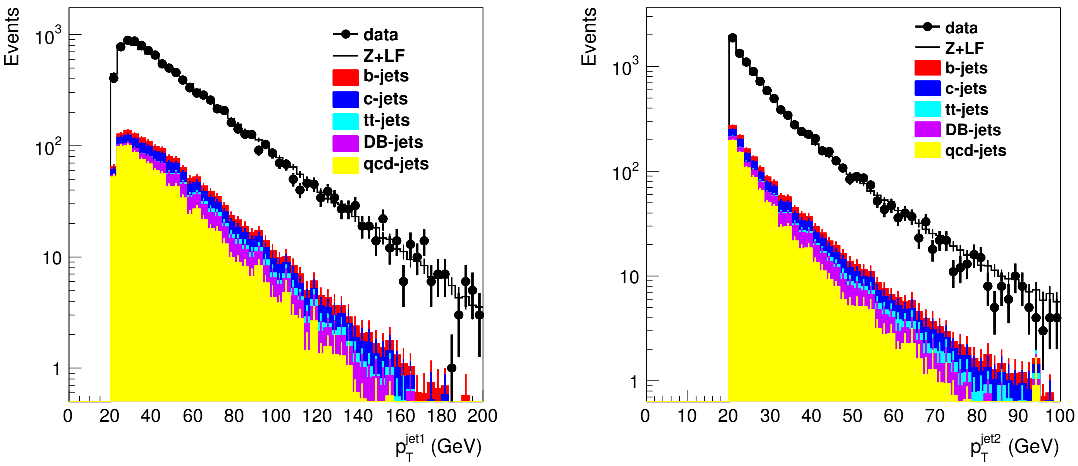

Figure 6.8: The leading and sub leading jet P_T spectrum for data and background in $Z+\geq 2$ jets sample before any b-tagging is applied, in log scale.

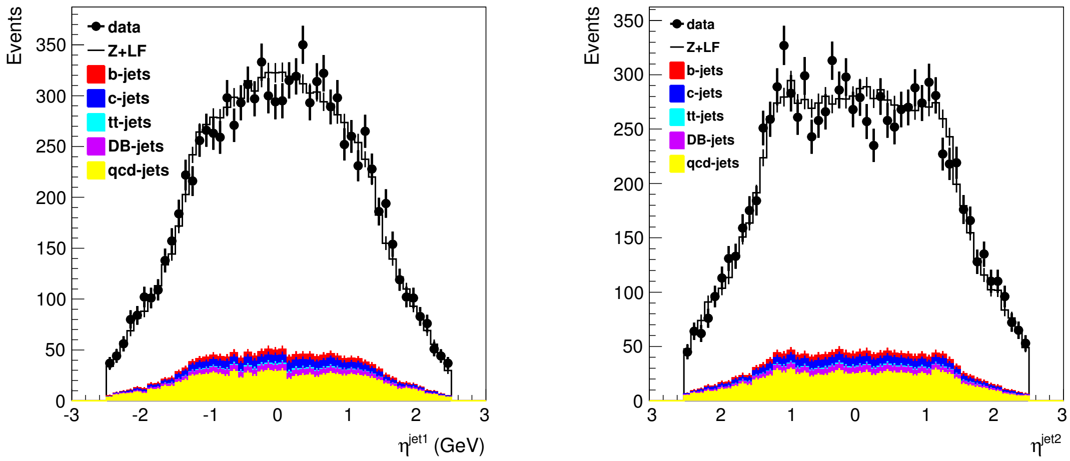

Figure 6.9: The leading and sub leading jet η spectrum for data and background in $Z+\geq 2$ jets sample before any b-tagging is applied.

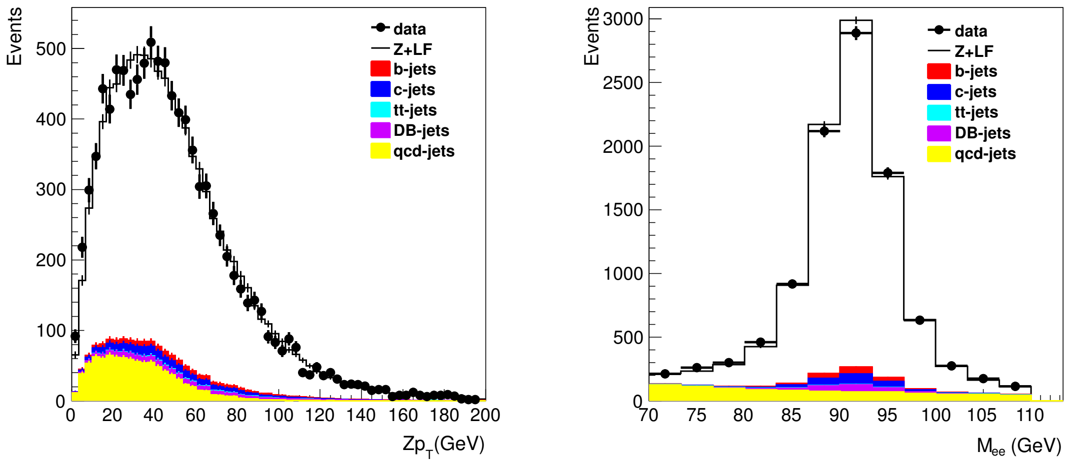

Figure 6.10: The Z P_T spectrum and invariant dielectron mass for data and background.

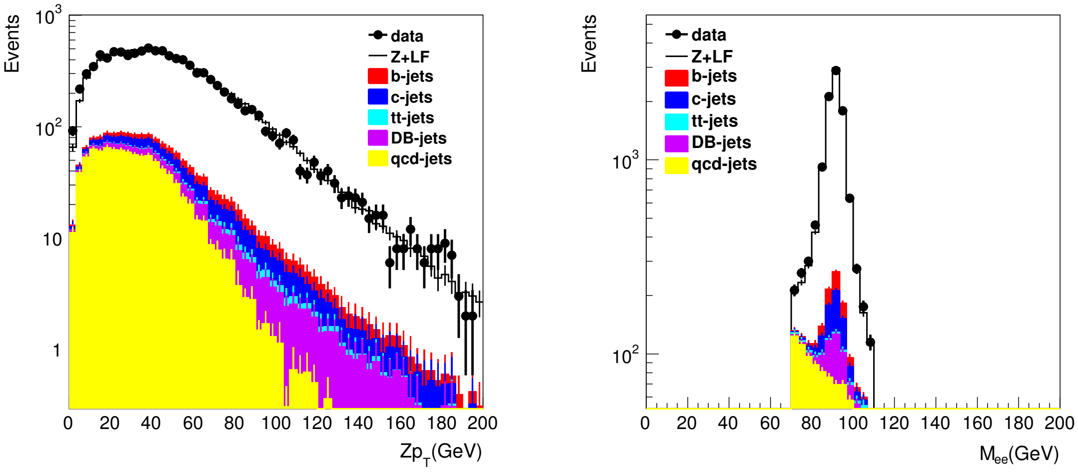

Figure 6.11: The Z P_T spectrum for data and background, in log scale.

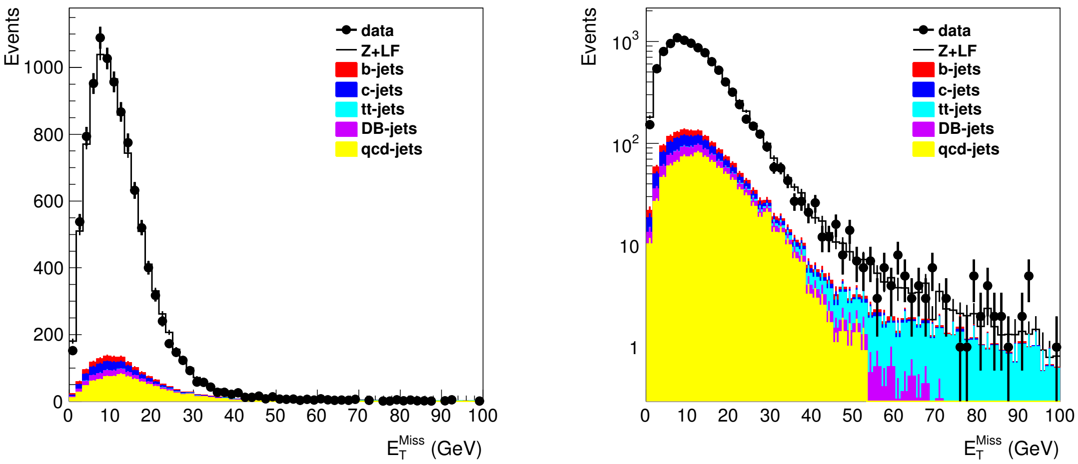

Figure 6.12: The Missing E_T spectrum for data and background and in log scale on right.

6.3 Analysis

There are 10149 and 10801 Z plus at least two jet candidate events in the dielectron and dimuon channels, respectively. The background fraction in dielectron channel is about 11%, and is dominated by the multijet production when two jets mimic isolated electrons. The dimuon channel is much cleaner with the background contribution of 2.4%. A total of 158 (174) events remained in the dielectron (dimuon) sample after the requirement that there be at least two b-tagged jet passing the MVA$_{\text{bl}}$ output cut of 0.15. Events with large missing transverse energy ($>$ 60 GeV) were rejected to suppress the $t\bar{t}$ background reducing it by $\sim$50%. This requirement had minimal effect on the Z+jets, diboson and multijet events in the selected sample.

6.3.1 Identifying Heavy Flavour Jets

Identification of heavy flavour jets and separation of light, c and b jets was carried out in two steps. First, the Z + 2jets preselected sample was enriched with heavy flavor jets. At least two jets were marked as taggable. Then a cut on the MVA$_{\text{bl}}$ output was applied to enrich the samples in b-jets. After this cut, D$_{\text{MJL}}$ was used, to further discriminate light- and c-jets from b-jets and a maximum likelihood fitter was used to extract the flavor fractions for the data set as used in extraction of b-jet flavour fraction in photon plus heavy flavour.

6.3.2 Efficiencies

All efficiencies were calculated after applying the event cuts discussed earlier in the Section 6.1. This means that the following cuts were applied to both numerator and denominator: met$\,<60$, $p_T^{jet_1} > 20$, $70 < Z_m < 110$, |jet physics $\eta| < 2.5$.

6.3.3 Jet Taggability Efficiency

A jet is required to be taggable before the MVA tagger is applied to it. For a jet to be taggable, it must have at least two associated tracks with $p_T\ > 0.5$ GeV, the leading track must have a p_T of at least 1.0 GeV and both tracks must have at least one hit in the SMT. This criteria ensures that the jet has sufficient information to be classified as a heavy flavor candidate. Figure 6.13 illustrates the taggability efficiency (Eqn. 6.2) of jets in $Z+2\,b$ MC as a function of the jet p_T showing that the taggability for b-jets is nearly a constant. The weighted average yields a taggability of 0.84 ± .03. Since the taggability rate was greater in MC than in data, scale factors were applied to correct the MC. To estimate the difference in taggability between data and MC a taggability requirement was applied to a distribution that showed agreement between MC and data beforehand and then measured the disagreement afterwards. Taggability efficiency in data was approximately 0.97% of that in MC. This difference was applied to the b-jet MC taggability.

$$\epsilon_{tagg} = \sum_{i=0}^{L=bins} \frac{N_{p_T}^{taggable\ jet}[i]}{N_{p_T}^{jet}[i]} * \frac{N_{p_T}^{jet}[i]}{N_{jet}} \qquad (6.2)$$

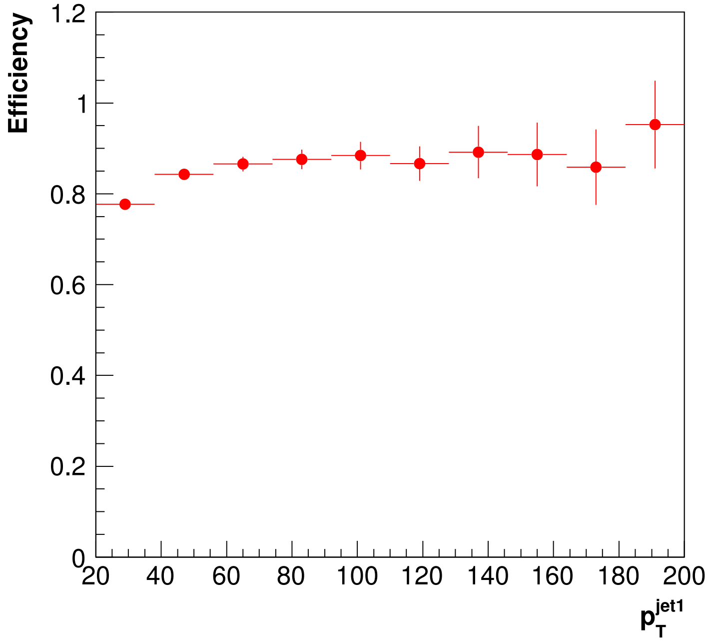

Figure 6.13: b-jet taggability efficiency as a function of jet p_T .

6.3.4 MVA$_{\mathrm{bl}}$Tagger

The MVA$_{\mathrm{bl}}$ tagger allowed for very good discrimination between light-jets and b-jets, as can be seen in Figure. 6.14. A cut at the MEDIUM operating point was applied, as certified by the bID group, which corresponds to MVA$_{\mathrm{bl}} > 0.15$. The p_T weighted average value was found to be $0.33 \pm .02$ for two b jets. To find the value in data a scale factor was applied to account for the difference between data and MC.

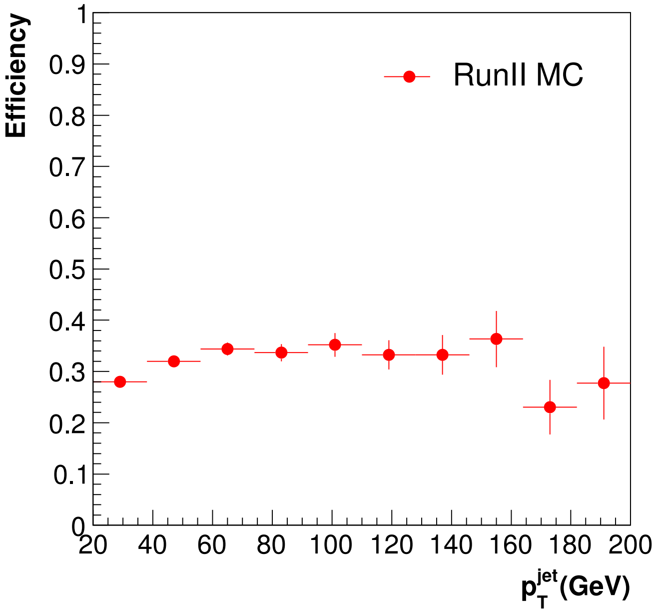

Figure 6.14: The spectrum of b-tagging efficiency as a function of jet transverse momentum measured in $Z + 2\ b$ MC for the b-ID operating point: MEDIUM (MVA$_{\mathrm{bl}}$ >0.15)

6.3.5 Background subtraction

In order to fit the data with the three D$_{\mathrm{MJL}}$ templates, the non-Z+2 jets background must first be subtracted. The sources of the background are diboson, $t\bar{t}$ and QCD multijet. For the diboson and $t\bar{t}$, the MC samples discussed in section 3.2.2 were used. By using the cross sections associated to these samples, the expected number of pre-tagged and tagged events can be determined. For QCD, the event weights were kept through the tagging process and how many tagged events are expected was determined. Just subtracting the number of expected background events from data was not a possibility because these backgrounds being dominated by b-jets. In order to subtract the background, their $\mathrm{D_{MJL}}$ shapes were normalized to the expected number of events, and then that distribution is subtracted from data. The sample composition for different b-tagging operating points has been shown table 6.2. Figure 6.15 illustrates the $\mathrm{D_{MJL}}$ shapes for different backgrounds. Also as an cross-check, an additional cut of H_T (sum of transverse momentum of all jets) < 130 is applied which reduces the $t\bar{t}$ backgrounds by factor of two as shown in Table 6.2.

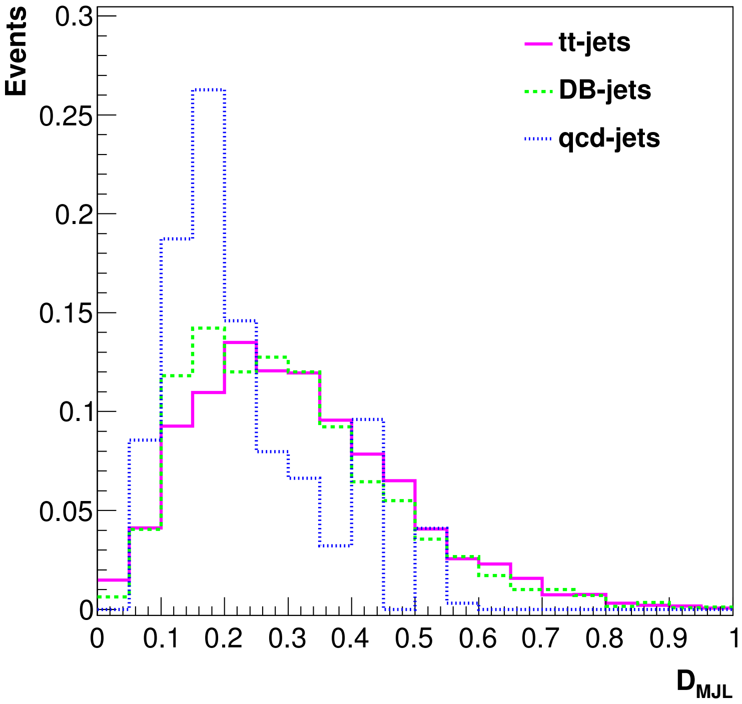

Figure 6.15: MJL templates for different backgrounds

Tagging Criteria	Sample Composition					
	Data	BGD	QCD	DB	$t\bar{t}$	Light Jets
L2,L2	259	53.4	6.3	18.5	28.6	35.9
L,L	189	45.8	4.1	15.8	25.9	17.1
OL,OL	163	42.5	3.5	14.3	24.2	10.8
M,M	139	35.8	3.1	11.9	20.9	4.1
M,M(with HT cut)	97	25.9	2.5	9.9	10.5	3.0

Table 6.2: Calculated background contributions to the b-tagged data set for the ($\mu\mu$ + ee)combined sample at different b-tagging operating points.

6.3.6 Determination of Jet Flavor Fractions

In order to measure the $\sigma(Z + 2\ b - \text{jets})/\sigma(Z + 2\ \text{jets})$ ratio, both the number of $Z + 2$-jet events and the number of $Z + 2$ b-jet events must be determined. To find the number of $Z + 2$-jet events the number of events that match the criteria discussed above was simply counted. To determine the number of $Z + 2$ b-jet events the following prescription was used. First, the MVA_{bl} tagger was applied to the jets in data, as well as the $Z + 2\ b$, $Z + 2\ c$ MC samples. The fraction of b-jets in data can be determined by using the D_{MJL} templates of the passed jets. The $Z + 2\ b$, $Z + 2\ c$ and $Z + 2$ light-jet D_{MJL} templates were fed into a maximum likelihood fitter (ROOT's TFractionFitter) to extract the fractions of each component from data. A two-dimensional (corresponding to the 2 b-jet candidates) maximum likelihood fit of D_{MJL} distributions of 2-jet events in data using the corresponding templates for 2 b jets, 2 c jets and 2 light jets was performed. These jet flavor templates were obtained from MC simulations. The result of maximum likelihood fits to D_{MJL} templates is presented in Fig. 6.16. This shows the one-dimensional projection onto the leading p_T jet D_{MJL} axis of the 2D fit. The figure shows both the data after background subtraction along with the $Z + 2\ b$ jets, $Z + 2\ c$ jets and $Z + 2$ light jets contributions measured by the maximum likelihood fitter. The 2 b-jet fractions obtained in ee channel, $\mu\mu$ channel separately and combined are listed in Table 6.3.

To check the stability of the result, the ratio was remeasured using a looser(tighter) MVA$_{bl}$ selection with the lower limit on the MVA$_{bl}$ output of $> 0.10 (> 0.225)$. The looser selection provides increased data statistics and the tighter selection yields a 2 b enriched sample. The new and default ratios were found to be in agreement within uncertainties of about 4%. To validate the $t\bar{t}$ background estimation, we reduced the contribution of $t\bar{t}$ events by rejecting events where the scalar sum of all jet p_T values was more than 130 GeV. This selection reduced the $t\bar{t}$ fraction by an additional factor of 2 with a signal efficiency of 80%. The new and default ratios were found to be in agreement within systematic uncertainties. The 2 b-jet fractions with $H_T^{jets} < 130$ cut are also shown in Table 6.3.

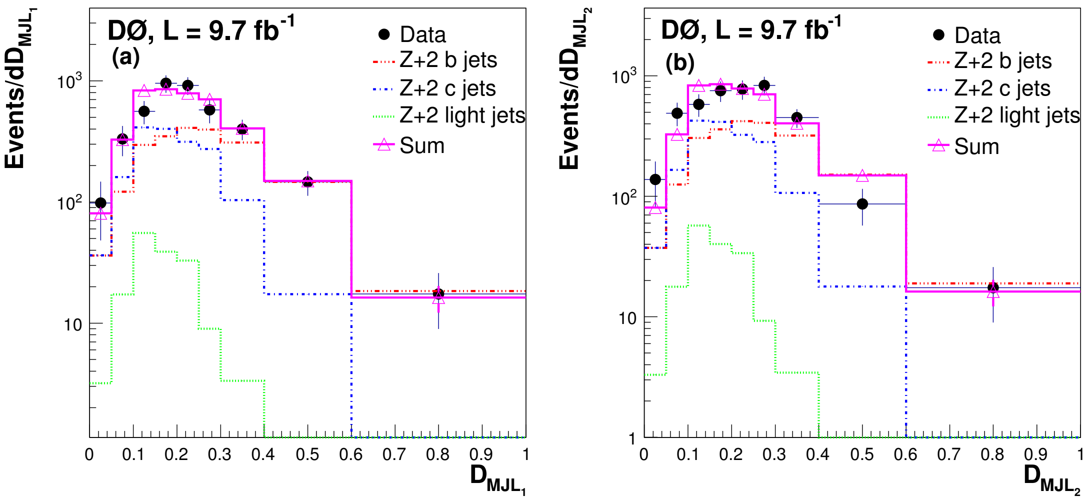

Figure 6.16: The one dimensional projection onto the highest-p_T jet (left) and the second highest-p_T jet (right) $D_{\rm MJL}$ axis of the 2D fit. The distributions of the b, c, and light jets are normalized by the fractions found from the fit.

Region	$Z + 2$ b jet
	$\|\eta\| < 2.5$, $MVA_{\rm bl} > .15$
ee channel	0.56±0.12
$\mu\mu$ channel	0.59±0.14
$\mu\mu$ + ee combined	0.64±0.11
$\mu\mu$ + ee combined (with HT cut)	0.73±0.10

Table 6.3: Table of jet flavor fractions $\mu\mu$, ee and combined.

6.3.7 Acceptance Corrections

Acceptance corrections take into account the events lost due to geometric and basic kinematic selection criteria which are aimed at keeping just EM clusters reconstructed in the fiducial regions in η and ϕ of the calorimeter (i.e. to avoid inter-calorimeter section boundaries and edges). It also "removes" events present at the reconstruction level but absent at the generator level. The acceptance A is calculated as

$$A = \frac{N^{\rm reco}}{N^{\rm part}}, \tag{6.3}$$

where $N^{\rm reco}$ and $N^{\rm part}$ are the numbers of events at the reconstruction and generator (true) level, respectively. In order to quote a combined ratio for the two channels, we corrected to a common lepton acceptance as follows. The detector acceptances for the inclusive jet sample and 2 b jets were determined from MC simulations in the kinematic region that satisfied the p_T and η requirements for leptons and jets. For the $\mathcal{A}_{bb}$ and $\mathcal{A}_{\rm incl}$ calculations, selections for both the electron and muon channels were applied for the fiducial region for the events with two jets and two leptons defined as:

$$p_T^{\text{jet}} > 20 \text{ GeV and } |\eta^{\text{jet}}| < 2.5,$$

$$p_T^{\ell} > 15 \text{ GeV and } |\eta^{\ell}| < 2. \tag{6.4}$$

The resulting ratio of the two acceptances was measured to be $\mathcal{A}_{\text{incl}}/\mathcal{A}_{bb} = 1.09 \pm 0.02$ (stat). The uncertainties on these individual acceptances (A_{incl} and A_{bb})would be large due to the uncertainties on the JES, JER, and the details of simulations, but in ratio these effects are reduced.

6.3.8 Results

The ratio of the cross section of $Z + 2\ b$ to $Z + 2\ jets$ can be calculated using the following form:

$$\frac{\sigma(Z+2\ b)}{\sigma(Z+2\ jet)} = \frac{N_{\text{fitted}} f_{\text{bb}}}{N_Z + j^{\text{presel}} \epsilon^{\text{bb}}_{\text{btag}} \epsilon^{\text{bb}}_{\text{Tagg}}} \times \frac{A_{\text{incl}}}{A_{\text{bb}}} \tag{6.5}$$

where N_{fitted} is the number of b-tagged, background subtracted events used to extract the flavour fraction, $N_Z + j^{\text{presel}}$ is the number of the preselected inclusive $Z + 2\ jet$ events, f_{bb} is the $2\ b - jet$ flavour fraction from the Table 6.3, and the various efficiences can be found in the Table 6.4. $\frac{A_{\text{incl}}}{A_{\text{bb}}}$ is the ratio of acceptances for $Z + 2$-jet and $Z + 2b$-jet events.

	Value	Stat. Uncertainty
$\epsilon^{\text{bb}}_{\text{btag}}$	0.33	0.02
$\epsilon^{\text{bb}}_{\text{tagg}}$	0.84	0.02
N_{fitted}	180	13
$N_Z + j^{\text{presel}}$	19561	140

Table 6.4: The efficiencies and number of events left after flavour extraction together with number of events in $Z + 2$-jet sample and statistical uncertainties on them.

The uncertainty on the flavour fractions obtained from the template fitting to data were mostly statistical. The systematic component was determined by artificially increasing the statistics of data. The error remaining was taken to be the systematic error associated to the template statistics. The result for the $\sigma(z + 2\ b)/\sigma(z + 2\ jet)$ ratio in combined $\mu\mu$ and ee channels for the $\mathrm{MVA_{bl}} > 0.15$ tagging operating point is 0.0236 ± 0.0032 (stat.)± 0.0035(syst.).

6.4 Systematic Uncertainties

- B-tagging Efficiency:

  In order to get the systematic error associated to b-tagging efficiency value, the efficiency was varied both up and down one σ.

- Jet Energy Resolution:

  For the systematic uncertainty in jet energy resolution, the standard resolution was varied both up and down one σ and the ratio was re-measured.

- Jet Energy Scale:

  For the systematic uncertainty in jet energy scale, the standard correction was varied both up and down one σ and the ratio was re-measured.

- Jet Reconstruction Efficiencies for heavy and light quarks:

  While a scale factor is applied to the final ratio to compensate for the difference in jet reconstruction, there is still a small issue. $\frac{\epsilon^{l}_{reco}}{\epsilon^{b}_{reco}}$ assumes that the Z+jet sample is made up entirely of light jets. For a systematic, the scale factor is varied by 2% and take half of the difference in the ratio as the systematic error.

- Background Estimations:

  In order to subtract the background from our data, Monte Carlo generators are relied on to give the number of events. To measure the systematic uncertainty associated to this method, the effect that varying the number of background events up and down by 10% had on the ratio was taken.

- Shape uncertainty - Data vs. MC:

  To estimate the systematic uncertainty due to template differences in data and MC, the templates in both the negative tagged data as well as the Z+light jet MC were used. For both samples the statistics were artificially inflated by multiplying each bin by 10^5. This preserves the original shape, but minimizes the corresponding statistical error in the fit. The fitter was applied with both cases. For the systematic uncertainty the difference of the central values is taken and it amounts to 2.2%.

- Uncertainty due to b-quark fragmentation

  By default, the events have been reweighted from the default PYTHIA b-fragmentation to a Bowler scheme that has been tuned to LEP data. To evaluate the systematics, the events are further reweighted to account for the difference between SLD and LEP data. The fractions are remeasured with the new fragmentation scheme. The difference in the b-fraction between the two schemes is taken as a systematic uncertainty [96].

- $\mathrm{D}_{\mathrm{MJL}}$ Efficiency

  To estimate the systematic uncertainty from the $\mathrm{D}_{\mathrm{MJL}}$ efficiency, the central value of the data to MC scale factor was varied by half of the RMS of the histogram.

Systematic Uncertainty	Percentage
B tagging	5.5%
JES	1.2%
JER	2.3%
Bkgd. Estimate	5.5%
Jet Reco: b vs. light	2%
Template Shape	2.2%
B-fragmentation	1.8%
MJL Efficiency	3.7%
Trigger Corrections ($\mu\mu$) ‘	0.4%
Sum	± 9.6%

Table 6.5: Table of systematic uncertainties and their contribution to the ratio.

Taking into account above systematic uncertainties, the result for the $\sigma(Z + 2\ b)/\sigma(z + 2\ \text{jet})$ ratio in combined $\mu\mu$ and ee channels is 0.0236 ± 0.0032 (stat.) ± 0.0035 (syst.).

6.4.1 Results and Comparison with theory

MCFM provides next-to-leading order (NLO) calculations for the inclusive cross sections of $Z + 2b$ and $Z + 2$ jet production. The calculations were performed using the instructions from the MCFM authors. The calculations were done using MSTW2008 NLO PDFs while calculating NLO contributions. Table 6.6 gives the values of expected cross sections of the processes obtained for the jet kinematic cuts, $p_T > 20$ GeV and $|\eta| < 2.5$. For the leptons, $p_T > 15$ GeV, $|\eta| < 2.5$ and dilepton invariant mass $70 < M_{ll} < 110$ GeV was used. The MCFM predictions used MSTW2008 parton distribution functions (PDFs). The renormalization and factorization scales were set to $Q^2 = M_Z^2$. The statistical errors on the cross sections are very small ($< 0.5\%$). Based on the MCFM predictions, the ratio $\frac{\sigma(z+2\ b)}{\sigma(z+2\ \text{jet})}$ is expected to be $0.0170 \pm^{+0.0003}_{-0.0002}$ for jet $p_T > 20$ GeV and $|\eta| < 2.5$. The uncertainty on the NLO prediction includes the uncertainty arising from choice of the scales, which were varied from $M_Z/2$ to $2M_Z$ and the uncertainty on the PDFs.

Cross sections (fb)	MSTW2008	CTEQ6M	$M_Z/2$	$2M_Z$
$Zb\bar{b}$	50.61	49.29	52.67	45.62
Zjj	2971.48	2918.41	3072.76	2731.60
$\sigma(Zb\bar{b})/\sigma(Zjj)$	$0.0170^{+0.0002}_{-0.0003}$	0.0168		

Table 6.6: The cross section (fb) evaluated by MCFM for Z+heavy flavor and light jet production at the Tevatron. The uncertainties on the ratio are from the variation of renormalization scale, factorization scale and the PDFs.

For the dimuon channel slightly different kinematic cuts on the muon ($p_T > 10$ GeV, $|\eta| <2.0$) were used, but the selection on the jets was same. Table 6.7 gives the values of expected cross sections of the processes and the resultant ratio. The ratio $\frac{\sigma(z+2\ b)}{\sigma(z+2\ \text{jet})}$ obtained is $0.0180\pm^{+0.0005}_{-0.0006}$. The ratio is quite stable within the theoretical uncertainties.

Cross sections (fb)	MSTW2008	CTEQ6M	$M_Z/2$	$2M_Z$
$Zb\bar{b}$	47.54	46.02	49.34	42.50
Zjj	2647.08	2557.87	2667.94	2451.80
$\sigma(Zb\bar{b})/\sigma(Zjj)$	$0.0180^{+0.0005}_{-0.0006}$	0.0179		

Table 6.7: The cross section (fb) evaluated by MCFM for Z+heavy flavor and light jet production at the Tevatron. The uncertainties on the ratio are from the variation of renormalization scale, factorization scale and the PDFs.

The Table 6.8 shows the ratio of integrated cross sections, $\sigma(p\bar{p} \to Z + 2\ b\ \text{jet})/\sigma(p\bar{p} \to Z + 2\ \text{jet})$, in the fiducial region defined in Eq. (6.4). The ratio was compared to predictions from NLO QCD calculations and two MC generators, PYTHIA and ALPGEN. The NLO predictions use the MSTW2008 PDF set [97] using MCFM with central values of renormalization and fragmentation scales $\mu_r = \mu_f = M_Z$. Uncertainties were estimated by varying μ_r and μ_f together by a factor of two, and are about 15%. ALPGEN generates multi-parton final states using tree-level matrix elements. When interfaced with PYTHIA, it employs an MLM scheme [98] to match matrix element partons with those after showering in PYTHIA, resulting in an improvement over leading-logarithmic accuracy.

$\sigma(p\bar{p} \to Z + 2\ b\ \text{jet})/\sigma(p\bar{p} \to Z + 2\ \text{jet})$				
Data $\pm\delta_{\text{stat}} \pm \delta_{\text{syst}}$	δ_{tot}	NLO QCD(MSTW)	PYTHIA	ALPGEN
$(2.36 \pm 0.32 \pm 0.35) \times 10^{-2}$	$0.47{\times}10^{-2}$	$(1.76 \pm 0.26) \times 10^{-2}$	$2.42{\times}10^{-2}$	$2.21{\times}10^{-2}$

Table 6.8: The ratio of integrated cross sections, $\sigma(p\bar{p} \to Z + 2\ b\ \text{jet})/\sigma(p\bar{p} \to Z + 2\ \text{jet})$ together with statistical uncertainties (δ_{stat}) and total systematic uncertainties (δ_{syst}). The column δ_{tot} shows the total experimental uncertainty obtained by adding δ_{stat} and δ_{syst} in quadrature. The last three columns show theoretical predictions obtained using NLO QCD with scale uncertainties and two MC event generators, PYTHIA and ALPGEN.

Chapter 7

Summary and Conclusions

This chapter gives a brief summary of measurements presented in this thesis and the conclusion of the present work:

- We have measured the differential cross sections $d\sigma/dp_T^\gamma$ for the production of photon $+b\bar{b}$-jet events and photon $+b$-jet events with photon rapidities $|y^\gamma| < 1.0$ within p_T^γ of 30–200 GeV, keeping jet $p_T^{\text{jet}} > 15$ GeV and rapidity $|y^{\text{jet}}| < 1.5$ for both jets. This is the first $p\bar{p}$ collider measurement of the differential cross section for associated photon and two heavy flavor jets production. The measured cross sections are well described by the NLO QCD calculations and the predictions from the k_T-factorization approach in the full studied p_T^γ region considering the experimental and theoretical uncertainties. Both of these predictions show consistent behavior, although the predictions from the k_T-factorization approach suffer from larger uncertainties. PYTHIA predicts significantly lower production rates and a more steeply falling p_T^γ distribution than observed in data. SHERPA performs better in describing the normalization at high p_T^γ, but underestimates production rates compared to that observed in data at low p_T^γ.

- In addition to measuring the $\gamma+2$ b-jet cross sections, we also obtain results for the inclusive $\gamma+b$-jet cross section in the same p_T^γ bins. Here we follow the same procedure as described in the previous similar D0 measurement. However, as for the $\gamma + 2$ b-jet cross section measurement, we now use the most recent HF tagging algorithm. Data and predictions are also presented in Table 5.7. The values of the obtained $\gamma+b$-jet cross section are consistent with our previously published results. We use $\sigma(\gamma + 2$ b-jet) and $\sigma(\gamma + b$-jet) cross sections to calculate their ratio in bins of p_T^γ. Figure 5.19 shows the p_T^γ spectrum of the measured ratio. The measurements are well described by the calculations done by NLO QCD and k_{T}-factorization predictions taking into account the experimental and theoretical uncertainties. The scale uncertainties on the NLO calculations are typically $\lesssim 15\%$, while they vary up to 35% at high p_T^γ for the k_{T}-factorization approach. The predictions from SHERPA describe the shape, but underestimate the ratio for most of the p_T^γ bins. The PYTHIA model does not perform well in describing the shape and underestimates ratios across all the bins. These results allow the tuning of the theoretical predictions for the $\gamma + b$ production process, understanding which is of great importance for QCD *per se* and also great relevance for improving the sensitivity of searches for the Higgs boson and other new phenomena at the Tevatron and the LHC, in which vector boson $+b$ jet final state is a dominating background.

- We also measured the ratio of integrated cross sections, $\sigma(p\bar{p} \to Z + 2\,b\text{ jet})/\sigma(p\bar{p} \to Z{+}2\text{ jet})$, for events with $Z \to \ell\ell$ in a restricted phase space of leptons with $p_T^\ell > 15$ GeV, $|\eta^\ell| < 2.0$ and with two jets limited to $p_T^{\mathrm{jet}} > 20$ GeV and $|\eta^{\mathrm{jet}}| < 2.5$. Measurements are based on the full data sample collected by the DØ experiment in Run II of the Tevatron, corresponding to an integrated luminosity of 9.7 fb^{-1} at a center-of-mass energy of 1.96 TeV. Several systematic uncertainties cancel when the ratio $\sigma(Z + 2\ b\text{ jets})/\sigma(Z + 2\text{ jets})$ is measured. These include uncertainties on the luminosity measurement, lepton trigger efficiency, and lepton and jet reconstruction efficiencies. The remaining uncertainties are estimated separately for the integrated result. The largest systematic uncertainty of 13.7% comes from the uncertainty on the shape of the D_{MJL} templates used in the fit including that due to MC statistics of the samples used to construct the templates. The shape of the templates may be affected by the choice of the b quark fragmentation function [99], the background estimation, the difference in the shape of the light jet MC template and a template derived from a light jet enriched dijet data sample, and the composition of the charm states used to determine the charm template shape [48]. It also includes uncertainties on production rates of different hadrons and uncertainties on branching fractions. These effects are evaluated by varying the central values by the corresponding uncertainties, one at a time. The entire analysis chain is checked for possible biases using a MC closure test and no significant deviations are observed. The next largest systematic uncertainty of 5.5% is due to the b-jet identification efficiency. The uncertainty on b-jet energy calibration is 2.6%; it comprises the uncertainties on the jet energy resolution and the jet energy scale. For the integrated ratio measurement, these uncertainties, when summed in quadrature, result in a total systematic uncertainty of 14.9%. For the integrated ratio we obtain

$$R = 0.0236 \pm 0.0032\,(\mathrm{stat}) \pm 0.0035\,(\mathrm{syst})\,. \tag{7.1}$$

The ratio is compared to predictions from NLO QCD calculations and two MC generators, PYTHIA and ALPGEN. The measured integrated ratio is found to be in agreement with the theoretical predictions within uncertainties. This result is important for tuning the theory as good theoretical description of this process is essential since it forms a major background for a variety of physics processes, including standard model (SM) Higgs boson production in association with a Z boson, $ZH(H \to b\bar{b})$ [100,101], and searches for supersymmetric partners of the b quark [102, 103].

These results will improve our theoretical understanding as we search for phenomena beyond the standard model using the data from collider experiments in the case where the final states of the interaction involved the production of vector bosons in association with two b-quark jets.

This work has been published in Phys. Rev. D **91**, 052010 and Phys. Lett. B **737**, 357. The detailed analysis is documented in our DØ Note 6423.

Bibliography

[1] M. Veltman, “Facts and Mysteries in Elementary Particle Physics,” World Scientific (2003).

[2] D. Griffiths, “Introduction to Elementary Particles,” John Wiley Sons (1987).

[3] D. H. Perkins, “Introduction to High Energy Physics,” Addison-Wesley Publishing Company (1972).

[4] S. B. Beri, “Concepts of High Energy and Nuclear Physics,” Elite Publishing House (2007).

[5] F. Halzen and A. Martin, “Quarks and Leptons,” John Wiley Sons (1984).

[6] M. E. Peskin and D. V. Schroeder, “An Introduction to Quantum Field Theory,” Addison Wesley, (1995).

[7] C. Quigg, “Gauge Theories of the Strong, Weak, and Electromagnetic Interactions,” Westview Press (1983).

[8] J. Beringer *et al.*, (Particle Data Group Collaboration), “Review of Particle Physics (RPP),” Phys. Rev. D **86**, 010001 (2012).

[9] S. L. Glashow, “Partial Symmetries of Weak Interactions,” Nucl. Phys. **22**, 579-588 (1961).

[10] J. Goldstone, A. Salam and S. Weinberg, "Broken Symmetries," Phys. Rev. **127**, 965-970 (1962).

[11] S. Weinberg, "A Model of Leptons", Phys. Rev. Lett. **19**, 1264-1266 (1967).

[12] F. Englert and R. Brout, "Broken Symmetry and the Mass of Gauge Vector Mesons," Phys. Rev. Lett. **13**, 321-323 (1964).

[13] G. S. Guralnik, C. R. Hagen, and T. W. B. Kibble, "Global Conservation Laws and Massless Particles," Phys. Rev. Lett. **13**, 585-587 (1964).

[14] P. W. Higgs, "Broken Symmetries and the Masses of Gauge Bosons," Phys. Rev. Lett. **13**, 508-509 (1964).

[15] G. Aad *et al.* (ATLAS Collaboration),"Observation of a new particle in the search for the Standard Model Higgs boson with the ATLAS detector at the LHC," Phys. Lett. B **716**, 1 (2012).

[16] S. Chatrchyan *et al.* (CMS Collaboration), "Observation of a new boson at a mass of 125 GeV with the CMS experiment at the LHC," Phys. Lett. B **716**, 30 (2012).

[17] T. Aaltonen and V. M. Abazov *et al.* (CDF and DØ Collaborations) "Higgs Boson Studies at the Tevatron," Phys. Rev. D **88**, 052014 (2013).

[18] R. Ellis *et al.*, "QCD and Collider Physics," Cambridge University Press (1996).

[19] R. P. Feynman, "QED : The Strange Theory of Light and matter," Princeton University Press, Princeton,(1985).

[20] J. F. Owens, "Large-momentum-transfer production of direct photons, jets, and particles," Rev. Mod. Phys. **59**, 465 (1987).

[21] G. Kane, "Modern Elementary Particle Physics," Addison-Wesley, (1993).

[22] V. N. Gribov and L. N. Lipatov, “Deep inelastic e p scattering in perturbation theory,” Nucl. Phys. **15**, 438-450 (1972).

[23] G. Altarelli and G. Parisi, “Asymptotic Freedom in Parton Language,” Nucl. Phys. B **126**, 298 (1977).

[24] Y. L. Dokshitzer, “Calculation of the Structure Functions for Deep Inelastic Scattering and e+ e- Annihilation by Perturbation Theory in Quantum Chromodynamics,” Sov. Phys. JETP **46**, 641 (1977).

[25] T. Stavreva and J. F. Owens, “Direct Photon Production in Association With A Heavy Quark At Hadron Colliders,” Phys.Rev. D **79** 054017 (2009).

[26] B. W. Harris and J. F. Owens, “The two cutoff phase space slicing method,” Phys. Rev. D **65**, 094032 (2002).

[27] P. M. Nadolsky *et al.*, “Implications of CTEQ global analysis for collider observables,” Phys. Rev. D **78**, 013004 (2008).

[28] T. Sjostrand, S. Mrenna and P. Z. Skands, “PYTHIA 6.4 Physics and Manual,” JHEP 0605, 026 (2006).

[29] H. B. Hartanto and L. Reina,“Hard-photon Production with *b* jets at Hadron Colliders,” Phys. Rev. D **89**, 074001 (2014).

[30] W. K. Tung, “Status of Global QCD Analysis and the Parton Structure of the Nucleon,” arXiv:0409145[hep-ph] (2004).

[31] W. K. Tung, H. L. Lai, J. Pumplin, P. Nadolsky and C. P. Yuan, “Heavy Quark Mass Effects in PQCD and Heavy Flavor Parton Distributions,” arXiv:0707.0320 [hep-ph] (2007).

[32] J. Pumplin *et al.*,“New Generation of Parton Distributions with Uncertainties from Global QCD Analysis,” JHEP 0207, 12 (2002).

[33] M. Gluck *et.al*, "On the role of heavy flavor parton distributions at high energy colliders," Phys. Lett. **B 664** 133-138 (2008).

[34] B. Abbott *et al.*, (DØ Collaboration), "Cross Section for b-Jet Production in $\bar{p}p$ Collisions at $\sqrt{s} = 1.8 TeV$," Phys.Rev.Lett. **85** 5068 (2000).

[35] A. Abulencia *et al.*, (CDF Collaboration), " Photon+b -jet cross-section at CDF", CDF Note 8377, (2006). `http://www-cdf.fnal.gov/physics/new/qcd/QCD.html`

[36] V. M. Abazov *et al*, "A Measurement of the Ratio of Inclusive Cross Sections $p\bar{p} \to Zb/p\bar{p} \to Zj$ at $\sqrt{s} = 1.96$ TeV," Phys. Rev. Lett. **94**, 161801 (2005).

[37] A. Abulencia *et al.*, (CDF Collaboration), "Measurement of the b Jet Cross Section in Events with a Z Boson in $p\bar{p}$ collisions at $\sqrt{s} = 1.96$ TeV," Phys. Rev. D**74**, 032008 (2006).

[38] T. Aaltonen *et al.*, (CDF Collaboraton),"Measurement of the Cross Section for b Jet Production in Events with a Z Boson in $p\bar{p}$ Collisions $\sqrt{s} = 1.96$ TeV," Phys. Rev. D **79**, 052008 (2009).

[39] T. Aaltonen *et al.* (CDF Collaboration), "Study of the associated production of photons and b-quark jets in $p\bar{p}$ collisions at $\sqrt{s} = 1.96$ TeV," Phys. Rev. D **81**, 052006 (2010).

[40] V. M. Abazov *et al.* (DØ Collaboration), "Measurement of $\gamma + b + X$ and $\gamma + c + X$ Production Cross Sections in $p\bar{p}$ Collisions at $\sqrt{s} = 1.96$ TeV," Phys. Rev. Lett. **102**, 192002 (2009).

[41] V. M. Abazov *et al.* (DØ Collaboration), "Measurement of the photon+b-jet production differential cross section in $p\bar{p}$ collisions at $\sqrt{s} = 1.96$ TeV," Phys. Lett. B **714**, 32-39 (2012).

[42] V. M. Abazov *et al.* (DØ Collaboration), "Measurement of the differential photon + c-jet cross section and the ratio of differential photon+ c and photon+ b cross sections in proton-antiproton collisions at $\sqrt{s} = 1.96$ TeV," Phys. Lett. B **719**, 354 (2013).

[43] T. Aaltonen *et al.* (CDF Collaboration), "Measurement of the Cross Section for Direct-Photon Production in Association with a Heavy Quark in $p\overline{p}$ Collisions at $\sqrt{s}$=1.96 TeV," Phys. Rev. Lett. **111**, 042003 (2013).

[44] T. Andeen *et al.*, FERMILAB-TM-2365 (2007).

[45] J. M. Campbell, R. K. Ellis, F. Maltoni, and S. Willenbrock, "Production of a W Boson and Two Jets with One b-quark Tag," Phys. Rev. D **69**, 074021 (2004).

[46] J. M. Campbell, R. K. Ellis, F. Maltoni, and S. Willenbrock,"Production of a Z boson and two jets with one heavy-quark tag," Phys. Rev. D **73**, 054007 (2006).

[47] F. F. Cordero, L. Reina, and D. Wackeroth,"NLO QCD corrections to $Zb\bar{b}$ production with massive bottom quarks at the Fermilab Tevatron," Phys. Rev. D **78**, 074014 (2008).

[48] V. M. Abazov *et al*, (DØ Collaboration), "Measurement of the ratio of inclusive cross sections $\sigma(p\overline{p} \to Z + b\text{-quark jet})/\sigma(p\overline{p} \to Z + \text{jet})$ at $\sqrt{s} = 1.96$ TeV," Phys. Rev. D **83**, 031105 (2011).

[49] V. Shiltsev, "Status of Tevatron Collider Run II and Novel Technologies for Luminosity Upgrades", in: Proc. 2004 European Particle Accelerator Conference, Lucern, Switzerland, Vol.1, p. 239 (2004).

[50] V. M. Abazov *et al.* (DØ Collaboration), "The upgraded DØ detector," Nucl. Instrum. Methods in Phys. Res. A **565**, 463 (2006).

[51] M. Abolins *et al.* (DØ Collaboration),"Design and implementation of the new DØ level-1 calorimeter trigger ," Nucl. Instrum. Methods in Phys. Res. A **584**, 75 (2008).

[52] R. Angstadt *et al.* (DØ Collaboration), "The layer 0 inner silicon detector of the DØ experiment," Nucl. Instrum. Methods Phys. Res. A **622**, 298 (2010).

[53] S. N. Ahmed *et al.* (DØ Collaboration), "The DØ Silicon Microstrip Tracker", Nucl. Instrum. Methods Phys. Res. A **634**, 8 (2011); `http://www-d0.fnal.gov/trigger/stt/smt/smt_tdr.ps`.

[54] D. Adams *et al.* (DØ Collaboration), "The DØ Upgrade: Central Fiber Tracker, Technical Design Report", DØ Note 4164 (1999).

[55] M. Adams *et al.* (DØ Collaboration), "Central Fiber Tracker Technical Design Report", DØ Note 3014 (1996).

[56] M. Adams *et al.* (DØ Collaboration), "The DØ Upgrade: Forward Preshower, Muon System and Level 2 Trigger", DØ Note 2894 (1996).

[57] S. Abachi *et al.* (DØ Collaboration), "The DØ Detector", Nucl. Instr. and Methods A **338**, 185 (1994).

[58] `http://www-d0.fnal.gov/Run2Physics/top/top_public_web_pages/top_dzero_detector.html`.

[59] T. Edwards, *et al.*, FERMILAB-TM-2278-E (2004).

[60] V. M. Abazov *et al.* (DØ Collaboration)," Electron and Photon Identification in the DØ Experiment," Nucl. Instrum. Methods Phys. Res. A **750**, 78 (2014). `http://www-d0.fnal.gov/phys_id/emid/d0_private/emid.html`.

[61] R. Brun, F. Bruyant, F. Carminati, S. Giani, M. Maire, A. McPherson, G. Patrick and L. Urban, "GEANT Detector Description and Simulation Tool," CERN-W5013, CERN-W-5013, W5013, W-5013 (1994).

[62] DØ MC event selector, `http://www-clued0.fnal.gov/d0_mess/`

[63] V. M. Abazov *et al.* (DØ Collaboration), "Measurement of the isolated photon cross section in $p\bar{p}$ collisions at $\sqrt{s} = 1.96$ TeV", Phys. Lett. **B639**, 151-158 (2006).

[64] D0 Data Quality Coordination, http://www-d0.fnal.gov/computing/data_quality/d0_private/forusers.html.

[65] Common Samples Group, http://www-d0.fnal.gov/Run2Physics/cs/MC/MC.html.

[66] M. L. Mangano *et al.*, "ALPGEN, a generator for hard multiparton processes in hadronic collisions," JHEP **0307**, 001 (2003).

[67] MLM matching procedure, `http://www-d0.fnal.gov/computing/MonteCarlo/generators/common_alpgen.html`.

[68] D. Gillberg, "Heavy Flavour Removal and Determination of Weighting Factors for ALPGEN W+jet Monte Carlo," DØ Note 5129 (2006).

[69] J. Campbell and R. K. Ellis, "An update on vector boson pair production at hadron colliders," Phys. Rev. D, **60**, 113006 (1999). `http://mcfm.fnal.gov/`

[70] C. Tully and A. Schwartzman, "Primary Vertex Reconstruction by Means of Adaptive Vertex Fitting," DØ Note 4918 (2005).

[71] O. Atramentov, D. Bandurin and Y. Maravin ,"Photon energy scale for jet energy scale setting," DØ Note 4974 (2006).

[72] G. C. Blazey *et al.*, "Run II Jet Physics: Proceedings of the Run II QCD and Weak Boson Physics Workshop," arXiv:0005012[hep-ex] (2000).

[73] V. Abazov*et al.* (DØ Collaboration),"Jet energy scale determination in the DØ experiment," Nucl. Instrum. Methods Phys. Res. A **763**, 442 (2014).

[74] A. Schwartzman and M. Narain, "Secondary vertex reconstruction using the Kalman Filter," DØ Note 3908 (2001).

[75] S. Abachi *et al.* (DØ Collaboration),"Isolated Photon Cross Section in the Central and Forward Rapidity Regions in $p\overline{p}$ Collisions at $\sqrt{s} = 1.8$TeV," Phys. Rev. Lett. **77**, 5011 (1996).

[76] B. Abbott *et al.* (DØ Collaboration), "Isolated Photon Cross Section in $p\overline{p}$ Collisions at $\sqrt{s} = 1.8$TeV," Phys. Rev. Lett. **84**, 2786 (2000).

[77] V. M. Abazov *et al.* (DØ Collaboration),"The ratio of the isolated photon cross sections at $\sqrt{s} = 630$ GeV and 1800 GeV," Phys. Rev. Lett. **87**, 251805 (2001).

[78] V. M. Abazov *et al.* (DØ Collaboration),"Measurement of the $t\bar{t}$ production cross section in $p\overline{p}$ collisions at $\sqrt{s} = 1.96$ TeV using secondary vertex b tagging," Phys. Rev. D. **74** 112004 (2006).

[79] V. M. Abazov *et al.* (DØ Collaboration), "Improved b quark jet identification at the DØ experiment," Nucl. Instrum. Methods Phys. Res. A **763**, 290 (2014).

[80] L. Breiman, "Random Forests," Machine Learning 45, 5 (2001)

[81] A. Hocker *et al.*, "TMVA - Toolkit for Multivariate Data Analysis," PoS ACAT, 040 (2007).

[82] R. Brun and F. Rademakers, "ROOT: An object oriented data analysis framework," Nucl. Instrum. Meth. Phys. Res. A **389**, 81 (1997).

[83] S. Trincaz-Duvoid and P. Verdier, "Missing E_T reconstruction in p17", DØ Note 4474 (2004).

[84] A. Harel, "Jet ID Optimization," DØ note 4919 (2006) .

[85] D. Bandurin, M. Hohlfeld and K. Kaadze, "Electron trigger efficiencies in Common Analysis Framework for Run II Data", DØ Note 5911 (2009).

[86] V.M. Abazov *et al.* (DØ Collaboration), "Measurement of Direct Photon Pair Production Cross Sections in $p\overline{p}$ Collisions at $\sqrt{s} = 1.96$ TeV," Phys. Lett. B **690**, 108 (2010).

[87] I. Anghel, C. Gerber, L. Shabalina and T. Ten, "Studies of Taggability vs. nPV for p17," DØ Note 5240 (2006);

[88] R. Barlow and C. Beston,"Fitting using finite Monte Carlo samples," Comp. Phys. Comm. **77**, 219-228 (1993).

[89] V. M. Abazov *et al.*, (DØ Collaboration), "Measurement of the differential cross section for the production of an isolated photon with associated jet in $p\overline{p}$ Collisions at $\sqrt{s} = 1.96$ TeV," Phys. Lett. B **666**, 2435 (2008); (DØ Note 5368).

[90] Z. Hubacek, *et al*, "D0JetSim - A Parameterized Detector Simulation for Jet Physics," DØ note 5703 (2008).

[91] M. Albrow, *et al* (TeV4LHC QCD Working Group), "Tevatron-for-LHC Report of the QCD Working Group," arXiv:0610012[hep-ex] (2006).

[92] T. Binoth, J. P. Guillet, E. Pilon and M. Werlen, "A Next-to-leading order study of photon pion and pion pair hadro production in the light of the Higgs boson search at the LHC," Eur. Phys. J. direct **4** 7 (2002).

[93] S. P. Baranov, A. V. Lipatov and N. P. Zotov, "Associated production of prompt photons and heavy quarks in off-shell gluon-gluon fusion," Eur. Phys. J. direct **56** 371-378 (2008).

[94] V. M. Abazov *et al.* (DØ Collaboration),“ Muon reconstruction and identification with the Run II DØ detector,” Nucl. Instrum. Methods in Phys. Res. A **737**, 281 (2014).

[95] V. M. Abazov *et al*, (DØ Collaboration), “ Measurement of the ratio of inclusive cross sections $\frac{\sigma(p\bar{p}\to Z+b)}{\sigma(p\bar{p}\to Z+j)}$ at $\sqrt{s} = 1.96$ TeV,” Phys. Rev. D **83**, 031105 (2011).

[96] Y. Peters, M. Begel, K. Hamacher and D. Wicke, “Reweighting of the fragmentation functions for the DØ Monte Carlo”, DØ Note 5325, (2007).

[97] A.D. Martin, W. J. Stirling and R. S. Throne,“Parton distributions for the LHC,” Eur. Phys. J. C **63**, 189 (2009).

[98] F. Caravaglios, M. L. Mangano, M. Moretti and R. Pittau,“A new approach to multi-jet calculations in hadron collisions (article) ,” Nucl. Phys. B **539**, 215 (1999).

[99] V. M. Abazov *et al.* (DØ Collaboration),“Precise measurement of the top-quark mass from lepton + jets events at D0,” Phys. Rev. D **84**, 032004 (2011).

[100] V. M. Abazov *et al.* (DØ Collaboration),“Search for the Standard Model Higgs Boson in $ZH \to \ell^+\ell^- b\bar{b}$ Production with the DØ Detector in 9.7 fb^{-1} of $p\overline{p}$ Collisions at $\sqrt{s} = 1.96$ TeV,” Phys. Rev. Lett. **109**, 121803 (2012).

[101] T. Aaltonen *et al.* (CDF Collaboration), “Search for the Standard Model Higgs Boson Decaying to a $b\bar{b}$ Pair in Events with Two Oppositely Charged Leptons Using the Full CDF Data Set,” Phys. Rev. Lett. **109**, 111803 (2012).

[102] V. M. Abazov *et al.* (DØ Collaboration), “Search for scalar bottom quarks and third-generation leptoquarks in $p\overline{p}$ Collisions at $\sqrt{s} = 1.96$ TeV,” Phys. Lett. B **693**, 95 (2010)

[103] T. Aaltonen *et al.* (CDF Collaboration), "Search for the Production of Scalar Bottom Quarks in $p\overline{p}$ Collisions at $\sqrt{s} = 1.96$ TeV," Phys. Rev. Lett. **105**, 081802 (2010).

List of Publications

No. of Publications as co-author of DØ collaboration: 24

Following is the list of publications and DØ notes for present work (S. Beri, M. Kaur *et. al.*)

- **"Measurement of the ratio of inclusive cross sections $\sigma(p\bar{p} \to Z + 2\ b\text{jets})/\sigma(p\bar{p} \to Z + 2\ \text{jets})$ in $p\bar{p}$ collisions at $\sqrt{s} = 1.96$ TeV"**

  V. M. Abazov *et al.* [D0 Collaboration].

  arXiv:1501.05325 [hep-ex]

  DOI:10.1103/PhysRevD.91.052010

  Phys. Rev. D **91**, no. 5, 052010 (2015)

  FERMILAB-PUB-15-013-E

- **"Measurement of the differential $\gamma + 2\ b$-jet cross section and the ratio $\sigma(\gamma + 2\ b\text{-jets})/\sigma(\gamma + b\text{-jet})$ in $p\bar{p}$ collisions at $\sqrt{s} = 1.96$ TeV"**

  V. M. Abazov *et al.* [D0 Collaboration].

  arXiv:1405.3964 [hep-ex]

  DOI:10.1016/j.physletb.2014.09.007

  Phys. Lett. B **737**, 357 (2014)

  FERMILAB-PUB-14-135-E

- **"Measurement of cross section of isolated photon production in association with bottom quark pair and ratio of photon+bb(bar) to photon+b-jet production"**

  S. Beri, D. Bandurin, M. Kaur and A. Kumar

  DØ Note 6423, (2014)

- **"Update on the s-channel production cross section of single top quarks in $9.7 fb^{-1}$ of ppbar data"**

  S. Bala, V. Bazterra, A. Garcia-Bellido, C. E. Gerber, J. Ellison, A. Heinson, J. Joshi, M. Kaur, R. Schwienhorst and Y. Tsai

  DØ Note 6414 (2014)

- **“Measurement of the Single Top Production Cross Section in $9.7 fb^{-1}$ of Data”**
  S. Bala, V. Bazterra, A. Garcia-Bellido, C. E. Gerber, J. Ellison, A. Heinson, J. Joshi, M. Kaur, R. Schwienhorst and Y. Tsai
  DØ Note 6375 (2013)

DØ Publications as co-author

- **“Measurement of the Top Quark Mass Using the Matrix Element Technique in Dilepton Final States”**
  V. M. Abazov *et al.* [D0 Collaboration].
  arXiv:1606.02814 [hep-ex]
  FERMILAB-PUB-16-219-E

- **“Measurement of the inclusive $t\bar{t}$ production cross section in $p\bar{p}$ collisions at $\sqrt{s} = 1.96$ TeV and determination of the top quark pole mass”**
  V. M. Abazov *et al.* [D0 Collaboration].
  arXiv:1605.06168 [hep-ex]
  FERMILAB-PUB-16-180-E

- **“Measurement of the Forward-Backward Asymmetries in the Production of and Baryons in $p\overline{p}$ Collisions”**
  V. M. Abazov *et al.* [D0 Collaboration].
  arXiv:1605.03513 [hep-ex]
  DOI:10.1103/PhysRevD.93.112001
  Phys. Rev. D **93**, no. 11, 112001 (2016)
  FERMILAB-PUB-16-168-E

- **“B_s^0 lifetime measurement in the CP-odd decay channel $B_s^0 \to J/\psi\ f_0(980)$”**

V. M. Abazov *et al.* [D0 Collaboration].

arXiv:1603.01302 [hep-ex]

DOI:10.1103/PhysRevD.94.012001

Phys. Rev. D **94**, no. 1, 012001 (2016)

FERMILAB-PUB-16-071-E

- **"Measurement of Spin Correlation between Top and Antitop Quarks Produced in $p\bar{p}$ Collisions at $\sqrt{s} = 1.96$ TeV"**

  V. M. Abazov *et al.* [D0 Collaboration].

  arXiv:1512.08818 [hep-ex]

  DOI:10.1016/j.physletb.2016.03.053

  Phys. Lett. B **757**, 199 (2016)

  FERMILAB-PUB-15-581-E

- **"Study of double parton interactions in diphoton + dijet events in $p\bar{p}$ collisions at $\sqrt{s} = 1.96$ TeV"**

  V. M. Abazov *et al.* [D0 Collaboration].

  arXiv:1512.05291 [hep-ex]

  DOI:10.1103/PhysRevD.93.052008

  Phys. Rev. D **93**, no. 5, 052008 (2016)

  FERMILAB-PUB-15-562-E

- **"Measurement of the forward-backward asymmetry of Λ and $\bar{\Lambda}$ production in $p\bar{p}$ collisions"**

  V. M. Abazov *et al.* [D0 Collaboration].

  arXiv:1511.05113 [hep-ex]

  DOI:10.1103/PhysRevD.93.032002

  Phys. Rev. D **93**, no. 3, 032002 (2016)

  FERMILAB-PUB-15-496-E

- **“Evidence for simultaneous production of J/ψ and Υ mesons”**

  V. M. Abazov *et al.* [D0 Collaboration].

  arXiv:1511.02428 [hep-ex]

  DOI:10.1103/PhysRevLett.116.082002

  Phys. Rev. Lett. **116**, no. 8, 082002 (2016)

  FERMILAB-PUB-15-485-E

- **“Inclusive Production of the X(4140) State in $p\overline{p}$ Collisions at D0”**

  V. M. Abazov *et al.* [D0 Collaboration].

  arXiv:1508.07846 [hep-ex]

  DOI:10.1103/PhysRevLett.115.232001

  Phys. Rev. Lett. **115**, no. 23, 232001 (2015)

  FERMILAB-PUB-15-373-E

- **“Precise measurement of the top quark mass in dilepton decays using optimized neutrino weighting”**

  V. M. Abazov *et al.* [D0 Collaboration].

  arXiv:1508.03322 [hep-ex]

  DOI:10.1016/j.physletb.2015.10.086

  Phys. Lett. B **752**, 18 (2016)

  FERMILAB-PUB-15-338-E

- **“Simultaneous measurement of forward-backward asymmetry and top polarization in dilepton final states from $t\bar{t}$ production at the Tevatron”**

  V. M. Abazov *et al.* [D0 Collaboration].

  arXiv:1507.05666 [hep-ex]

  DOI:10.1103/PhysRevD.92.052007

  Phys. Rev. D **92**, 052007 (2015)

  FERMILAB-PUB-15-312-E

- **“Search for Violation of CPT and Lorentz invariance in B_s^0 meson oscillations”**

  V. M. Abazov *et al.* [D0 Collaboration].

  arXiv:1506.04123 [hep-ex]

  DOI:10.1103/PhysRevLett.115.161601, 10.1103/PhysRevLett.116.019901

  Phys. Rev. Lett. **115**, no. 16, 161601 (2015), Addendum: [Phys. Rev. Lett. **116**, no. 1, 019901 (2016)]

  FERMILAB-PUB-15-258-E

- **“Tevatron Combination of Single-Top-Quark Cross Sections and Determination of the Magnitude of the Cabibbo-Kobayashi-Maskawa Matrix Element $\mathbf{V_{tb}}$”**

  T. A. Aaltonen *et al.* [CDF and D0 Collaborations].

  arXiv:1503.05027 [hep-ex]

  DOI:10.1103/PhysRevLett.115.152003

  Phys. Rev. Lett. **115**, no. 15, 152003 (2015)

  FERMILAB-PUB-15-088-E

- **“Measurement of the forward-backward asymmetry in ^0_b and $\overline{\ }^0_b$ baryon production in $p\bar{p}$ collisions at $\sqrt{s}$=1.96 TeV”**

  V. M. Abazov *et al.* [D0 Collaboration].

  arXiv:1503.03917 [hep-ex]

  DOI:10.1103/PhysRevD.91.072008

  Phys. Rev. D **91**, no. 7, 072008 (2015)

  FERMILAB-PUB-15-080-E

- **“Precision measurement of the top-quark mass in lepton+jets final states”**

  V. M. Abazov *et al.* [D0 Collaboration].

  arXiv:1501.07912 [hep-ex]

DOI:10.1103/PhysRevD.91.112003

Phys. Rev. D **91**, no. 11, 112003 (2015)

FERMILAB-PUB-15-021-E

- **"Measurement of the $W+b$-jet and $W+c$-jet differential production cross sections in $p\bar{p}$ collisions at $\sqrt{s} = 1.96$ TeV"**

  V. M. Abazov *et al.* [D0 Collaboration].

  arXiv:1412.5315 [hep-ex]

  DOI:10.1016/j.physletb.2015.02.012

  Phys. Lett. B **743**, 6 (2015)

  FERMILAB-PUB-14-525-E

- **"Measurement of the electron charge asymmetry in $p\bar{p} \rightarrow W+X \rightarrow e\nu + X$ decays in $p\bar{p}$ collisions at $\sqrt{s} = 1.96$ TeV"**

  V. M. Abazov *et al.* [D0 Collaboration].

  arXiv:1412.2862 [hep-ex]

  DOI:10.1103/PhysRevD.91.032007, 10.1103/PhysRevD.91.079901

  Phys. Rev. D **91**, no. 3, 032007 (2015), Erratum: [Phys. Rev. D **91**, no. 7, 079901 (2015)]

  FERMILAB-PUB-14-514-E

- **"Measurement of the Forward-Backward Asymmetry in the Production of $B^{\pm}$ Mesons in $p\bar{p}$ Collisions at $\sqrt{s} = 1.96$ TeV"**

  V. M. Abazov *et al.* [D0 Collaboration].

  arXiv:1411.3021 [hep-ex]

  DOI:10.1103/PhysRevLett.114.051803

  Phys. Rev. Lett. **114**, 051803 (2015)

  FERMILAB-PUB-14-472-E

- **“Measurement of the ϕ^*_η distribution of muon pairs with masses between 30 and 500 GeV in 10.4 fb^{-1} of $p\bar{p}$ collisions”**
  V. M. Abazov *et al.* [D0 Collaboration].
  arXiv:1410.8052 [hep-ex]
  DOI:10.1103/PhysRevD.91.072002
  Phys. Rev. D **91**, no. 7, 072002 (2015)
  FERMILAB-PUB-14-430-E
- **“Measurement of the B^0_s lifetime in the flavor-specific decay channel $B^0_s \to D^-_s \mu^+ \nu X$”**
  V. M. Abazov *et al.* [D0 Collaboration].
  arXiv:1410.1568 [hep-ex]
  DOI:10.1103/PhysRevLett.114.062001
  Phys. Rev. Lett. **114**, no. 6, 062001 (2015)
  FERMILAB-PUB-14-388-E
- **“Measurement of the direct CP-violating parameter A_{CP} in the decay $D^+ \to K^- \pi^+ \pi^+$”**
  V. M. Abazov *et al.* [D0 Collaboration].
  arXiv:1408.6848 [hep-ex]
  DOI:10.1103/PhysRevD.90.111102
  Phys. Rev. D **90**, no. 11, 111102 (2014)
  FERMILAB-PUB-14-309-E
- **“Measurement of the effective weak mixing angle in $p\bar{p} \to Z/\gamma^* \to e^+e^-$ events”**
  V. M. Abazov *et al.* [D0 Collaboration].
  arXiv:1408.5016 [hep-ex]
  DOI:10.1103/PhysRevLett.115.041801
  Phys. Rev. Lett. **115**, no. 4, 041801 (2015)

FERMILAB-PUB-14-288-E